Modelling dissolved gas concentration in alkaline water electrolysis

Master Thesis
M.S. Roodenburg

TUDelft

Modelling dissolved gas concentration in alkaline water electrolysis

by

M.S. Roodenburg

Student Name	Student Number
Mounir Stefan Roodenburg	4431723

1$^{\text{st}}$ Examiner:	Dr. ir. J.W. Haverkort
2$^{\text{nd}}$ Examiner:	Dr. ir. D.A. Vermaas
3$^{\text{rd}}$ Examiner:	Prof. Dr. S. Kenjereš
Daily Supervisors:	Dr. ir. J.W. Haverkort & M.Sc A. Rajora
Institution:	Delft University of Technology
Place:	Process & Energy, 3mE, Delft
Project Duration:	September 1, 2021 - May 31, 2022

TUDelft

Abstract

Reducing the concentration of hydrogen and oxygen dissolved in the electrolyte helps to increase the efficiency of alkaline water electrolysis. This thesis provides an account of the evolution of dissolved concentration in the vicinity of the electrode surface for alkaline water electrolysis for the bubble size, the electrode height, the dissolved gas uptake by bubbles, and the bubble generation at the electrode surface. Included are an analytical and numerical model that not often include local electrokinetic effects coupled with a gas-liquid flow model. As is commonly found for experimental data on dissolved hydrogen and oxygen, the dissolved species is either an average concentration measured relatively far from the electrode surface or an average concentration at the electrode surface without any local effect of the electrode kinetics.

In this thesis an agreement is found for the analytical derived natural convection up to an height of 0.01 [m] with the numerical model. The fraction of dissolved hydrogen and oxygen taken up by the gas bubbles is enhanced for smaller bubbles, a high frequency of bubbles generated, and an increased mass transfer of dissolved gas at the electrode. Moreover, a clear difference is found for the dissolved hydrogen and oxygen evolution near the electrode for horizontal and vertical electrodes. Horizontal electrodes have more dissolved gas at the electrodes, likely due to the dissolved gas not being able to transfer to the gas bubbles as easily for vertical electrodes. Also, for both vertical and horizontal electrodes the dissolved gas concentration flattens for increased current density, likely due to homogeneous nucleation. For an increasing electrode height a lowering of the dissolved gas was observed, associated with an increased dissolved gas uptake by the bubbles. Most of these local effects are able to be modelled using an analytical and numerically combined model. These simulations greatly improve the understanding of dissolved hydrogen and oxygen evolution in the vicinity of electrodes.

Contents

Nomenclature

Abbreviations

Abbreviation	Definition
AWE	Alkaline Water Electrolysis(er)
HER	Hydrogen Evolution Reaction
OER	Oxygen Evolution Reaction
RDS	Rate Determining Step

Symbols

Symbol	Definition	Unit
$\overline{A}_{\mathrm{H_2}}$	real mass transfer effect hydrogen	[-]
$\overline{A}_{\mathrm{O_2}}$	real mass transfer effect oxygen	[-]
c_0	dissolved gas concentration at the electrode surface	[mol/m^3]
c_0'	dissolved gas flux at the electrode wall	[mol/m^2]
c_{s}	maximum solubility concentration	[mol/m^3]
c_{track}	concentration tracker species	[mol/m^3]
$c_{\mathrm{H_2}}$	dissolved gas concentration hydrogen	[mol/m^3]
$c_{\mathrm{O_2}}$	dissolved gas concentration oxygen	[mol/m^3]
$c_{\mathrm{H_2\,reff}}$	reference concentration hydrogen	[mol/m^3]
$c_{\mathrm{O_2\,reff}}$	reference concentration oxygen	[mol/m^3]
d_{p}	bubble diameter	[m]
D	diffusion coefficient	[m^2/s]
D^{eff}	effective diffusion coefficient	[m^2/s]
$\mathbf{D}$	dimensionless hydrodynamic self diffusion matrix	[-]
$\mathrm{Da_H}$	Darcy's number	[-]
E_{an}	anodic cell potential	[V]
E_{cath}	cathodic cell potential	[V]
E_{cell}	cell potential	[V]
E_{eq}	equilibrium cell potential	[V]
E_{eq}^0	standard equilibrium cell potential	[V]
f	hindrance function	[-]
f_{g}	gas evolution efficiency	[-]
F	Faraday constant	[C/mol]
$\mathbf{F}_{\mathrm{H_2}}$	Body force adherence region hydrogen	[N/m^3]
$\mathbf{F}_{\mathrm{O_2}}$	Body force adherence region oxygen	[N/m^3]
g	gravity constant	[m/s^2]
H	electrode height	[m]
i	subscript i refers to hydrogen or oxygen	[-]
i_{loc}	local current density	[A/m^2]
i_0	exchange current density	[A/m^2]
$i_{0,\mathrm{ref}}$	reference exchange current density	[A/m^2]
j	applied current density	[A/m^2]
k_{b}	bubble mass transfer coefficient	[m/s]
$\langle k_{\mathrm{d}} \rangle$	time-averaged mass transfer coefficient	[m/s]

Symbol	Definition	Unit
k_n	natural convective mass transfer coefficient	[m/s]
k_L	overall mass transfer coefficient	[m/s]
k_μ	bubble-induced micromixing	[m/s]
k_∞	infinity mass transfer coefficient	[m/s]
$\mathbf{K}_c$	stress tensor continuous phase	[Pa·s]
$\mathbf{K}_d$	stress tensor dispersed phase	[Pa·s]
l	inter-electrode width	[m]
L	mass transfer boundary layer	[m]
MW_i	molecular weight of hydrogen or oxygen	[kg/mol]
$\mathbf{M}$	momentum exchange	[kg/m s]
n_i	nucleation site density of hydrogen or oxygen	[#/m^2]
N_i	gas flux of hydrogen or oxygen	[mol/m^2 s]
Nu_H	dimensionless Nusselt number	[-]
p	pressure	[Pa]
Pr	dimensionless Prandtl number	[-]
q_v	volumetric gas flux	[m/s]
q_w	heat flux	[W/m^2]
r_b	bubble radius	[m]
R	Gas constant	[J/mol K]
R_{anode}	anode electrode resistance	[Ω]
$R_{cathode}$	cathode electrode resistance	[Ω]
R_{dia}	diaphragm resistance	[Ω]
R_{KOH}	electrolyte resistance	[Ω]
Ra_m	dimensionless modified Rayleigh number	[-]
S	sink for dissolved gas	[mol/m^3]
Sc	dimensionless Schmidt number	[-]
Sh_a	adherence region Sherwood number	[-]
Sh_b	bubble Sherwood number	[-]
Sh_H	natural convective Sherwood number	[-]
t	time	[s]
T	temperature	[K]
$\mathbf{u}$	interstitial mixture velocity	[m/s]
$\mathbf{U}$	superficial mixture velocity	[m/s]
$\mathbf{U}_c$	superficial continuous velocity	[m/s]
$\mathbf{U}_d$	superficial dispersed velocity	[m/s]
$\mathbf{U}_{Hdiff}$	superficial hydrodynamic slip velocity	[m/s]
$\mathbf{U}_{Sdiff}$	superficial shear-induced slip velocity	[m/s]
$\mathbf{U}_{Smig}$	superficial migration slip velocity	[m/s]
$\mathbf{U}_{Saff}$	superficial Saffman slip velocity	[m/s]
$\mathbf{U}_{stokes,1}$	superficial Stokes slip velocity, one bubble	[m/s]
$\mathbf{U}_{stokes}$	superficial Stokes slip velocity, plume	[m/s]
V_{ad}	volume adherence region	[m^3]
V_{bubble}	volume gas bubble	[m^3]
V_m	molar volume	[m^3]
$\mathbf{V}$	mass averaged mixture velocity	[m/s]
$\mathbf{V}_c$	mass averaged continuous velocity	[m/s]
$\mathbf{V}_d$	mass averaged dispersed velocity	[m/s]
z_i	electron transfer for hydrogen or oxygen	[-]
α_a	anodic charge transfer coefficient	[-]
α_c	cathodic charge transfer coefficient	[-]
β	thermal expansion coefficient	[-]
β_j	stress jump coefficient	[-]
β_d	Shear-induced coefficient	[-]
$|\dot{\gamma}|$	flow shear rate	[1/s]

Symbol	Definition	Unit
δ_c	concentration penetration depth	[m]
ϵ	porosity	[m]
ε_c	continuous phase fraction	[-]
ε_d	dispersed phase fraction	[-]
ε_H	enhancement factor	[-]
ε_{max}	maximum packing concentration	[-]
η_{act}	activation overpotential	[V]
η_{conc}	concentration overpotential	[V]
η_{ohm}	ohmic overpotential	[V]
θ	surface coverage	[-]
κ	permeability	[m^2]
κ_s	migration coefficient	[-]
λ	thermal conductivity	[W/m K]
μ_c	dynamic viscosity continuous phase	[Pa·s]
μ_d	dynamic viscosity dispersed phase	[Pa·s]
ν_c	kinematic viscosity continuous phase	[m^2/s]
ν_d	kinematic viscosity dispersed phase	[m^2/s]
ρ	mixture density	[kg/m^3]
ρ_c	density continuous phase	[kg/m^3]
ρ_d	density dispersed phase	[kg/m^3]
σ_{KOH}	electrolyte conductivity	[S/m]
σ_{KOH}^0	standard electrolyte conductivity	[S/m]
τ	shear stress	[Pa]

1

Introduction

1.1. Motivation

Transition from fossil fuels to renewable energies

The current utilization of fossil fuels and expected 50% increasing fossil fuel demand by 2050 poses serious threats to the environment such as natural resource depletion, harmful gas emissions, and climate change [1, 2]. The effects on global temperature rise must be minimized to reduce climate change and potential natural disasters. However, the global temperature has been increasing in the past 80 years illustrated in figure 1.1 stating the urgency to transition from fossil fuels to renewable energies. By reducing greenhouse gasses such as, hydrocarbons, nitrogen oxides, and carbon dioxide by 80 to 95% the temperature rise and harmful gas emissions should be lowered sufficiently before 2050 [3]. For European countries the current policy states that the greenhouse gasses must be reduced by at least 40%, while the share and energy efficiency for renewable energies must be increased by at least 32% and 32.5%, respectively [4]. New clean renewable energies must meet the increasing energy demand while minimizing the environmental threats. However, a global transition from fossil fuels to clean renewable energies generated by hydro, wind, and solar power gives rise to new challenges such as energy storage, energy infrastructure, system operation, energy peak demands and energy supply reliability [1, 5, 6]. Hydrogen production is an important solution to these challenges and especially water electrolysis is the most important process of hydrogen production.
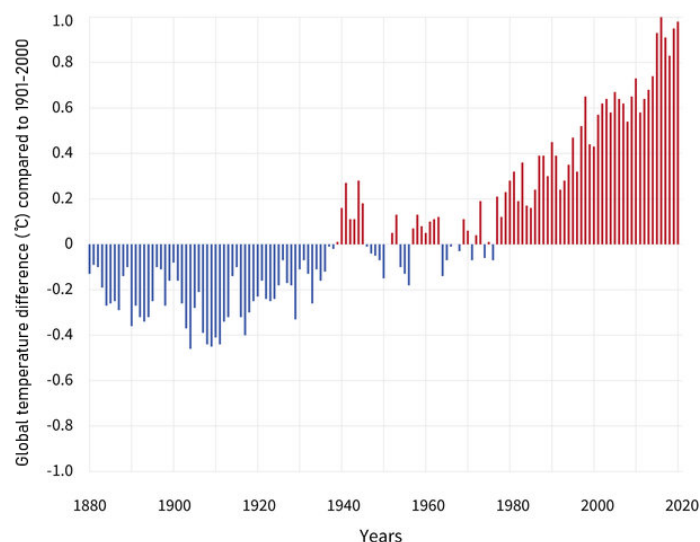
Figure 1.1: Surface temperature change for every year compared to the long-term average temperature from 1901-2000. The zero line indicates the long-term average temperature for the whole planet; the blue bars represent colder years and the red bars are warmer years compared to the long-term year average temperature [7].

Current Hydrogen landscape

Hydrogen is an essential base chemical and promising energy carrier. It is used in key industries like the production of ammonia, the most used fertilizer in the world, or the production of steel, among other [8, 9]. Since its initial use in the Apollo program for the transportation, hydrogen has gained significant specific weight in the transportation energy as an alternative to fossil fuels [10]. Beyond buses and forklifts, hydrogen is seen as a promising fuel for cars, trucks, ships, and even planes [11]. However, hydrogen gas can be produced in different manners such as steam reforming (grey hydrogen), by non-renewable energies (blue hydrogen), and electrolysis (green hydrogen). Green hydrogen is produced from renewable energies such as hydro, wind and solar power. Water electrolysis produced from renewable energies is currently the most sustainable method of producing hydrogen, but to minor means of hydrogen production. Presently, 90% of the hydrogen production is by steam reforming [12]. Water electrolysis still proves to be expensive due to its inefficient process and limitations to small-scale operations [13]. At the same time, large scale alkaline water electrolysis is cheaper and overall more efficient compared to acidic water electrolysis [14, 15].

Alkaline Water Electrolysis

Alkaline water electrolysis (AWE) is the process which uses renewable electricity to electrochemically decompose water in oxygen and hydrogen. During the AWE process several losses lower the overall efficiency. The losses must be minimized to improve overall efficiency of AWE. However, minimization of the losses is a rather complex matter and concerns three technical challenges:

- The optimization of mass transport for the dissolved hydrogen and oxygen species in the electrolyte which minimizes the concentration overpotential.
- The minimization of the ohmic resistances in the electrolyte such as bubble formation which lower the ohmic overpotential
- The minimization of the activation energy required to activate the electrochemical process at the electrode surface which lower the activation overpotential.

The three different challenges are illustrated in figure 1.2; the chemical species react at the electrode wall and move toward the bulk and the gas bubble. Meanwhile, the local current experiences resistance because of the bubbles. Improving on these challenges reduces the electricity losses. Therefore, the required cell voltage to have an operational electrolyzer is lower making the process more efficient. However, the complexity resides in the coupled hydrodynamic and electrochemical phenomena with the bubble dynamics coupling the two previous phenomena. The coupled phenomena makes it challenging to distinguish the different contributions to the required cell voltage. Understanding the highly coupled phenomena of AWE enables the possibility to increase its efficiency.
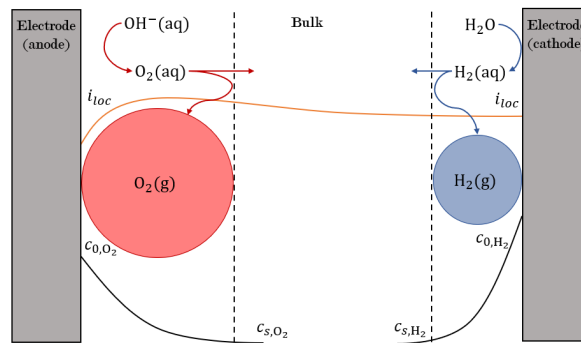
Figure 1.2: Schematic overview of the relevant processes in AWE; water is electrochemically decomposed to dissolved hydrogen (H_2 (aq)) and oxygen (O_2 (aq)) at the cathode and anode electrode wall, respectively. The dissolved gasses are transported to the bulk and their respective gas bubble. The local current density (i_{loc}) is affected by the bubbles that act as insulators.

The dissolved hydrogen and oxygen concentration reaches quantities which are significantly higher than their respective maximum solubility concentration; c_{s,H_2} and c_{s,O_2}, at high current densities. The high dissolved concentration, of both hydrogen and oxygen affect the electrode kinetics significantly.

The electrode kinetics become sluggish because the increased dissolved concentration minimizes the mass transport and increases the activation energy. The bubbles act as small insulators forcing the current to take a longer path to travel from the cathode to the anode. This extended path increases ohmic resistance and subsequently the energy loses. At the other hand, gas bubbles also act as a sink for the dissolved hydrogen and oxygen increasing the mass transport and lowering the activation energy. Moreover, the bubbles induce free natural convection and local bubble mixing which increases the mass transfer rate of the dissolved concentrations into the bubble. This increase in the mass transfer rate lowers the dissolved concentration and therefore lowering the activation energy.

Among the three coupled phenomena, the optimization of mass transfer and the minimization of the activation energy have the most significant effect on AWE efficiency. This is a result of the dissolved hydrogen and oxygen concentration. This effect is enhanced for large-scale AWE as they are operated at high current densities. Therefore, it is key to minimize the dissolved concentrations and the bubble fraction.

1.2. Problem Statement/ Previous Research and Gaps

Experimental work on dissolved concentration
Multiple studies [16, 17, 18, 19, 20, 21, 22, 23, 24, 25, 26] have performed measurements on the dissolved concentration of hydrogen and oxygen in both alkaline and acidic conditions for different vertical and horizontal electrode geometries [27, 28]. Two methods are used for measuring the supersaturation which are the current-interrupt and photographic/film method. Both methods are not capable of capturing the local dissolved concentration in the vicinity of the electrode. The first method [16, 17, 19, 21, 22, 24, 25, 26] is the better method and measures the dissolved concentration overpotential once the current is shut off. The second method [18, 20, 27, 23, 28] tracks the growth of a bubble of which only the foot of the bubble experiences the dissolved concentration near the electrode. In other words, the measured dissolved concentration is the average dissolved gas concentration at the electrode or the near-bulk concentration, respectively. The dissolved concentration near the electrode wall could be significantly higher than is measured and therefore the actual effect of dissolved concentration on the cell potential could be underestimated.

Bubble dynamics at electrodes
AWE efficiency is reduced by the production of bubbles on and near the electrode. Qian *et al.* [29] revealed that bubbles adhering to the electrode reduces the effective reaction area and increases the cell voltage. Kuznetsov [30] reveals that the fluid interaction between the electrode adhered bubbles and the electrolyte undergoes a sudden increase in shear while the adhered bubbles can be approached as a porous region. Janssen [31] showed that bubbles inhibit the transport of free ions in the electrolyte resulting in an increased electrolyte resistance. Vogt [32] indicated that gas bubbles can induce local mixing affecting velocity field and the local mass transport. Abdelouahed *et al.* [33] analyzed the effect of bubbles on the on the flow field and showed that it enhances mass transport of ions in the vicinity of the electrode. The previous studies confirm that bubbles have a significant effect on the flow field characteristics and the mass transport of the chemical species near the electrode. It is therefore key to develop a good understanding of the two-phase flow to increase AWE efficiency.

Numerical modelling of water electrolysis
Several studies have performed numerical simulations on flow dynamics coupled to electrochemical phenomena [34, 35]. They showed the effect of buoyancy-driven (natural/free) convection for an incompressible flow on the cell performance while using a combination of the mass, momentum, and Nernst-Plank equation. Other numerical studies model two-phase flow while only using Faraday's law to relate current with gas flux [36, 37]. These studies reveal that natural convection significantly affects the mass transport on a macroscopic scale. No effects of microscopic bubble induced mixing on mass transport are considered.

The majority of numerical modelling uses single-phase flow coupled to electrochemical phenomena, while few numerical simulations have been performed for two-phase flow models including electrochemical phenomena and bubble-induced mixing effects. To this day, there has been no numerical modelling that simulates an alkaline water electrolyzer which properly couples the two-phase flow characteristics with

the electrochemistry.

Analytical modelling of water electrolysis

Various works derive mathematical models that describe the performance of an electrochemical cell. Janssen *et al.* [38] describes and validates a theoretical model that captures the effect of bubble-induced mixing on the mass transfer rate. Vogt [39] introduces the gas-evolution efficiency stating the fraction of produced dissolved concentration that transfers into the bubbles adhered to the electrode. The gas-evolution efficiency, and the bubble coverage introduce new insights to the parameters that control the natural convection and bubble-induced convection. In the previous works empirical relations are used for the natural free convection while it is dependent on the flow characteristics of the electrochemical cell. Also, the bubble-induced convection is dependent on the free natural convection. However, the local velocity effects are not captured in the empirical relations. They require numerical modelling to better estimate the natural free convection and bubble induced mixing. Moreover, no theoretical model is made that describes the dissolved concentration near the electrode wall.

The two-phase hydrodynamics and electrochemical phenomena are highly coupled and introduce local effects on the velocity profile, gas fractions, current distribution, and chemical species. All local effects influence the dissolved concentration near the electrode wall. Numerical simulations help to analyse these highly coupled effects and give insight to the different local effects which are not captured with experimental work.

1.3. Research Questions

The aim of this work is to develop a complete numerical model that includes two-phase flow hydrodynamics, and the electrochemical phenomena to analyze the evolution of dissolved concentrations near the electrode wall. The focus will be on the natural convection, bubble induced mixing, and forced flow mass transfer coefficients which are not captured in the experimental work due to the local effects. The numerical model will be able to show how alkaline water electrolysis can be optimized. Based on the aim of this work the following research questions are posed:

- What is the effect of bubble radius and current density on the dissolved gas concentration?
- How does the mass transfer boundary layer thickness change with respect to electrode height, bubble radius, and nucleation site density?
- How do the local current density, electrode height, bubble radius, nucleation site density, and mass transfer rate affect the dissolved concentration of H_2 and O_2 near the electrode wall?
- Which factors such as local current density, bubble radius, nucleation site density, and mass transfer rate have to be minimized or maximized to lower the dissolved concentration?
- What dissolved concentration profiles can be predicted on the surface for vertical electrodes?

1.4. Document structure

The thesis has six chapters. Each chapter except for chapter 1 will have a short description about the content of the respective chapter. Chapter 1 consists of the introduction explaining the motivation of this research, a general explanation of alkaline water electrolysis, the problem research gaps, and the research questions. After the introduction, chapter 2 explains the necessary fundamentals in water electrolysis, and also the theory behind analytical and numerical modelling of AWE. The analytical modelling elaborates on the different coupled phenomena in AWE and the factors that affect the dissolved concentration. The section numerical modelling describes the physics used in the numerical simulations. Subsequently, in chapter 3 the geometries, and assumptions made to model the dissolved concentration are elaborated. In chapter 4 the results of the analytical model and the numerical model are showed. Then a comparison is made with the analytical, numerical, and experimental work. Lastly, chapter 5 concludes on the research questions and in chapter 6 recommendations are made for different approaches or improvements.

2

Theory

In this chapter the fundamentals of water electrolysis are elaborated using an alkaline water electrolyzer. Subsequently, a distinction is made between acidic and alkaline water electrolysis. Furthermore, the analytical model for deriving the dissolved gas concentration is explained as well for the numerical model.

2.1. Fundamentals of Water Electrolysis

Water electrolysis is the chemical decomposition of water into oxygen and hydrogen gas using an electrical current. A standard water electrolysis cell consists of two electrodes; an anode and a cathode, an electrolyte, a diaphragm or membrane, and an external power supply as shown in figure 2.1.
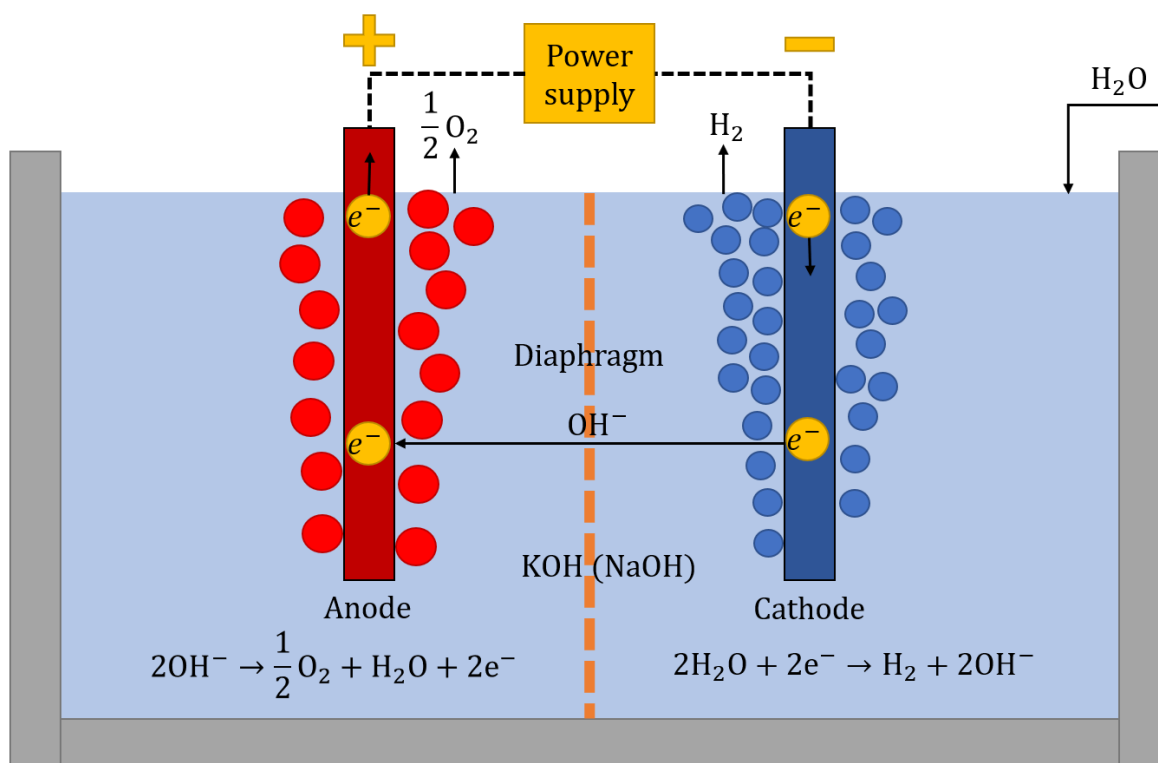
Figure 2.1: General schematic overview and operation of an alkaline water electrolysis cell.

The electrodes in AWE are usually nickel, nickel alloy or cobalt [15]. These materials are the most suitable due to its low costs, high catalytic activity, and satisfactory electric conductivity [40, 41]. The electrodes are immersed in the electrolyte. The electrolyte, which is a salt dissolved in a liquid, is

necessary for free ions to move. For AWE the electrolyte is water with dissolved potassium hydroxide or sodium hydroxide. To separate the gasses safely a diaphragm exists between the two electrodes. The diaphragm prevents gas crossover while allowing the transport of water, free ions, and dissolved species. Normally, the diaphragm has an average pore sizes of 1.0 μ [42]. The external power supply connects the two electrodes making a closed circuit and providing a voltage and current.

For electrolysis to occur an overvoltage (overpotential) is necessary between the anode and cathode which is supplied by the external power supply. During operation current flows from the power supply into the cathode electrode. The water in the vicinity of the cathode electrode is decomposed in dissolved hydrogen and hydroxide ions as shown in figure 2.1 and equation 2.1. Subsequently, hydroxide ions flow through the electrolyte passing the diaphragm to the anode electrode. Hydroxide ions flow because of the voltage and concentration gradients existing in the electrolyte. At the anode the hydroxide ions are recombined into dissolved oxygen and liquid water, as stated in equation 2.2. Lastly, the electrons flow towards the power supply resulting in a closed loop. During the process water must be replenished to continue the electrochemical process, and dissolved gas is removed by the nucleation of gas bubbles.

$$\text{Cathode half reaction}: 2H_2O \text{ (l)} + 2e^- \rightleftharpoons H_2 \text{ (g)} + 2OH^- \text{(aq)} \tag{2.1}$$

$$\text{Anode half reaction}: 2OH^- \text{(aq)} \rightleftharpoons \frac{1}{2}O_2 \text{ (g)} + H_2O \text{ (l)} + 2e^- \tag{2.2}$$
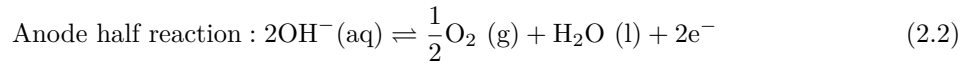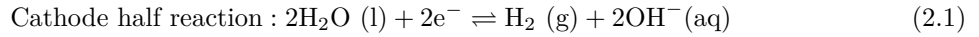
Adding the cathode half reaction and the anode half reaction result in the overall reaction as shown in equation 2.3.

$$\text{Overall reaction}: 2H_2O \text{ (l)} \rightleftharpoons 2H_2 \text{ (g)} + O_2 \text{ (g)} \tag{2.3}$$
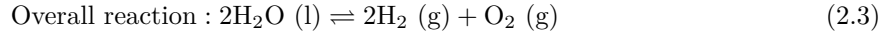
2.1.1. Electrochemistry

Electrolysis occurs for a certain overpotential which is determined by a set of overpotentials; equilibrium potential, ohmic overpotential, concentration overpotential, and activation overpotential. Each overpotential states the extra added voltage to the equilibrium potential required to perform electrolysis.

The various overpotentials increase with respect to current density and result in a distinct curve called the polarization curve illustrated in figure 2.2. The polarization curve is determined by the following equation:

$$E_{\text{cell}} = E_{\text{eq}}^0 + \eta_{\text{Ohm}} + \eta_{\text{conc}} + \eta_{\text{act}} \tag{2.4}$$

where E_{cell} is the cell voltage required to activate electrolysis, E_{eq}^0 is the equilibrium voltage at 25°C, η_{Ohm} is the ohmic overpotential, η_{conc} is the concentration overpotential, and η_{act} is the activation overpotential.
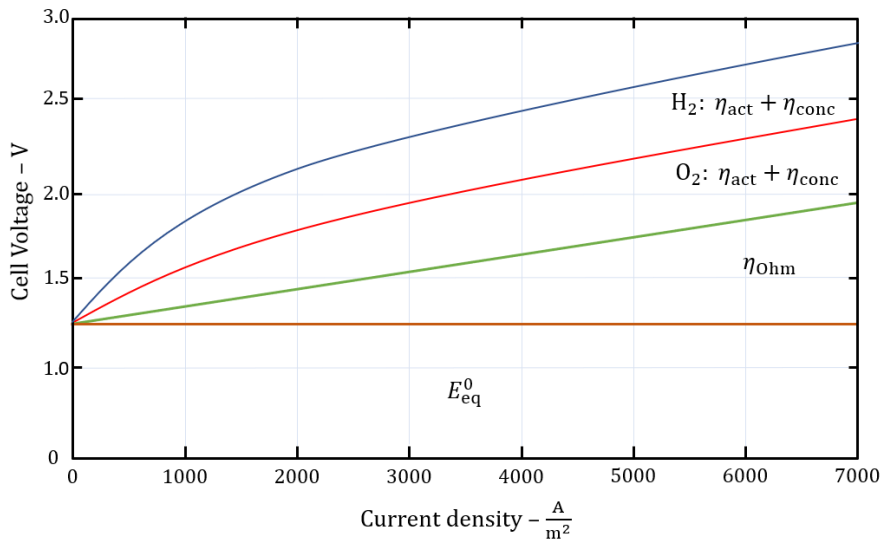
Figure 2.2: Example of an AWE polarization curve or cell performance curve. The cell voltage is determined by the equilibrium voltage, the activation overpotential, ohmic overpotential, and concentration overpotential.

Equilibrium Voltage & Concentration Overpotential

An electrochemical cell at zero current drawn (equilibrium) has no other overpotentials, and has a cell voltage of 1.23 V known as the equilibrium potential E^0_{eq} (thermodynamic equilibrium). The equilibrium potential is determined from the energy balance between the chemical potential of the reactants and the electrical energy. The equilibrium voltage is based on the assumption that the half reactions are reversible and is calculated by the Nernst equation:

$$E_{\text{eq}} = E^{\circ}_{\text{eq}} + \frac{RT}{F}\left[\frac{c_{\text{H}_2}^{1/2} \cdot c_{\text{O}_2}^{1/4}}{c_{\text{H}_2\text{O}}}\right] \tag{2.5}$$

where E°_{eq} is the standard potential at $T = 298$ K and $p = 1$ atm; R, T, and F are the universal gas constant, operating temperature, and Faraday constant, respectively; c_{H_2}, c_{O_2}, and $c_{\text{H}_2\text{O}}$ are the dissolved hydrogen concentration, dissolved oxygen concentration, and water concentration, respectively. Generally, the standard potential is dependent on temperature, but temperature is not evaluated in this thesis work so it remains constant at 1.23 V.

The second term of the Nernst equation is the concentration overpotential. The concentration overpotentials represents the effect of dissolved concentration of oxygen and hydrogen on the standard equilibrium potential. Both oxygen and hydrogen have their respective concentration overpotential determined on their respective dissolved gas concentration as shown in figure 2.2.

Ohmic overpotential

The traversing of electrons through the electrodes, and ions through the electrolyte passing the bubbles and the membrane towards the the cathode, are all resistances that add to the ohmic overpotential. Using Ohm's law the ohmic overpotential is determined by multiplying the current with the total resistance [43]:

$$\eta_{\text{Ohm}} = I \cdot (R_{\text{anode}} + R_{\text{KOH}} + R_{\text{dia}} + R_{\text{cathode}}) \tag{2.6}$$

Where R_{anode} and R_{cathode} are the resistances experienced by the electrons in the anode and cathode electrode, respectively; R_{KOH} is the resistance experienced by the ions flowing through the electrolyte, and R_{dia} is the resistance the ions experience passing the diaphragm. In this thesis work, no diaphragm nor the resistances experienced in the electrodes are considered.

The resistance R_{KOH} follows Pouillet's law:

$$R_{\text{KOH}} = \frac{b}{\sigma_{\text{KOH}}A} \tag{2.7}$$

where b is the width between the electrodes, A is the surface of the electrode, and σ_{KOH} is the conductivity of the electrolyte. Due to the presence of the bubbles the conductivity of the electrolyte is corrected by the Bruggeman correction [44]. The Bruggeman equations correlates the tortuosity factors of the porous media with their porosity:

$$\sigma_{\text{KOH}} = \sigma^0_{\text{KOH}}(1 - \epsilon)^{1.5} \tag{2.8}$$

where σ^0_{KOH} is the conductivity of the electrolyte without bubbles, and ϵ is the porosity. For the porosity we assume that it is equal to void fraction created by the bubbles ($\epsilon = \varepsilon_{\text{d}}$). The conductivity of the electrolyte without bubbles is dependent on the potassium hydroxide concentration and temperature. Higher concentrations of KOH increases the conductivity, because more free ions are present. This makes the ion transfer from the cathode to the anode easier. Higher temperatures also help the ions to more more freely. The electrolyte conductivity dependence on concentration en temperature is presented in figure A.1 in Appendix A.

Activation overpotential

The activation overpotential is the potential required for both the anode and cathode half reactions to overcome the energy threshold to push the reaction towards the product generation. The activation overpotential at the anode generally consumes more potential than the cathode [45]. The Butler-Volmer equation is generally used to determine the activation overpotential:

$$i_{\text{loc}} = i_0\left[\exp\left(\frac{\alpha_{\text{a}}Fz_i\eta_{\text{act,an}}}{RT}\right) - \exp\left(-\frac{\alpha_{\text{c}}Fz_i\eta_{\text{act,cath}}}{RT}\right)\right] \tag{2.9}$$

$$i_0 = i_{0,\text{ref}} \cdot \frac{c_{\text{H}_2}}{c_{\text{H}_2}^{\text{ref}}}^{(\alpha_c/2)} \cdot \frac{c_{\text{O}_2}}{c_{\text{O}_2}^{\text{ref}}}^{(\alpha_a/4)} \tag{2.10}$$

where:

- i_{loc} is the local electrode current density, $[\text{A/m}^2]$
- i_0 is the exchange current density, $[\text{A/m}^2]$
- $i_{0,\text{ref}}$ is the reference exchange current density for the hydrogen oxidation at the cathode and oxygen reduction at the anode, $[\text{A/m}^2]$
- α_a is the anodic charge transfer coefficient, $[-]$
- α_c is the cathodic charge transfer coefficient, $[-]$
- $\alpha_\text{a} = 1 - \alpha_\text{c}$, $[-]$
- $\eta_{\text{act,i}}$ is the activation overpotential for the respective electrode. $\eta_{\text{act,i}} = E_\text{i} - E_{\text{eq}}^0$, where E_i is the anodic or cathodic electrode potential and E_{eq}^0 is the standard equilibrium potential, $[\text{V}]$
- z_i is the number of electrons transferred for the anodic or cathodic reaction, $[-]$
- $c_{\text{H}_2}^{\text{ref}}$ is the maximum hydrogen solvability concentration, $[\text{mol/m}^3]$
- $c_{\text{O}_2}^{\text{ref}}$ is the maximum oxygen solvability concentration, $[\text{mol/m}^3]$

However, the Butler-Volmer equation (2.9) assumes that the concentration near the electrodes is equal to the concentration in the bulk. In other words, the mass transfer is dominant compared to the reaction rate. Multiple authors [19, 20, 21, 22] elaborate that the dissolved concentration near the electrode is significantly higher than the bulk concentration. The Butler-Volmer equation (2.9) can be extended with mass transport limitations by substituting the Nernst equation 2.5 in equation 2.9 which is then re-written to:

$$i_{\text{loc}} = i_0 \left[\frac{c_{\text{H}_2}(0,t)}{c_{\text{H}_2}^{\text{ref}}} \exp\left(\frac{\alpha_\text{a} F z_i \eta_{\text{act,an}}}{RT} \right) - \frac{c_{\text{O}_2}(0,t)}{c_{\text{O}_2}^{\text{ref}}} \exp\left(-\frac{\alpha_\text{c} F z_i \eta_{\text{act,cath}}}{RT} \right) \right] \tag{2.11}$$

where $\eta_{\text{act,cath}} = E_{\text{cath}} - E_{\text{eq}}^0$, and $\eta_{\text{act,an}} = E_{\text{an}} - E_{\text{eq}}^0$.

Next to the Butler-Volmer equation other equations exist that describe the electrode kinetics. Both hydrogen evolution reaction (HER) and oxygen evolution reaction (OER) consists of several intermediate reaction steps. Each intermediate reaction step can be described by the extended Butler-Volmer equation or other electrode kinetics. However, the intermediate step that limits the electrode kinetics is the most important and is called the rate determining step (RDS). In the following sections the HER and OER are explained and what electrode kinetics is the RDS.

Intermediate Steps Hydrogen Evolution Reaction

The hydrogen evolution reaction (HER) in water electrolysis consists of three (or four) intermediate reaction steps and are similar for alkaline and acidic conditions. The first intermediate step is the Volmer reaction step where a hydrogen atom is adsorbed on the electrocatalyst [15]:

$$\begin{aligned} \text{alkaline} &: \text{H}_2\text{O(l)} + \text{e}^- \rightleftharpoons \text{H}_{\text{ad}}(*) + \text{OH}^-(\text{aq}) \\ \text{acidic} &: \text{H}^+(\text{aq}) + \text{e}^- \rightleftharpoons \text{H}_{\text{ad}}(*) \end{aligned} \tag{2.12}$$
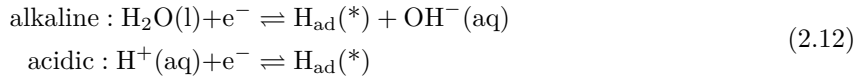
The hydrogen atoms adsorbed on the electrocatalyst could then undergo a surface diffusion reaction step [46]:

$$\text{H}_{\text{ads, A}}(*) \rightleftharpoons \text{H}_{\text{ads, B}}(*) \tag{2.13}$$

where A and B are distinct adsorption and desorption sites on the electrode surface [47]. The adsorbed hydrogen atom subsequently reacts to dissolved hydrogen molecules according to the Heyrovsky reaction step [15]:

$$\begin{aligned} \text{alkaline} &: \text{H}_2\text{O(l)} + \text{H}_{\text{ad}}(*) + \text{e}^- \rightleftharpoons \text{H}_2(\text{aq}) + \text{OH}^-(\text{aq}) \\ \text{acidic} &: \text{H}^+(\text{aq}) + \text{H}_{\text{ad}}(*) + \text{e}^- \rightleftharpoons \text{H}_2(\text{aq}) \end{aligned} \tag{2.14}$$
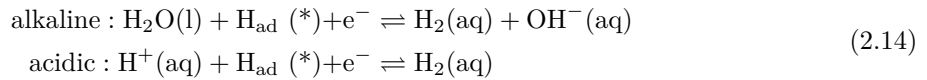
Alternatively, two adsorbed hydrogen atoms react to a dissolved hydrogen molecule following the Tafel reaction step:

$$\text{alkaline \& acidic} : \text{H}_{\text{ad}}(*) + \text{H}_{\text{ad}}(*) \rightleftharpoons \text{H}_2(\text{aq}) \tag{2.15}$$
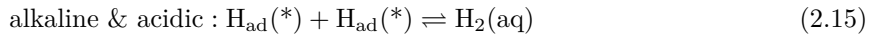
Nowadays, it is unclear what intermediate steps define the HER for acidic and alkaline conditions and their respective RDS. Kahyarian *et al.* [47] mentions that multiple studies state alternate elementary reaction steps and RDS for HER . For example, Brug *et al.* [48] uses a combination of the Volmer, Hevrovsky and Tafel steps as stated by the equations 2.12, 2.14, and 2.15, respectively. For lower current densities the Volmer intermediate reaction step is the RDS and for higher current densities the Hevrovsky intermediate reaction step is the RDS. Conway and Bai [46] proposed an additional intermediate reaction step shown in equation 2.13 for the adsorbed hydrogen atom to diffuse on the electrocatalyst surface . According to Kahyarian *et al.* [47] the RDS for lower current densities is the surface diffusing step and for high current densities the Hevrovsky reaction step.

The importance of knowing which intermediate step is the RDS defines the electrode kinetics that must be used. For example, if the reaction mechanism is not reaction-limited, but rather diffusion-limited, dissolved gas concentration does not affect the electrode kinetics.

Intermediate Steps Oxygen Evolution Reaction

The oxygen evolution reaction (OER) has four intermediate reactions steps due to the four electrons transferred in the OER half reaction. Giordano *et al.* [49] stated the various reaction pathways for OER illustrated in figure 2.3. The S indicates an activation site on the electrode surface. The three
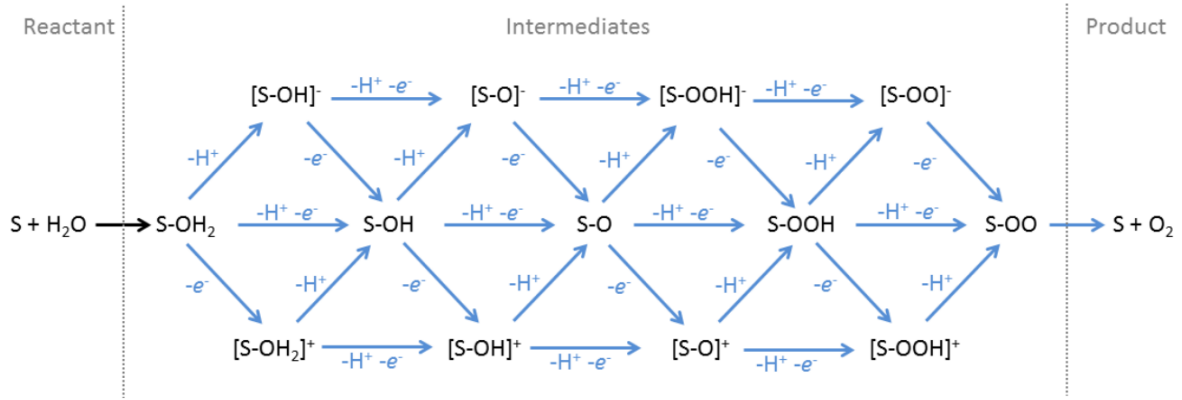
Figure 2.3: Various reaction pathways of the oxygen evolution reaction from Giordano *et al.* [49].

intermediate chemical species in OER are O, OH, and OOH and are identical for alkaline and acidic conditions [50, 51]. The OOH intermediate is assumed to be present and can be neglected if two adsorbed oxygen molecules recombine to a dissolved oxygen molecule. Varying the pH levels affect the reaction paths individually, but no clear pattern is found for the reaction path as a function of pH according to Giordano *et al.* [49]. Rather, Exner *et al.* [52] states that the second intermediate step is a Volmer step and the RDS at zero overpotential, while for both alkaline and acidic conditions the last intermediate step, the oxygen formation is the RDS at overpotentials higher than zero volt.

Alkaline and Acidic Water Electrolysis

The key difference between alkaline and acidic water electrolysis is the electrolyte. Whether the electrolyte is alkaline or acidic, it affects the activity, stability and material selection of the electrocatalysts, gas purities, bubble growth, and the reaction mechanisms [14].

Alkaline water electrolyzers have an ample variety in catalysts materials which are well qualified because they are non-noble metals, abundant, and cheap. Combining the non-noble metals give a high yield of suitable alloys that can be tuned to increase the activity of electrocatalysts. The abundancy of the non-noble metals and low costs helps to increase the quantity of electrocatalyst and therefore the reaction surface area increasing the overall reaction rate[53, 54].

Acidic water electrolyzers are limited to the noble, scarce, and expensive platinum transition metals. The platinum transition metals are the only active and fairly stable electrocatalysts for hydrogen gas production. The catalyst at the anode is only fairly stable because it dissolves over time which is problematic for long operation times [55, 56]. Due to high costs of platinum only a limited quantity is used reducing the active surface area and therefore lowering the overall reaction rate.

The gas purities for alkaline water electrolysis are less compared to acidic water electrolysis due to the

higher gas crossover rates through the cell diaphragm. This is a result of the bigger pore size of AWE diaphragms which are several orders of magnitude bigger than the diaphragms used in acidic water electrolyzers[15].

The bubble growth is also affected by the nature of the electrolyte. In general the size of both oxygen and hydrogen bubbles is bigger under acidic compared to alkaline conditions [57]. Increasing the respective concentration lowers the bubble size as seen in various experiments of Janssen *et al.* [28].

An alkaline electrolyzer has two half reactions already stated by the equations 2.1 and 2.2. For an acidic water electrolyzer the following half reactions hold with the same overall reaction stated in equation 2.3:

$$\text{Anode half reaction : } H_2O(l) \rightleftharpoons \frac{1}{2}O_2(g) + 2H^+(aq) + 2e^- \tag{2.16}$$

$$\text{Cathode half reaction : } 2H^+(aq) + 2e^- \rightleftharpoons H_2(g) \tag{2.17}$$
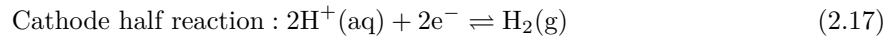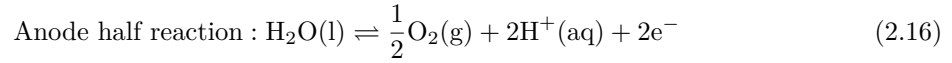
The half reactions for both alkaline and acidic conditions are different and consist of multiple intermediate reaction steps. The intermediate steps are also different for the alkaline and acidic half reactions.

2.1.2. Flow Characteristics & Chemical Species Evolution

The flow behaviour in an electrolysis cell is dependent on the bubble motion. The bubbles drag the fluid resulting in flow fields which does not apply for single-phase flow fields. Subsequently, the flow field affects the distribution of the chemical species within the electrolysis cell. Both the flow characteristics and chemical species are elaborated in the sections 2.3.2 and 2.3.4, respectively

2.2. Analytical Modelling

The analytical model is a mathematical model built in combination with J.W. Haverkort [58]. The model is based on the schematic overview illustrated in figure 2.4. The model is extended with (semi)-empirical relations from literature. The analytical model is able to determine the dissolved gas concentrations and the gas evolution efficiency.
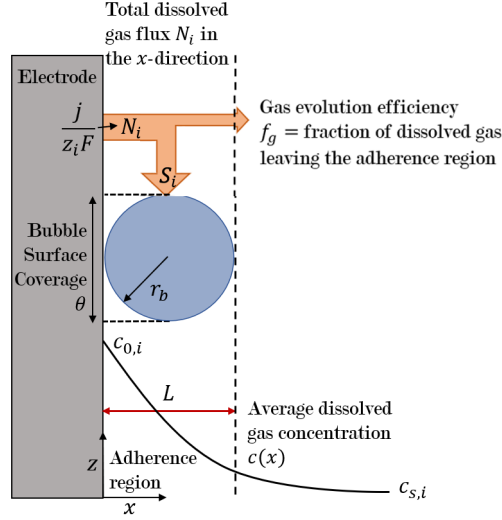
Figure 2.4: Schematic overview of the electrolysis operation near the electrode. The dissolved gas flux (N_i) is distributed in to the gas bubble (S_i) and to the bulk. The various parameters are used in the analytical modelling to model the dissolved concentration and the gas evolution efficiency.

The half reactions shown in equations 2.1 and 2.2 relate the ion flux $\frac{j}{z_i F}$ with the dissolved gas flux at the electrode wall N_i as stated in equation 2.18:

$$N_i = \frac{j}{z_i F} \tag{2.18}$$

,where i is the chemical species H_2 or O_2, z_i is the electrons transferred based on the respective half reaction, and F is the Faraday's constant. The electrons reacting in the half reaction are the effective current. Some of the current can be lost due to heat generation in the electrode or in undesired side reactions [59].

The flux of the dissolved gasses entering from the electrode wall is dependent on the mass transfer of the convective and diffusive flow within the adherence region. The expression for the dissolved flux can be written as:

$$N_i = -D_i^{\text{eff}} \frac{dc_i}{dx} = -D_i \text{Sh}_a \frac{dc_i}{dx} \tag{2.19}$$

where Sh_a is the adherence Sherwood number stating the ratio between the convective mass transfer to the diffusive mass transport in the adherence region.
The conservation differential equation for the dissolved concentration, c_i, within the adherence region is assumed to follow a purely 1-D diffusive flux:

$$D_i \text{Sh}_a \frac{\partial^2 c_i}{\partial x^2} = \pm S \tag{2.20}$$

where a positive S implies a sink for the dissolved gas. A fraction of the dissolved gas transfers to the gas bubbles which act as the sink. The other fraction enters the bulk electrolyte. The assumptions made for the adherence region are the following: 1-D steady state system, constant density (ρ), constant diffusion coefficient (D), and no advection in the x and z-direction (purely diffusive).

Assuming the sink term is a first order reaction rate, the sink yields:

$$S = N_\perp a = k_\mathrm{L} a \Delta c \tag{2.21}$$

where $N_\perp$ is the average mass flux of the dissolved gas in/out of the gas bubble, k_L is the mass transfer coefficient from dissolved gas into the bulk, a is the volumetric surface area, and Δc is the driving force. The driving force is the gas dissolved in the liquid into the gas bubble.

The rate at which the dissolved gas enters or leaves the gas bubble is the bubble mass transfer coefficient k_b and it is defined as:

$$k_\mathrm{b} = \mathrm{Sh_b} \frac{D_i}{2r_i} \tag{2.22}$$

where $\mathrm{Sh_b}$ is the bubble Sherwood number (assumed to be 2), and r_i is the bubble radius of hydrogen or oxygen.

The 2nd order ordinary differential equation (ODE) stated in equation 2.20 is now expressed as:

$$-D_i^\mathrm{eff} \frac{d^2 c_i}{dx^2} = k_\mathrm{L} a \Delta c \tag{2.23}$$

The first boundary condition at the electrode wall (x=0) is a flux boundary, which can be typically imposed in either experiments or regular operating conditions. The dissolved gas concentration at the electrode wall may be provided, although this is typically not a control parameter and so it is difficult to impose:

$$\frac{dc}{dx}\Big|_{x=0} = c_0' = \frac{j}{z_i F D_i^\mathrm{eff}} \tag{2.24}$$

The second boundary condition states that the concentration has reached the maximum solubility concentration at the position $x = L$.

$$c(x = L) = c_{\mathrm{s},i} \tag{2.25}$$

where $c_{\mathrm{s},i}$ is the maximum solubility of hydrogen or oxygen in water, and L is the mass transfer boundary layer:

$$L = \frac{D_i}{k_\mathrm{L}} \tag{2.26}$$

where k_L is the liquid mass transfer coefficient. The mass transfer boundary layer indicates the position where dissolved gas can either transfer to the bubbles for $x \leq L$ or leaves for the bulk for $x > L$. The liquid mass transfer coefficient expresses the rate of the dissolved species heading towards the bulk fluid. The liquid mass transfer coefficient is elaborated in section 2.2.1.

Solving the 2nd ODE stated in equation 2.23 with the two previous mentioned boundary conditions results in the following concentration profile for the dissolved gas:

$$c_i(x) = c_{\mathrm{s},i} + c_0' L \frac{\tanh(\mathrm{Ha})}{\mathrm{Ha}} = c_{\mathrm{s},i} + c_0' L \varepsilon_\mathrm{H} \tag{2.27}$$

where Ha is the Hatta number, and ε is the enhancement factor. The enhancement factor is named such, because the higher the enhancement factor the more of the dissolved gas enters the bubbles. The Hatta number is a dimensionless number and it relates the ratio of chemical species reacting in a thin film to the rate of diffusion through the film. The chemical species reacting in the thin film refers to the dissolved gas concentration entering the gas bubbles. The Hatta number is defined as:

$$\mathrm{Ha} = \frac{L}{\delta_c} = \sqrt{\frac{k_\mathrm{L} a L^2}{D_i^\mathrm{eff}}} \tag{2.28}$$

where δ_c is the concentration penetration depth of the dissolved gas in the mass transfer boundary layer:

$$\delta_c = \sqrt{\frac{D_i^\mathrm{eff}}{k_\mathrm{L} a}} = \sqrt{\frac{\mathrm{Sh_a}}{n_i \pi \mathrm{Sh_b}}} \tag{2.29}$$

Gas evolution efficiency
The gas evolution efficiency f_g represents the fraction of gas produced at the electrode wall that ends directly in the bubbles:

$$f_g = \frac{N(y = 0) - N(y = L)}{N(y = 0)} \tag{2.30}$$

The general flux expressed in equation 2.19, and the first derivative of the dissolved concentration with respect to x stated in equation 2.27 at position $x = 0$ and $x = L$, gives the expression for the gas evolution efficiency:

$$f_g = 1 - \frac{\cosh(\mathrm{Ha}(1 - \frac{2r}{L}))}{\cosh(\mathrm{Ha})} \tag{2.31}$$

The gas evolution efficiency in equation 2.31 holds for the limit where L is thicker than the bubble diameter ($L > 2r$). However, for the limit L is thinner than the bubble diameter ($L < 2r$) the gas evolution efficiency can be approximated as:

$$f_g = 1 - \frac{1}{\cosh(\mathrm{Ha})} \tag{2.32}$$

2.2.1. Overall mass transfer coefficient

The overall mass transfer coefficient expresses the total rate at which dissolved gas enters the bubbles within the mass transfer boundary layer. Janssen *et al.* [38] derived a relation for the overall mass transfer coefficient k_L shown in equation 2.33. It is a combination of the natural convective mass transfer coefficient k_n and the bubble induced mixing mass transfer coefficient k_μ:

$$k_L = k_n(1 - \theta) + \theta k_\mu \tag{2.33}$$

where θ is the bubble surface coverage as shown in figure 2.4. The natural convective mass transfer coefficient represents the rate of dissolved gas that enters the gas. The natural convective mass transfer is caused by the buoyancy of the bubbles and the drag imposed on the electrolyte. This local effect on the velocity near the electrode improves the mixing of the dissolved gas which increases the total mass transfer. The natural convective mass transfer coefficient is defined as :

$$k_n = \mathrm{Sh}\frac{D_i}{H} \tag{2.34}$$

where Sh is the local Sherwood number, and H is the electrode height. The local Sherwood number is a dimensionless number that represents the ratio of convective to diffusive mass transport of the dissolved gas towards the bubble. The natural convective mass transfer coefficient is dependent on the orientation of the electrode and relates to the local Sherwood number.

The bubble induced mixing is caused by the formation of the bubbles. The bubble nucleation induces local mixing which homogenises the concentration near the electrode wall. The mass transfer rate of dissolved gas to the bubbles is increased, because the concentration near the bubble is increased.

2.2.2. Natural convection and Vertical Electrodes

Brangeon *et al.* [60] performed numerical simulations on natural convection for asymmetrically heated inclined walls for various uniform heat fluxes. The work of Brangeon *et al.* has been validated in reasonable agreement with the data of Dupont *et al.* [61] and Web and Hill [62]. The relation found by Brangeon *et al.* is:

$$\mathrm{Nu_H} = 0.62 \cdot (\mathrm{Ra_m} \cos(i))^{0.204} \tag{2.35}$$

where $\mathrm{Nu_H}$ is the local Nusselt number along the height H, $\mathrm{Ra_m}$ is the modified Rayleigh number, and $\cos(i)$ is the inclination of the wall. Assuming an inclination of $90°(i = 0)$ and the analogy between heat and mass transfer, the above equation is rewritten to:

$$\mathrm{Sh_H} = 0.62 \cdot \mathrm{Ra}_m{}^{0.204} \tag{2.36}$$

where $\mathrm{Sh_H}$ is the local Sherwood number along the height of the electrode, and $\mathrm{Ra_m}$ represents the ratio between the buoyancy and the mass transfer by diffusion and/or convection.

The modified Rayleigh number according to Brangeon *et al.* [60] is:

$$\text{Ra}_\text{m} = \frac{g\beta q_w l^4}{\lambda \nu^2}\frac{l}{H}\text{Pr} \tag{2.37}$$

where q_w is the uniform heat flux normal at the wall, l is the characteristic width, λ is the thermal conductivity, H is the wall height, and Pr is the dimensionless Prandtl number. Again, assuming heat and mass transfer analogy, the Prandtl number is replaced for the dimensionless Schmidt number (Sc= $\frac{\nu_i}{D_i^\text{eff}}$). The Schmidt number relates the kinematic to the dynamic viscosity (internal friction of the fluid).

In case of mass transport, the driving force responsible in the modified Rayleigh number is not the expansion due to temperature differences ($\frac{\beta q_w}{\lambda} \sim \nabla T$), but rather driven by the gas density difference between the gas bubbles and the electrolyte ($\nabla \rho$):

$$\text{Ra}_\text{m} = \frac{g\nabla\rho l^4}{\nu^2}\frac{l}{H}\text{Sc} \tag{2.38}$$

The density is subsequently expressed in terms of the wall gas fraction:

$$\frac{\Delta\rho}{(\rho_\text{c} + \rho_\text{d})} = \varepsilon_\text{d} \tag{2.39}$$

where ε_d is the gas fraction. Expressing the modified Rayleigh number with the gas fraction as the driving force, rather than the density difference:

$$\text{Ra}_\text{m} = \frac{g\nabla\varepsilon_\text{d} l^4}{\nu^2}\frac{l}{H}\text{Sc} \tag{2.40}$$

The gas fraction gradient $\nabla\varepsilon_\text{d}$ is based on Fick's first law within the mass transfer boundary layer:

$$\mathbf{U}_\text{d} = -D_i^\text{H,eff}\nabla\varepsilon_\text{d} \tag{2.41}$$

where $\mathbf{U}_\text{d}$ is the superficial velocity of the dispersed phase, and D_i^eff is the effective diffusivity of bubbles towards other bubbles. The effective diffusivity between bubbles is caused by hydrodynamic self diffusion and shear-induced diffusion, both explained in section 2.3.2.

The gas fraction is generated by the gas flux entering normal to the electrode wall. The superficial velocity is directly coupled to the current density by Faraday's' law:

$$\mathbf{U}_\text{d} = \frac{jV_\text{m}}{z_i F} \tag{2.42}$$

where V_m is the molar volume. Substituting equation 2.41 and 2.42 respectively in equation 2.40 results in the local Sherwood number along the height of the electrode in terms of current density, electrode width, and electrode height:

$$\text{Sh}_\text{H} = 0.62 \cdot \left[\frac{gjV_\text{m}l^4}{D_\text{H,eff}^2 \nu_i z_i F}\frac{l}{H}\right]^{0.204} \tag{2.43}$$

The above relation for the local Sherwood number holds for the range $4\cdot10^3 < \text{Ra}_\text{m} \leq 1.29\cdot10^5$. If the modified Rayleigh number is higher than $1.29\cdot10^5$ the following relation holds for the local Sherwood number:

$$\text{Sh}_\text{H} = 0.72 \cdot \left[\frac{gjV_\text{m}l^4}{D_\text{H,eff}^2 \nu_i z_i F}\frac{l}{H}\right]^{0.187} \tag{2.44}$$

which holds up to $\text{Ra}_\text{m} \leq 5\cdot10^6$.

2.2.3. Bubble induced mixing

Bubble induced mixing is the enhancement of local mixing effect due to the nucleation of bubbles. This effect has been mathematically derived by Janssen *et al.* [38]. The derivation describes how the local mixing only accounts for bubbles detaching from the electrode surface and not the adhered bubbles. It is assumed that the radius remains constant of the bubble, the bubble distribution over the electrode surface remains uniform, and the time for a bubble to nucleate and detach of the electrode surface is equal for all bubbles.

At $t = 0$ after the bubble release, the electrode attains the bulk concentration c_s over an area of $\bar{A}\pi r_{\text{b}}^2$. The surface area covered is a function of the bubble nucleation density and the real projected area by all bubbles:

$$\theta_r = \bar{A}\theta = \bar{A}n\pi r_{\text{b}}^2 \tag{2.45}$$

where $\bar{A}$ is the ratio between the real effect the bubble coverage has on mixing and the projected surface coverage (θ).

Over time the original concentration profile will re-establish at the nucleation site, which we assume can be described by the 1D diffusion equation solution which gives a mass transfer coefficient $k_{\text{d}} = \sqrt{\frac{D}{\pi t}}$. Furthermore, at time $t = t_d$ a new bubble is released at the same location.

The time-average k_{d} between $t = 0$ and $t = t_d$ is:

$$\langle k_{\text{d}} \rangle = \frac{1}{t_d} \int_{t=0}^{t=t_d} \sqrt{\frac{D}{\pi t}} dt = 2\sqrt{\frac{D}{t_d \pi}} \tag{2.46}$$

where t_d is the bubble release period. Janssen *et al.* estimates $\langle k_{\text{d}} \rangle$ as the representative time at which all bubbles are replenished once. The time it requires is the total amount of volume of the bubbles replenished by the volumetric gas flux

$$t_d = \frac{V_{\text{bubble}} n}{q_v} \tag{2.47}$$

where V_{bubble} is the bubble volume, and q_v is the volumetric gas flux. The volumetric gas flux is estimated by the current density and the gas evolution efficiency

$$q_v = \frac{j}{z_i F} \frac{MW_i}{\rho_i} f_{\text{g}} \tag{2.48}$$

where MW_i is the molecular weight of the given chemical species.

If the bubble is within the time range $0 < t < t_d$ the bubble is adhered and not detached yet. In this time range the natural convective mass transfer coefficient holds. Only the moment when the bubbles are released the time-average mass transfer coefficient in equation 2.46 applies. Combining the effect of the free natural convection and time-averaged mass transfer coefficient results in the bubble induced mixing mass transfer coefficient:

$$k_{\mu} = \sqrt{k_{\text{n}}^2 + \langle k_{\text{d}} \rangle^2} \tag{2.49}$$

where k_{μ} is the bubble induced mixing mass transfer coefficient.

The overall mass transfer coefficient k_{L} is:

$$k_{\text{L}} = k_{\text{n}}(1 - \theta) + \theta k_{\mu} \tag{2.50}$$

Note that the bubble induced mixing increases with increased surface coverage.

Finally. expanding the equation for the overall mass transfer coefficient with the operating parameters

$$k_{\text{L}} = k_{\text{n}}(1 - \bar{A}n\pi r_{\text{b}}^2) + \bar{A}n\pi r_{\text{b}}^2 \sqrt{k_{\text{n}}^2 + \frac{3D}{nr_{\text{b}}^3} \frac{j}{z_i F} V_{\text{m}} f_{\text{g}}} \tag{2.51}$$

where V_{m} is the molar volume.

2.3. Numerical Modelling

In this section the theory of the numerical modelling is elaborated and how the physics are coupled in AWE. The numerical modelling is performed in the multi-physics platform COMSOL. First, the vertical and horizontal geometries are explained. Secondly, an overview is given of the different physics used and how they are coupled. Finally, the different physics are elucidated.

2.3.1. Numerical Coupling Electrolysis

The numerical modelling is performed in the commercial available multiphysics platform COMSOL. COMSOL is a software package using finite element method to understand, predict, and optimize for a broad range of physical phenomena [63]. Various pre-built modelling packages exist in COMSOL to address certain physics such as the flow characteristics, the chemical species transport, and the electrochemical behavior. Accordingly, these pre-built packages with physical extensions shall be used to evaluate the coupled physics in AWE.

The coupling and dependent variables in AWE are illustrated in figure 2.5.
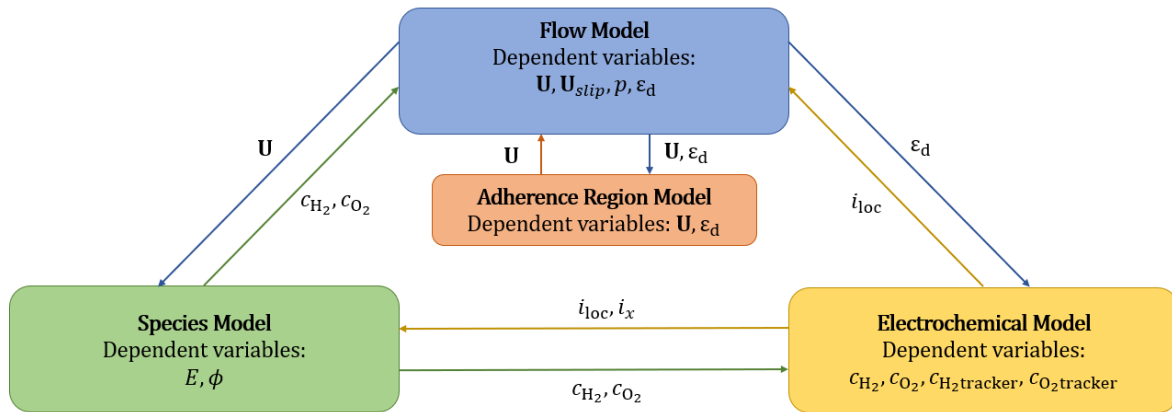
Figure 2.5: Schematic overview of the physics coupling and dependent variables of the different pre-built COMSOL models to simulate electrolysis.

Each model has different governing equations, dependent variables, assumptions and boundary conditions for both the vertical and horizontal electrode which will be elaborated in the following subsections.

2.3.2. Flow Model

Various methods exists to model the flow of multiple phases within in a single domain. The trade-off for different flow models is computational effort and accuracy. The first distinction is between separated or dispersed multiphase models. Separated multiphase flow models use sharp phase boundaries to model the two separate phases in detail. Dispersed phase models uses volume fractions to describe the two different phases, while gas-liquid interactions are modelled as sinks and sources.

Secondly, multi-phase flow models can be distinguished by two different approaches, the Euler-Euler approach and the Euler-Lagrange approach. The distinction is that the Euler-Lagrange approach uses the particle as a reference frame while the Euler-Euler approach uses a fixed frame for reference. Using a Euler-Lagrange approach is inherent to using a separated multiphase flow model.

In this thesis detailed effects of gas-liquid interaction are not considered, because the computational cost is high while the accuracy gain is limited. Moreover, the momentum source and sinks of the dispersed phase models have reasonable accuracy to model bubble interactions. Therefore, an Euler-Euler approach is taken with a dispersed phase flow model.

Several dispersed multiphase flow models exist in COMSOL that follow an Euler-Euler approach:

1. Euler-Euler Model (EE)
2. Mixture Model (MM)
3. Bubbly Flow (BF)

In this thesis, an Euler-Euler approach is taken and the Mixture Model is used to study the effects of bubbles on the dissolved gas concentration.

The EE and MM model enables momentum exchange between the gas-liquid interface. The momentum exchange affects the velocity of the dispersed and continuous phase, which subsequently affects the distribution of dissolved gas concentration. This is not possible for the BF model. However, for the EE model the computational effort is higher than for the MM model. Due to the high non-linearity of the modelling, the MM model is more practical for solving the dissolved gas in the vicinity of the electrodes. Else the computational cost would limit the range of simulations.

Euler-Euler Model
The EE model consists of two phases, the dispersed phase and the continuous phase. Each phase is solved for their respective set of equations; the mass conservation equation and momentum equation (Navier-Stokes equation):

$$\frac{\partial \varepsilon_{\mathrm{d}}}{\partial t} + \nabla \cdot (\varepsilon_{\mathrm{d}} \mathbf{V}_{\mathrm{d}}) = 0 \tag{2.52}$$

$$\rho_{\mathrm{d}} \frac{\partial (\varepsilon_{\mathrm{d}} \mathbf{V}_{\mathrm{d}})}{\partial t} + \rho_{\mathrm{d}} \varepsilon_{\mathrm{d}} (\mathbf{V}_{\mathrm{d}} \nabla \cdot \mathbf{V}_{\mathrm{d}}) + \varepsilon_{\mathrm{d}} \nabla p + \nabla \cdot (\varepsilon_{\mathrm{d}} \mathbf{K}_{\mathrm{d}}) - \rho_{\mathrm{d}} \mathbf{g} = -\mathbf{M} \tag{2.53}$$

$$\mathbf{K}_{\mathrm{d}} = -\mu_{\mathrm{d}} (\nabla \mathbf{V}_{\mathrm{d}} + (\nabla \mathbf{V}_{\mathrm{d}})^T) - \frac{2}{3} \mu_{\mathrm{d}} (\nabla \mathbf{V}_{\mathrm{d}}) \cdot \mathbf{I} \tag{2.54}$$

$$\frac{\partial \varepsilon_{\mathrm{c}}}{\partial t} + \nabla \cdot (\varepsilon_{\mathrm{c}} \mathbf{V}_{\mathrm{c}}) = 0 \tag{2.55}$$

$$\rho_{\mathrm{c}} \frac{\partial (\varepsilon_{\mathrm{c}} \mathbf{V}_{\mathrm{c}})}{\partial t} + \rho_{\mathrm{c}} \varepsilon_{\mathrm{c}} (\mathbf{V}_{\mathrm{c}} \nabla \cdot \mathbf{V}_{\mathrm{c}}) + \varepsilon_{\mathrm{c}} \nabla p + \nabla \cdot (\varepsilon_{\mathrm{c}} \mathbf{K}_{\mathrm{c}}) - \rho_{\mathrm{c}} \mathbf{g} = \mathbf{M} \tag{2.56}$$

$$\mathbf{K}_{\mathrm{c}} = -\mu_{\mathrm{c}} (\nabla \mathbf{V}_{\mathrm{c}} + (\nabla \mathbf{V}_{\mathrm{c}})^T) - \frac{2}{3} \mu_{\mathrm{c}} (\nabla \mathbf{V}_{\mathrm{c}}) \cdot \mathbf{I} \tag{2.57}$$

$$\varepsilon_{\mathrm{d}} + \varepsilon_{\mathrm{c}} = 1 \tag{2.58}$$

ε_{d}	Volume fraction dispersed phase	[-]		ε_{c}	Volume fraction continuous phase	[-]
$\mathbf{V}_{\mathrm{d}}$	Mass-averaged velocity disp. phase	[m/s]		$\mathbf{V}_{\mathrm{c}}$	Mass-averaged velocity cont. phase	[m/s]
ρ_{d}	Density dispersed phase	[kg/m³]		ρ_{c}	Density continuous phase	[kg/m³]
$\mathbf{K}_{\mathrm{d}}$	Stress tensor dispersed phase	[N/m²]		$\mathbf{K}_{\mathrm{c}}$	Stress tensor continuous phase	[N/m²]
μ_{d}	Dynamic viscosity dispersed phase	[Pa· s]		μ_{c}	Dynamic viscosity continuous phase	[Pa · s]
p	Operation pressure (static)	[Pa]		$\mathbf{M}$	Interphase momentum exchange	[kg · m/s]
$\mathbf{I}$	Unit tensor	[-]		$\mathbf{g}$	Gravitational acceleration	[m/s²]

The solution for the dispersed and continuous phase in a continuum manner such as stated by the equations above implies that detailed information regarding single bubble behavior is not captured [64]. However, solving in a continuum manner is computational less demanding especially when higher dispersed fractions are present in the continuous flow field.

The set of equations for the dispersed and continuous phase can only be solved when $\mathbf{M}$ is known. The momentum transfer between the two phases depends on how the gas-liquid interface interact. Several works have investigated this gas-liquid interaction with help of semi-empirical correlations, which will be elaborated in section 2.3.2.

Mixture Model
The MM is a simplified version of the EE model. The EE model proved to be difficult to converge due to the two-way coupling of the momentum exchange between the dispersed and continuous phase [65]. The convergency issues can be minimized by simplifying the interphase momentum exchange through combining the dispersed and continuous Navier-Stokes which elimates the interphase momentum exchange M:

$$\frac{\partial (\rho_{\mathrm{d}} \varepsilon_{\mathrm{d}} \mathbf{V}_{\mathrm{d}} + \rho_{\mathrm{c}} \varepsilon_{\mathrm{c}} \mathbf{V}_{\mathrm{c}})}{\partial t} + \nabla \cdot (\rho_{\mathrm{d}} \varepsilon_{\mathrm{d}} \mathbf{V}_{\mathrm{d}}^2 + \rho_{\mathrm{c}} \varepsilon_{\mathrm{c}} \mathbf{V}_{\mathrm{c}}^2) + \nabla \cdot (\varepsilon_{\mathrm{d}} \mathbf{K}_{\mathrm{d}} + \varepsilon_{\mathrm{c}} \mathbf{K}_{\mathrm{c}}) + \nabla p - (\rho_{\mathrm{d}} + \rho_{\mathrm{c}}) \mathbf{g} = 0 \tag{2.59}$$

Also the mass conservation equations can be simplified by adding them together which eliminates the time dependency:

$$\nabla (\varepsilon_{\mathrm{d}} \mathbf{V}_{\mathrm{d}} + \varepsilon_{\mathrm{c}} \mathbf{V}_{\mathrm{c}}) = 0 \tag{2.60}$$

Eliminating the interphase momentum transfer M simplifies the model, but two equations and three unknown variables results in a not fully enclosed system. To reduce the unknown variables by one, the velocity of the dispersed phase and continuous phase can be combined to a mass-averaged mixture velocity $\mathbf{V}$ resulting in solvable closed system:

$$\mathbf{V} = \frac{(\rho_d \varepsilon_d \mathbf{V}_d + \rho_c \varepsilon_c \mathbf{V}_c)}{\rho} \tag{2.61}$$

The density of the mixture ρ is a combination of the dispersed and continuous volume fraction with their respective gas density:

$$\rho = \rho_d \varepsilon_d + \rho_c (1 - \varepsilon_d) \tag{2.62}$$

The momentum and continuity equation used in COMSOL is volume-averaged and not mass-averaged. Nigam [66] converted the momentum and continuity equation of the mixture model from mass-averaged to volume-averaged velocity:

$$\rho \frac{\partial \mathbf{U}}{\partial t} + \rho(\mathbf{U} \cdot \nabla)\mathbf{U} + (\rho_d - \rho_c)(\mathbf{U}_{slip} \nabla)\mathbf{U} = \nabla \cdot [-p\mathbf{I} + \mathbf{K}] - \nabla \cdot \mathbf{K}_m + \rho \mathbf{g} \tag{2.63}$$

where $\mathbf{U}$ is the volume-averaged (superficial) mixture velocity. The superficial mixture velocity is the superficial velocity of the continuous $\mathbf{U}_c$ and dispersed phase $\mathbf{U}_d$ combined:

$$\mathbf{U} = \mathbf{U}_c + \mathbf{U}_d = \mathbf{u}_c(1 - \varepsilon_d) + \mathbf{u}_d \varepsilon_d \tag{2.64}$$

where $\mathbf{u}_c$ and $\mathbf{u}_d$ are the actual continuous and dispersed phase velocity, respectively (also called interstitial velocity).

Because the interphase momentum transfer is eliminated, the gas-liquid interactions are captured by the superficial slip velocity:

$$\mathbf{U}_{slip} = \mathbf{U}_d - \mathbf{U}_c \tag{2.65}$$

The slip velocity is a result of the force balance existing between the dispersed and continuous phase which is very similar to interphase momentum transfer in the EE model. The added value of the MM is that the slip velocity can be computed explicitly decreasing the computational time and increasing the ease of convergency. The slip velocity will be elaborated in section 2.3.2.

The first stress tensor $\mathbf{K}$ in equation 2.63 is a result of the dispersed-dispersed and continuous-continuous shear forces:

$$\mathbf{K} = \mu(\nabla\mathbf{U} + (\nabla\mathbf{U})^T) - \frac{2}{3}\mu(\nabla\mathbf{U})\mathbf{I} \tag{2.66}$$

The second stress tensor $\mathbf{K}_m$ is caused by the gas-liquid interactions (slip velocities):

$$\mathbf{K}_m = (\rho_c + \rho_d - \rho)\mathbf{u}_{slip}\mathbf{U}_{slip}^T \tag{2.67}$$

where $\mathbf{u}_{slip}$ is the interstitial slip velocity.

where $\mathbf{u}_{slip}$ is the interstitial slip velocity.

The dynamic viscosity of the mixture μ stated in equation 2.66 can be approached by different models. The most common model is from Krieger et $al.$ [67]:

$$\mu = \mu_c \left(1 - \frac{\varepsilon_d}{\varepsilon_{max}}\right)^{-2.5\varepsilon_{max}\mu^*} = \mu_c \left(1 - \frac{\varepsilon_d}{\varepsilon_{max}}\right) \tag{2.68}$$

where $\mu^* = \frac{\mu_d + 0.4\mu_c}{\mu_d + \mu_c}$ and is assumed to approach 0.4 for $\mu_d \ll \mu_c$ and $\varepsilon_{max} = 1$. ε_{max} is the maximum packing concentration of the dispersed phase. This value is determined on experimental results or empirical relations.

The MM relies on the following assumptions [68]:

1. The density of each phase is approximately constant.
2. Both phases share the same pressure field.
3. The relative velocity between the two phases is essentially determined assuming a balance between the pressure gradient and viscous drag.

Gas-liquid interaction

The bubble behavior in the electrolyte is described by the drag experienced by the bubbles in the electrolyte. This behavior is expressed using volume forces (EE model) or slip velocities (MM and BF model). As mentioned, in this thesis the MM model is used and therefore only the slip velocities will be elaborated.

The relative superficial slip velocity $\mathbf{U}_r$ stated in equation 2.69 is a combination of various coupled gas-liquid interactions derived by Dahlkild [69] and further improved by Wedin and Dahlkild [67] which describes the relative bubble motion to the electrolyte. The derivation is based on the sedimentation of rigid spherical particles on a vertical surface. However, bubble behavior such as bubble coalescence, adherence to the electrode, bubble deformation, and bubble break-up are not considered in this derivation. Nonetheless, the derivation is a fine approximation of the relative bubble motion as for AWE the hydrogen bubbles in the electrolyte are small, persist to be spherical, and do not simply coalesce [28]. Although this not holds for oxygen bubbles as they grow bigger and coalescence more easily, it remains a good approximation. The bubble motion defined by Schillings et.al [36] uses a set of equations that determine the slip velocity:

$$\mathbf{U}_r = \mathbf{U}_{\text{stokes}} + \mathbf{U}_{\text{Smig}} + \mathbf{U}_{\text{Sdiff}} + \mathbf{U}_{\text{Hdiff}} + \mathbf{U}_{\text{Saff}} \tag{2.69}$$

The first term $\mathbf{U}_{stokes}$ in the superficial relative velocity is the Stokes' flux. The Stokes' flux is a result from a force balance between the drag and buoyancy forces. The Stokes' velocity stated in equation 2.70 is the terminal rising velocity of a single bubble

$$\mathbf{U}_{\text{stokes},1} = \frac{2gr_{\text{b}}^2}{9\nu_c} \tag{2.70}$$

where g is the gravity constant, r_{b} is bubble radius, and ν_c is the kinematic viscosity of the continuous phase. Nicolai [70] states that the Stokes' velocity for a single bubble is affected by its nearby bubbles and is corrected by a hindrance function:

$$f(\varepsilon_{\text{d}}) = (1 - \varepsilon_{\text{d}})^5 \tag{2.71}$$

However, the effect of neighbouring interacting bubbles (also known as swarm effect) is strongly affected by the gas fraction. At gas fractions of 0.4 or higher the swarm effect is likely to be overpredicted. The Stokes' velocity for the swarm of bubbles is:

$$\mathbf{U}_{\text{stokes}} = \varepsilon_{\text{d}} f(\varepsilon_{\text{d}}) \mathbf{U}_{\text{stokes},1} \mathbf{e}_z \tag{2.72}$$

where $\mathbf{e}_z$ is the unity vector in the vertical direction, the opposite of the gravity direction.

The second and third term relate the collision frequency of the bubbles to the dispersed phase and the shear along the vertical electrode as reported Leighton et al. [71] and Schaflinger[72]. $\mathbf{U}_{\text{Smig}}$ is the shear-induced migration for non-uniform shear stresses:

$$\mathbf{U}_{\text{Smig}} = -r_{\text{b}}^2 |\dot{\gamma}| \frac{\kappa(\varepsilon_{\text{d}})}{\tau} \nabla\tau \tag{2.73}$$

where $|\dot{\gamma}| = \frac{\partial \mathbf{U}_z}{\partial x}$ is the flow shear rate between two vertical plates, $\kappa(\varepsilon_{\text{d}}) = 0.6\varepsilon_{\text{d}}^2$ is a non-dimensional coefficient, and $\tau = \mu \frac{\partial \mathbf{U}_z}{\partial x}$ is the shear stress along the flow direction.

The third term is the shear-induced diffusion that originates from the generated bubble concentration gradient in a constant shear

$$\mathbf{U}_{\text{Sdiff}} = -r_{\text{b}}^2 |\dot{\gamma}| \beta(\varepsilon_{\text{d}}) \nabla\varepsilon_{\text{d}} \tag{2.74}$$

where $\beta(\varepsilon_{\text{d}}) = \frac{1}{3}\varepsilon_{\text{d}}^2(1 + 0.5e^{8.8\varepsilon_{\text{d}}})$, and is another non-dimensional coefficient. The fourth term is the hydrodynamic self-diffusion. and describes the irregular bubble motion in a bubble plume.

$$\mathbf{U}_{\text{Hdiff}} = -r_{\text{b}} \mathbf{U}_{\text{stokes},1} f(\varepsilon_{\text{d}}) \mathbf{D} \nabla\varepsilon_{\text{d}} \tag{2.75}$$

where $\mathbf{D}$ is a 2x2 matrix describing the non-isotropic dimensionless dispersion coefficient

$$\mathbf{D} = \begin{bmatrix} D_\perp & 0 \\ 0 & D_\parallel \end{bmatrix} \tag{2.76}$$

where $D_\perp = 1$, and $D_\parallel = 8$, both remain fairly constant and are independent of ε_d. The isotropic values are empirically determined by Nicolai et al. [70].

The last term is the Saffman's lift flux caused by the rotation of the bubbles in a sheared flow. It is derived from Saffman's lift velocity [73].

$$\mathbf{U}_{\text{Saff}} = -\varepsilon_d f(\varepsilon_d) \mathbf{U}_{\text{stokes},1} |\dot{\gamma}| \frac{6.46}{6\pi} \sqrt{\frac{r_b^2 |\dot{\gamma}|}{\nu_c}} \mathbf{e}_x \tag{2.77}$$

The lift forces generated by Stokes's and Saffman's velocity tend to push the bubbles towards the lowest velocities.

2.3.3. Adherence Region Model

As depicted in figure 2.4 the bubbles are adhered to the electrode surface. It is assumed that this layer of adhered bubbles is static and acts as a porous region. The bubbles act as the porous matrix and the voids between the bubbles as the pores which are filled with the electrolyte.

The adherence region model is part of the flow model because the adherence region model affects the flow characteristics in the adherence region and are governed by the flow model. The characteristic flow in the adherence region can be described by Darcy's law because Reynolds number is below 10. This law describes the linear relationship between the mixture velocity field $\mathbf{U}$ and the gradient of the pressure p [74]:

$$\mathbf{U} = -\frac{\kappa}{\mu} \nabla p \tag{2.78}$$

where κ (m^2) is the permeability in the adherence region, and μ_c is the electrolyte dynamic viscosity. Darcy's law is affected by two variables; the permeability and the porosity which describes the ratio of void (pore) volume to the total volume

$$\varepsilon_p = \frac{V_{\text{ad}} - V_{\text{bubbles}}}{V_{\text{ad}}} = 1 - \varepsilon_d = \varepsilon_c \tag{2.79}$$

where V_{ad} is the total volume of the adherence region and V_{bubbles} is the total bubble volume in the adherence region.

Different models exist that can describe the permeability in the porous region for different regimes of Reynolds. The Kozenzy-Carman relation is used which describes the flow through packed beds, because Re < 10. This relation estimates the permeability of the porous region from the average particle diameter d_p and porosity ε_p [74]:

$$\kappa = \frac{d_p^2}{180} \frac{\varepsilon_p^3}{(1 - \varepsilon_p)^2} = \frac{4 r_b^2}{180} \frac{\varepsilon_c^3}{(1 - \varepsilon_c)^2} \tag{2.80}$$

The fluid flow between the fluid in the adherence region and the fluid in the bulk experiences a continuity in velocity and shear. However, this is not necessarily the case between the gas particle in the adherence region and the fluid in the bulk. Therefore, the averaged shear between the adherence region and bulk is not always continuous [30]. Ochoa-Tapia and Whitaker [75, 76] suggested a discontinuity in the averaged shear at the boundary while maintaining continuity in velocity. It is assumed that the inertial effect in the adherence region are negligible.

The stress jump boundary condition between the adherence region and bulk:

$$\mu \frac{d(\mathbf{U}_{c,\text{ad}})}{dx} - \mu_c \frac{d(\mathbf{U}_{c,\text{bulk}})}{dx} = \beta_j \frac{\mu_c}{\kappa^{(1/2)}} \mathbf{U}_{c,ad} \quad \text{at} \quad x = 2r_b \tag{2.81}$$

where β_j is the stress jump coefficient. The continuity boundary conditions is as followed: 2.82.

$$\mathbf{U}_{c,\text{bulk}} = \mathbf{U}_{c,\text{ad}} \quad \text{at} \quad x = 2r_b \tag{2.82}$$

As stated in equation 2.81 the discontinuity is expressed in the last term if $\beta_j \neq 0$. Ochoa-Tapia and Whitaker [75, 76] noted that β_j is in the order of one and the sign can be either positive or negative.

The relation used by Kuznetsov [30] expresses the relation of permeability to the adherence region thickness with Darcy's number (Da_H):

$$Da_H = \frac{\kappa}{4r_b^2} \tag{2.83}$$

In figure 2.6 the effect of the stress jump coefficient on the interfacial velocity for various Darcy's numbers is illustrated. For Darcy's numbers 0.1, which is applicable for very small gas bubbles, the effect on the velocity profiles is significant.

The importance of the stress jump is that it affects the velocity profiles and therefore the dissolved concentration uptake towards the bubbles and bulk.
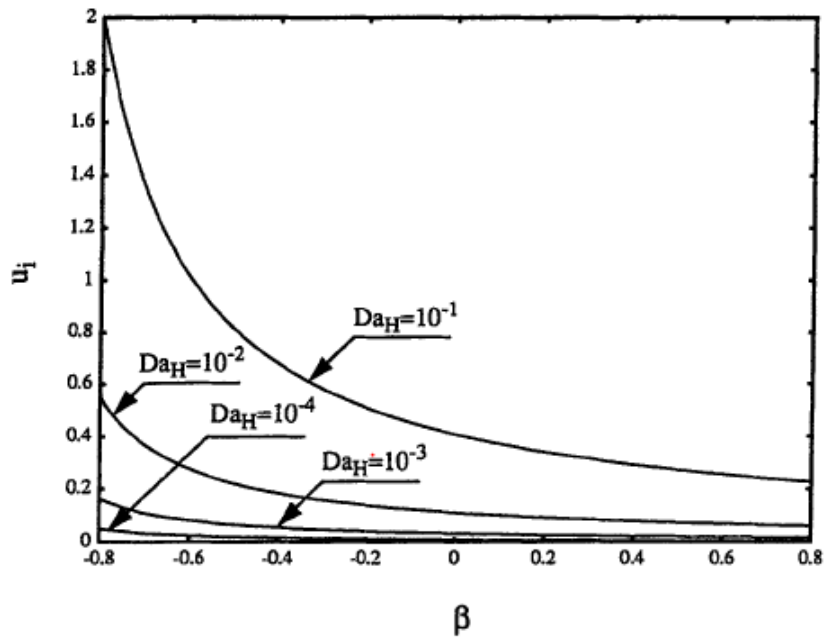
Figure 2.6: The interfacial velocity $\mathbf{u}_i$ against the adjustable coefficient β_j in the stress boundary condition for different permeability dependencies Da_H [30]

.

2.3.4. Species Model

The aim of the species model is to capture the evolution of the dissolved gas concentrations in the vicinity of the electrode surface.

Two species models exist that can describe the concentration evolution in a designated fluid domain; the concentrated and diluted species model. The key difference is that the species concentrations in the diluted species model are small compared to the solvent fluid. As a general-principle, a mixture containing various species is considered dilute when the concentration of the solvent is 90 mol% or more [77]. Due to the diluted assumption the mixture properties can be assumed to be nearly equal to the solvent fluid properties such as density and viscosity.

In electrolysis the vicinity of the electrode surface is supersaturated due to generated dissolved gas. This layer of supersaturated dissolved gas affects the concentration overpotential, and the growth of the bubbles. The latter is not taken into account. In this thesis, the diluted species model is used to take the dissolved concentration effects in to account and enables to compute concentration fields for dissolved hydrogen and oxygen.

The evolution of the chemical species in the diluted species model depends on three driving forces; diffusion, migration, and convection. Migration effects can be neglected, because no supporting electrolyte is present as a chemical species such as hydroxide or hydrogen ions. The resulting governing equation for the chemical species is:

$$\frac{\partial c_i}{\partial t} + \mathbf{U} \cdot \nabla c_i - D_i \nabla^2 c_i = S_i \tag{2.84}$$

where the second term is transport by diffusion determined by Fick's law, the third term is transport by convection determined by the mixture model flow field, and the last term is the consumption/production term S which is the same as in equation 2.21 of the analytical model. S_i is the sink term which uptakes the dissolved concentration generated at the electrode surface by the bubbles.

The S_i term 2.84 not only represents a sink term for the dissolved gas but also a source term for the generated dissolved hydrogen and oxygen concentration based on the electrochemistry. The sink term is defined in equation 2.21 and the overall mass transfer coefficient in equation 2.51. The source term for the dissolved gas is:

$$S_i = \frac{\nu_i i_{\text{loc}}}{z_i F} \tag{2.85}$$

where ν_i is the stoichiometric coefficient, and i_{loc} is the local current density at the electrode wall. The stoichiometric coefficient is based on the half reactions:

$$\begin{aligned} \Sigma_{\text{ox}} |\nu_{\text{ox}}| \text{Ox} + z_i e^- &\rightleftharpoons \Sigma_{\text{red}} \quad &\nu_{\text{red}} \text{Red} \\ \nu_{\text{ox}} < 0 \quad &\quad &\nu_{\text{red}} > 0 \end{aligned} \tag{2.86}$$
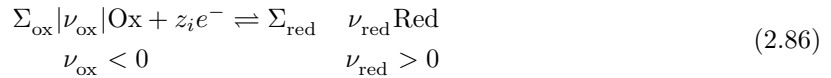
For the HER (anode); $\nu_{\text{ox}} = 0$, $z_i = 2$, and $\nu_{\text{red}} = 1$ and for the OER (cathode); $\nu_{\text{ox}} = -1$, $z_i = 4$, and $\nu_{\text{red}} = 0$.

Tracker species

Two more chemical species are used next to the dissolved hydrogen c_{H_2} and oxygen c_{O_2} which are the hydrogen and oxygen tracker species, $c_{\text{H}_2,\text{track}}$ and $c_{\text{O}_2,\text{track}}$, respectively. The tracker species are used to track the tracker concentration flux, $\mathbf{N}_{\text{track}}$, near the electrode wall. This enables to study the natural free convection using k_{n}:

$$k_{\text{n}} = \frac{N_{\text{track}}}{\Delta c_{\text{track}}} \tag{2.87}$$

The reason not using the dissolved species to compute their respective natural free convection is that the dissolved concentration is consumed by the sink term S and therefore affecting the dissolved concentration flux.

Also, the dissolved concentration affects the local current density through the Nernst equation and the Butler-Volmer equation. The local current density subsequently affects the rate of production of dissolved species and thus the concentration. This eventually alters the dissolved concentration flux. Therefore a tracker species is used that does not affect the uptake nor the local current density, but still follows the flow profile.

2.3.5. Electrochemical Model

The last additional phenomena in electrolysis is electrochemistry. The majority of the electrochemistry is explained in section 2.1.1 and applies to the numerical model. However, for numerical modelling three different approaches can be taken to describe the current distribution. The current distribution approach helps to make a balanced approach between computational effort and accuracy with respect to the electrode kinetics.

The electrochemistry in the electrolyte and electrodes in an electrochemical cell as depicted in figure 2.1 can be classified in three different current distribution classes. These classes are the primary, secondary, and tertiary current distribution. Each distribution class has different approximations which have different effects on the solution conductivity, electrode kinetics, and mass transport.

The primary current distribution model only requires the Nernst equation to describe the electrode surface potential. However, it does not solve for electrode kinetics nor for the reactant chemical species. The secondary current distribution makes use of the Nernst equation and various electrode kinetics such as the extended Butler-Volmer equation. It does not inlcude the mass transport of the supporting electrolyte. The tertiary current distribution includes the nernst equation, electrode kinetics, and the mass transfer of the supporting electrolyte. The latter makes the tertiary current distribution highly non-linear.

All three current distributions assume electroneutrality and ohm's law. Ohm's law can be used because the potential gradient at an infinitesimally scale is linear.

This thesis work will use a secondary current distribution model, because the concentration of the supporting electrolyte (KOH) is significantly higher than the dissolved gas concentrations. With an electrolyte concentration of 6 molar we assume that the concentration of OH^- is not limiting the reaction at the anode.

3

Modelling

The research goal of this thesis is to improve the understanding of the local effects such as local current density and bubble motion on dissolved gas concentrations. To achieve this goal, the modelling chapter describes how the research questions will be answered with the help of the analytical and numerical model theory explained in chapter 2.

The analytical model provides a better insight how the Hatta number, mass transfer boundary layer, and current density affect the dissolved gas concentration and gas evolution efficiency. Also, a database is built with data of previous works to understand if any trends can be discovered for vertical and horizontal electrodes for both alkaline and acidic conditions. The database is provided in Appendix B. In parallel a COMSOL model is built to capture the flow dynamics, electrochemical behavior and the transport of the chemical species in water electrolysis to analyze the local effects on the dissolved concentration near the electrode walls. Moreover, the geometry setup, material properties, assumptions and boundary conditions, mesh and modelled results will be explained.

3.1. Analytical Model Setup

A database is made for the various literature works on dissolved gas concentration for alkaline and acidic conditions. The database provides an understanding of the development of the dissolved gas concentration for horizontal and vertical electrodes in alkaline and acidic conditions. Moreover, the database acts as a validation tool and helps to find any physical gaps in the analytical model. Furthermore, an independent parameter analysis is performed on the electrode properties to grasp the significance of each electrode property on the dissolved gas concentration and gas evolution efficiency stated in equation 2.27, 2.31 and 2.32.

The material properties and operation conditions applicable for the analytical modelling are defined in section 3.2.3. The geometry variables are listed below and are based on the experimental setup of Janssen *et al.* [28].

Parameter	Property	Value	Dimensions
l	Inter-electrode width	0.006	[m]
H	Electrode height	0.1	[m]
$\overline{A}_{H_2}$	real effect mass transfer surface coverage H_2	0.21	[-]
$\overline{A}_{O_2}$	real effect mass transfer O_2	1.4	[-]
f_g	gas evolution efficiency	0.5	[-]

The results that can be obtained from the analytical model are listed below:

- The gas evolution efficiency can be predicted with experimental data
- An independent parameter study can be performed to analyze the effects of single parameters on the gas-evolution efficiency and the concentration profiles
- An analysis can be done for limiting cases such as current density or bubble nucleation site density.

24

- Free natural convection and bubble-induced mass transfer coefficients can be computed and compared with the numerical model (experimental maybe?)
- The concentration profiles can be predicted with experimental data

3.2. Numerical Model Setup

This section elaborates the specifications of the numerical model and simulations; the electrode geometry, material properties, the various physical models, their respective assumptions and boundary conditions, the extra implemented functionality, and the meshing.

3.2.1. Electrode geometry

The electrode geometry consist of an inlet region, two vertical electrodes, and an outlet region illustrated in figure 3.1. The dimensions of the vertical electrode setup are shown in table 3.1. The geometry is based on the work of Janssen *et al.* [28] in order to validate numerical results with the analytical model and the experimental data.
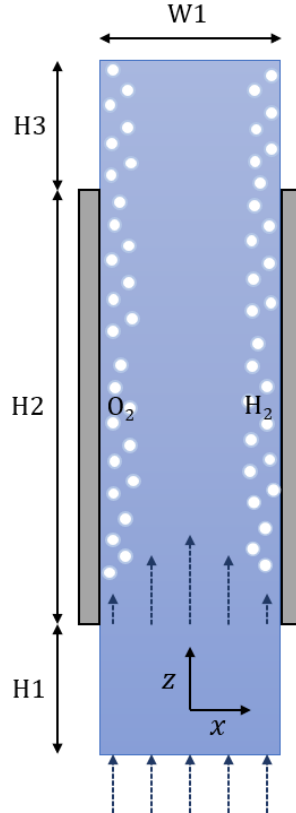
Figure 3.1: The vertical geometry used in numerical simulations. The vertical geometry is based on the experimental setup of Janssen *et al.* [28]. The geometry is not drawn to scale.

Parameter	Value	Dimensions	Parameter	Value	Dimensions
H1	20	mm	W1	6.0	mm
H2	100	mm			
H3	20	mm			

Table 3.1: The dimensions of the vertical geometry.

3.2.2. Numerical Model Physics

The applied physics in the numerical model are the mixture model, adherence region model, electrochemical model, and diluted species model. The different models are explained in Chapter 2. The setup and coupling effects of the different models are illustrated in figure 2.5. Each model has their own set of boundary conditions which will be illustrated in the following sections. The material properties and the operations conditions that are applicable for the various models are listed in section 3.2.3.

Several assumptions are made for the mixture and adherence region model used in modelling the flow field. These assumptions reduce the computational effort while minimizing accuracy losses.

- The flow field is assumed to be isothermal
- The flow field is assumed to be two dimensional (2D)
- The flow field is assumed to be laminar.
- The mixture fluid is assumed to be incompressible and Newtonian.
- The bubble radius is assumed to be constant and independent of current density.
- The bubbles are assumed to not coalescence or break-up.
- The inertial effects in the adherence region are assumed to be negligible.
- The bubbles are assumed to be static in the adherence region. However, the release of bubbles still constitutes to micro-mixing.

Solving the Navier-Stokes (2.59) and the mass continuity (2.60) equations requires properly defined initial conditions and boundary conditions. The initial conditions consist of initial inlet velocity, initial gas fraction, and initial pressure. The boundary conditions consist of wall (no-slip) boundaries, gas flux inlets, inlet velocity, and an outlet pressure. The boundary conditions for the mixture model and adherence region model are illustrated in figure 3.2.
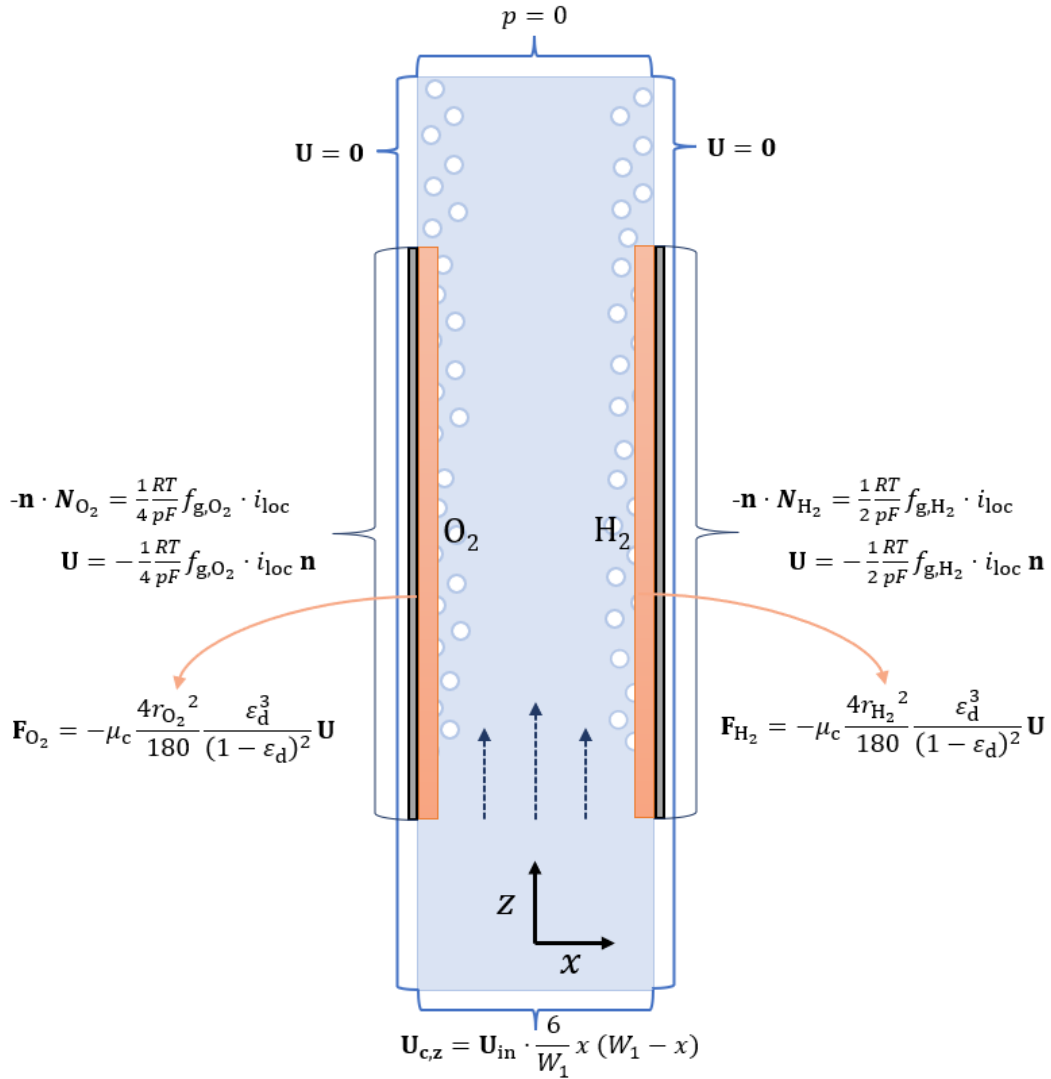
Figure 3.2: Schematic overview of the boundary conditions and momentum sinks applied in the mixture model and the adherence region model, respectively.

The finer details regarding the boundary conditions are elaborated in Appendix C in section C.1.

The diluted species model computes the dissolved gas concentration of hydrogen and oxygen, and the hydrogen and oxygen tracker species. The flow field affects the convection in the diluted species model, and the local current density from the electrochemical model influences the dissolved gas production rate. For the diluted species model several assumptions are made:

- It is assumed that the dissolved gas flux enters the domain in the same quantity as the gas flux. However, a part of the dissolved gas is taken up by the sink term derived in the analytical modelling section 2.2 in equation 2.21.
- It is assumed that the species model is diluted, because the total dissolved concentration of all species is ≤ 10 mol% of the total mixture.
- It is assumed that the tracker species completely reacts at the electrode wall

Also, the concentration equation requires well defined initial conditions, boundary conditions, and sinks. The initial conditions consist of an initial concentration for each species. The boundary conditions consist of four no-flux boundaries, a single fixed concentration inlet, a single outlet, two fixed concentrations for the tracker species, and two dissolved gas inlets at the electrodes. The sinks are defined within the gas evolution domain (green domain). The boundary conditions, and sinks for the diluted species model are shown in figure 3.3. The initial concentration is equal to the fixed concentration inlet:
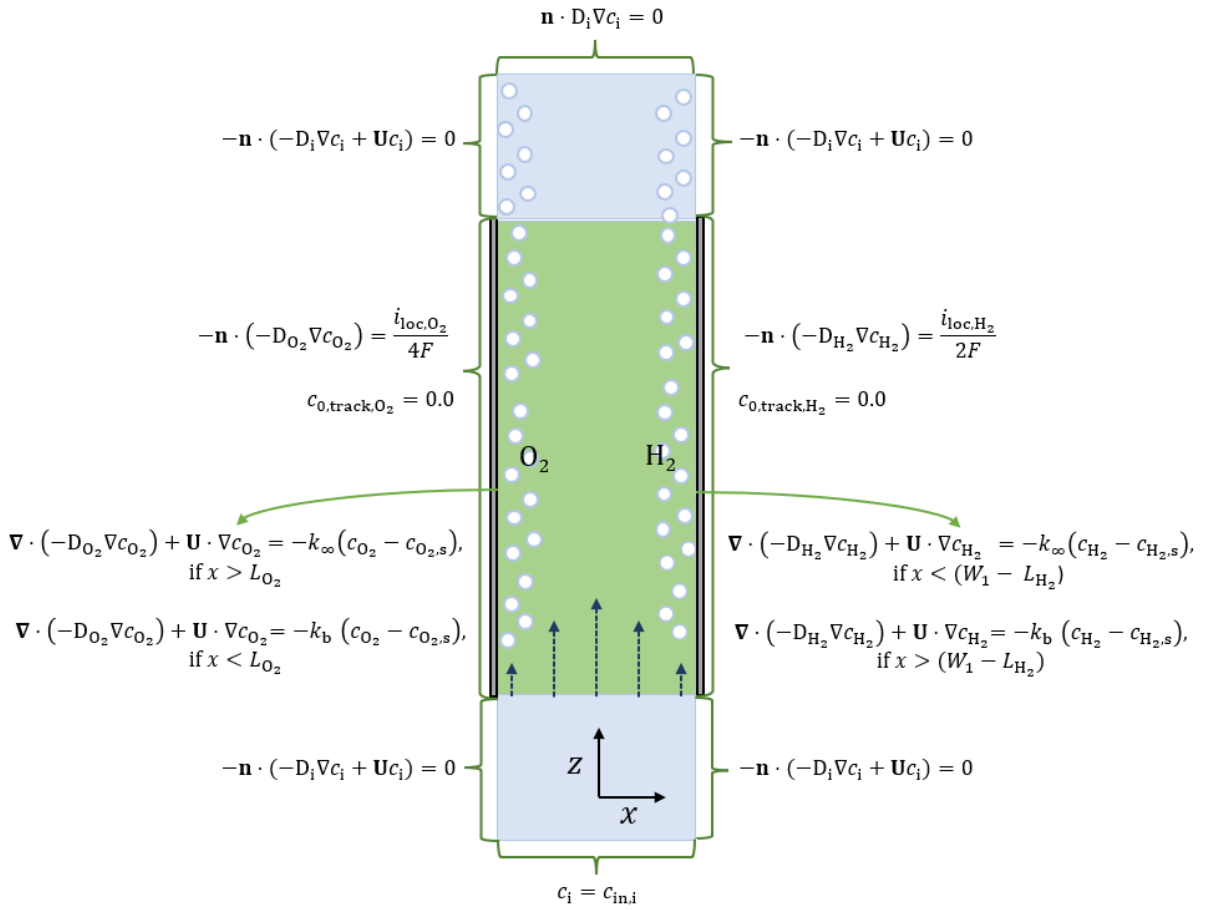
Figure 3.3: Schematic overview of the boundary conditions and concentration sinks in the diluted species model.

$$
\begin{aligned}
c_{H_2,initial} = c_{in,H_2} = && c_{s,H_2} &= 0.794 \quad [\text{mol/m}^3] \\
c_{O_2,initial} = c_{in,O_2} = && c_{s,O_2} &= 1.26 \quad [\text{mol/m}^3] \\
c_{H_2,track,initial} = && c_{in,H_2,track} &= 1.0 \quad [\text{mol/m}^3] \\
c_{O_2,track,initial} = && c_{in,O_2,track} &= 1.0 \quad [\text{mol/m}^3]
\end{aligned}
\tag{3.1}
$$

The sink term, initial conditions, and boundary conditions are stated in section C.2 in Appendix C.

The last physics is the electrochemical model and solves for the local current density and the required voltage potential. For the electrochemical model several assumptions hold:

- The total charge within the electrolyzer is assumed to be zero; electroneutrality. Electroneutratlity holds for scales larger than nanometers [78].
- The electrolyte current is assumed to follow Ohm's law, because of electroneutrality and small electrolyte concentration gradients of the ions in the electrolyte.
- The electrolyte conductivity is assumed to be isotropic, but is corrected with the Bruggeman correlation for gas fraction.
- No supporting electrolyte present (KOH) that can affect the electrode kinetics and thus the activation overpotential.

The initial conditions of the electrochemical model are the electrolyte potential ϕ_l and the electrode potential ϕ_s. The applied boundary conditions are six insulation boundaries, one applied electrode potential, and one applied current density. The insulation boundary states that no electrolyte current i_l nor electrode current i_s can pass normal to the respective boundary. The applied electrode potential boundary for the cathode is set to 0 V and must overcome the equilibrium potential to start electrolysis. In figure 3.4 a schematic overview of the boundary conditions is shown for the electrochemical model.
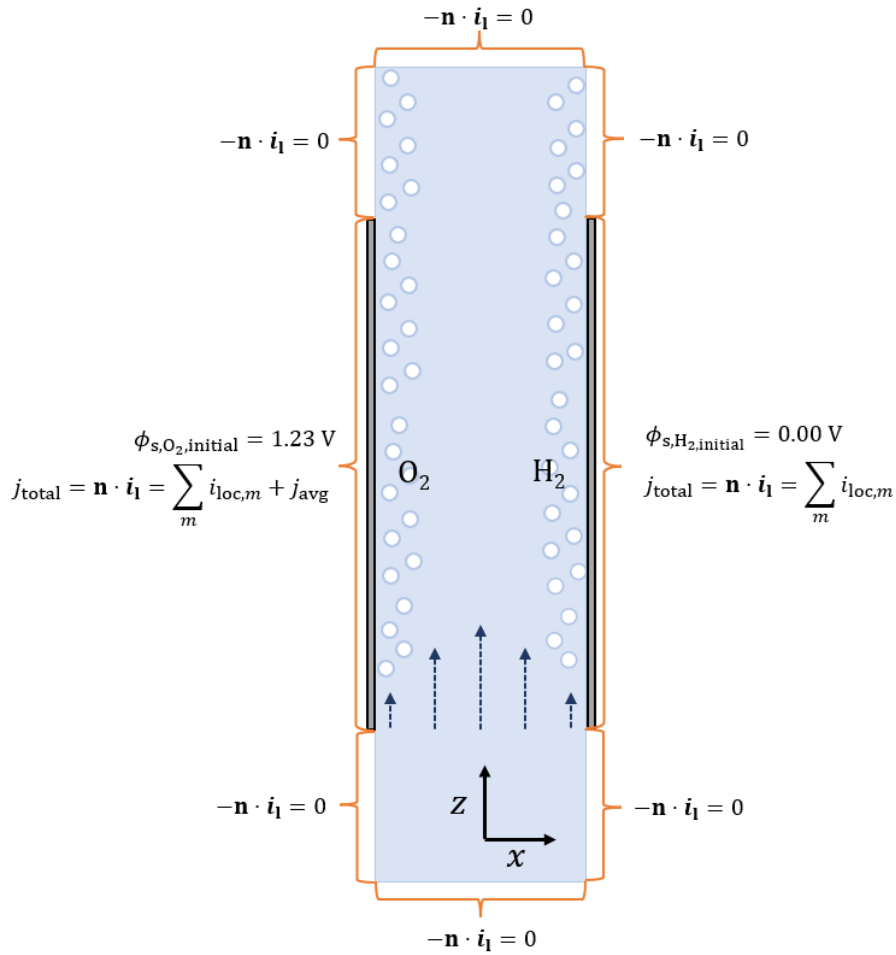
Figure 3.4: Schematic overview of the boundary conditions and the applied current density in the electrochemical model.

The initial conditions for within the domain:

$$\phi_{l,\text{initial}} = 0 \quad \text{V}$$
$$\phi_{s,\text{initial}} = 0 \quad \text{V}$$

$$(3.2)$$

The boundary condition set for the anode (OER) states the total current density at the electrode-electrolyte interface is equal to the sum of all local current densities for m reactions and the applied average current density. The sum of all local current densities is a result of the applied voltage between the anode and cathode. The sum of all local current densities for an initial potential difference of 1.23 V is 0.00 A/m^2. However, applying an average current density higher than 0 A/m^2 results in a voltage difference higher than 1.23 V due to ohmic losses and the and electrode kinetics. This increased potential difference rearranges the sum of all local current densities through the Butler-Volmer equation resulting a shift in the voltage difference between the electrodes.

The boundary conditions are stated in section C.3 in Appendix C.

3.2.3. Material Properties and Operation Conditions

The continuous phase or electrolyte in the flow domain is KOH with a concentration of $1.0 \cdot 10^3$ mol/m^3. The electrolyte concentration is consistent with the experiments performed by Janssen *et al.* [27, 28] which will be used as a comparison to the numerical model. The dispersed phase consists of oxygen and hydrogen gas. All parameters dependent on temperature, pressure and KOH concentration are corrected for T = 303K, 1 atm, and 1M KOH. The material properties of the continuous and dispersed phase are provided in table 3.2 below:

Parameter	Property	Value	Dimensions
ρ_{c}	density electrolyte	1050	kg/m^3
$\rho_{\mathrm{d,O_2}}$	density hydrogen	0.0799 [79]	kg/m^3
$\rho_{\mathrm{d,H_2}}$	density oxygen	1.27 [80]	kg/m^3
μ_{c}	dynamic viscosity electrolyte	$1.129 \cdot 10^{-3}$ [81]	Pa $\cdot$ s
$\mu_{\mathrm{d,H_2}}$	dynamic viscosity hydrogen	$0.90 \cdot 10^{-5}$ [82]	Pa $\cdot$ s
$\mu_{\mathrm{d,O_2}}$	dynamic viscosity oxygen	$2.1 \cdot 10^{-5}$ [82]	Pa$\cdot$ s
r_{b}	bubble radius	$50 \cdot 10^{-6}$	m
T	operating temperature	303	K
p	operating pressure	$1.01325 \cdot 10^5$	Pa
σ	electrolyte conductivity	23 [83]	S/m
$E^{\circ}_{\mathrm{eq,H_2}}$	Reference equilibrium potential hydrogen	0.00	V
$i^{\circ}_{\mathrm{0,H_2}}$	ECD, hydrogen oxidation	100	A/m^2
$c_{\mathrm{s,H_2}}$	maximum solubility hydrogen	0.794 [84]	mol/m^3
α_{a}	CTC, anodic	0.5	-
$E^{\circ}_{\mathrm{eq,O_2}}$	Reference equilibrium potential oxygen	1.23	V
$i^{\circ}_{\mathrm{0,O_2}}$	ECD, oxygen reduction	1.00	A/m^2
$c_{\mathrm{s,O_2}}$	maximum solubility oxygen	1.26 [85]	mol/m^3
α_{c}	CTC, cathodic	0.5	-
$D_{\mathrm{H_2}}$	Diffusion coefficient hydrogen	$3.0 \cdot 10^{-9}$ [86]	m^2/s
$D_{\mathrm{O_2}}$	Diffusion coefficient oxygen	$1.9 \cdot 10^{-9}$ [85]	m^2/s
$D_{\mathrm{H_2,track}}$	Diffusion coefficient hydrogen tracker	$3.0 \cdot 10^{-9}$ [86]	m^2/s
$D_{\mathrm{H_2,track}}$	Diffusion coefficient oxygen tracker	$1.9 \cdot 10^{-9}$ [85]	m^2/s

Table 3.2: Material properties and operation conditions

In appendix B the temperature and KOH dependency for the diffusion coefficient of dissolved hydrogen and oxygen are illustrated in figures B.1 and B.2, respectively.

3.2.4. Mesh

The meshing is an important step for numerical simulations and has a direct effect on the solution accuracy and computation time. The meshing defines how the nodes and how many nodes (finite elements) are positioned in the geometry, see figure 3.5.
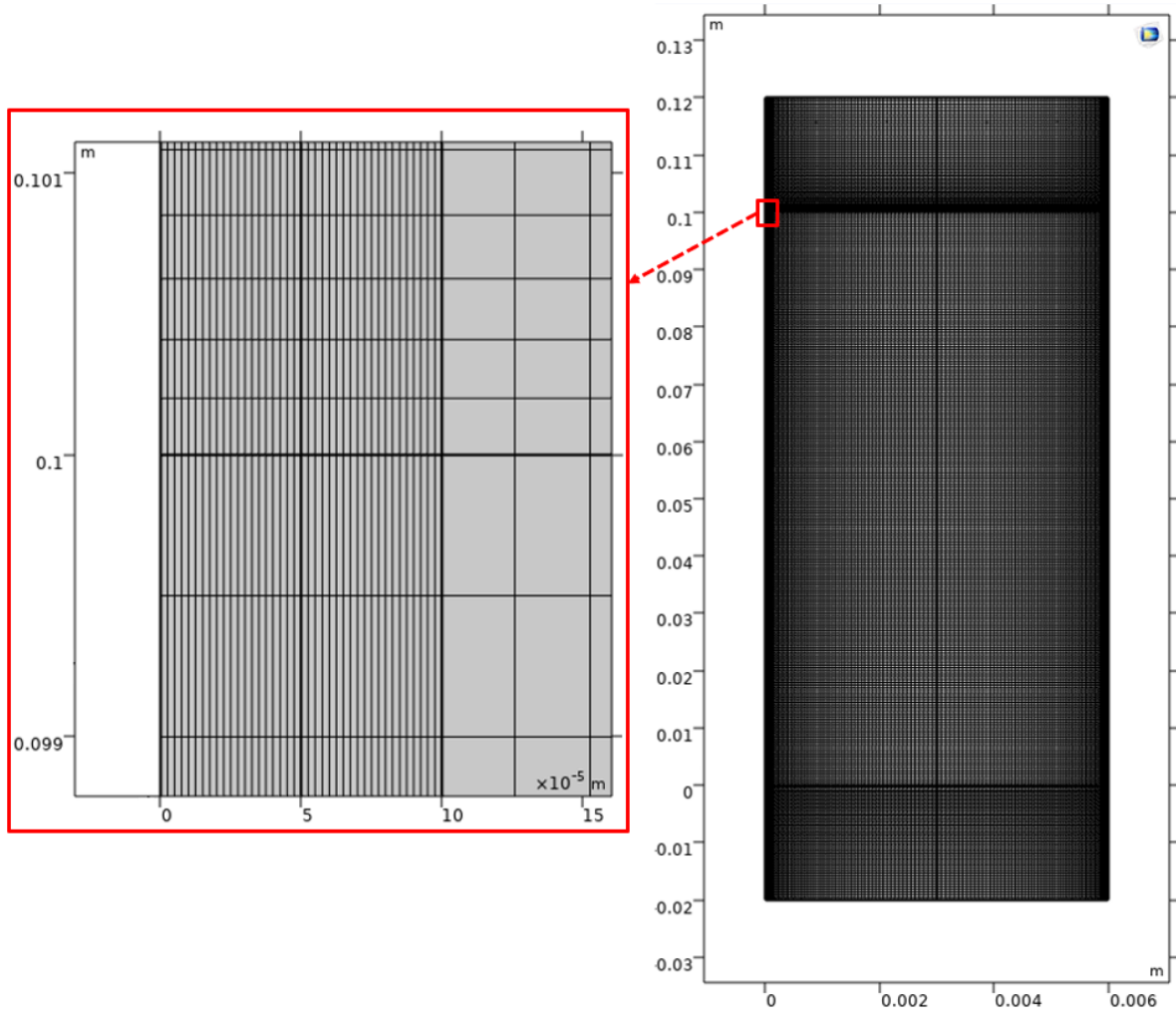
Figure 3.5: The meshing distribution of the vertical channel based on the experimental setup of Janssen *et al.* [28]. The full domain is meshed as 300 x 240 nodes while the nodes in each adherence region (left) consist of 40 x 200 nodes. The mesh distribution within the adherence region is more refined and is the same size as the bubble diameter . The nodes in the adherence regions are 500 x 2.5 micrometer. The inlet and outlet region each have 50 x 240 nodes.

The meshing was built using a mapped distribution. Mapped distribution gives control over how the nodes and how many nodes are distributed in the geometry. Also, options such as element ratio which increases the nodes length relative to its neighbouring node by that specific ratio.

The node distribution near the electrode walls haven been optimized and require an extremely fine mesh to capture the no-slip effects and the mass transfer boundary layer (L). The latter is required to accurately model the sink term of the dissolved gas. The width of the nodes near the electrode wall are 2.5 microns while the radius of a single bubble varies from 25 to 75 microns. The node size remains the same if the bubble radius is altered during simulations. The height of the nodes in the adherence region are 500 micrometers.

The meshing at the middle of domain can be fairly coarse, but the shift from 2.5 micrometer nodes to 50 micron nodes could lead to convergency problems due to improper interpolation between the nodes. The specific element ratio used in the gas evolving domain is 3.0

The node distribution along the height of electrode at the inlet and outlet region is finer than in the gas evolving domain. This improves the current distribution at the bottom and top of the electrode which

prevents extreme local current densities at the corners of electrode. The specific element ratio used in the inlet and outlet region is 1.5.

Moreover, all nodes have an angle of 90°which helps to increase accuracy and stabilize the numerical convergency more quickly. Nodes that do not have angles of 90 °are skewed and highly skewed elements decrease the accuracy and increase numerical instabilities.

4

Results

In this section the results of the analytical model and numerical model are presented and discussed. The analytical model uses experimental data from Janssen *et al.* [28] to predict the gas evolution efficiency and dissolved gas concentration. Moreover, an independent parameter study is performed to get a better understanding of the effects on gas-evolution efficiency and dissolved gas concentration. Furthermore, a database is presented in Appendix D which is made from various literature works on dissolved gas concentration. The database is used to distinguish trends for dissolved gas concentration. The numerical model evaluates the electrochemical, flow, and species characteristics to get a better understanding on the evolution of the dissolved concentration near the electrode wall.

4.1. Analytical Model

The theory used for the analytical model is explained in section 2.2.

To predict the gas-evolution efficiency and dissolved concentration a set of parameters must be known; the nucleation site density (n [1/m^2]), the bubble radius (r_b), and surface coverage (θ). Both oxygen and hydrogen have their own set of parameters. The experimental data of Janssen *et al.* [28] provides this set of parameters and are presented in Appendix D. Based on the experimental data a power correlation for nucleation site density (1/m^2) and current density (A/m^2) is made for various inlet velocities:

$$
\begin{aligned}
\text{H}_2 &: n = 226.65 \cdot & j^{2.1314} & \quad \& \quad v = 0.0 \quad [\text{m/s}] \\
\text{O}_2 &: n = 74894 \cdot & j^{0.9151} & \quad \& \quad v = 0.0 \quad [\text{m/s}] \\
\text{H}_2 &: n = 155.30 \cdot & j^{2.1311} & \quad \& \quad v = 0.3 \quad [\text{m/s}] \\
\text{O}_2 &: n = 27207 \cdot & j^{1.0106} & \quad \& \quad v = 0.3 \quad [\text{m/s}]
\end{aligned}
\tag{4.1}
$$

Figures 4.1 and 4.2 show the power curves in a log-log plot of the nucleation site density against the current density for a free and forced flow mentioned in the above equation. Also, the experimental data of Janssen *et al.*[28] is plotted to assess the relevance of the power curves.
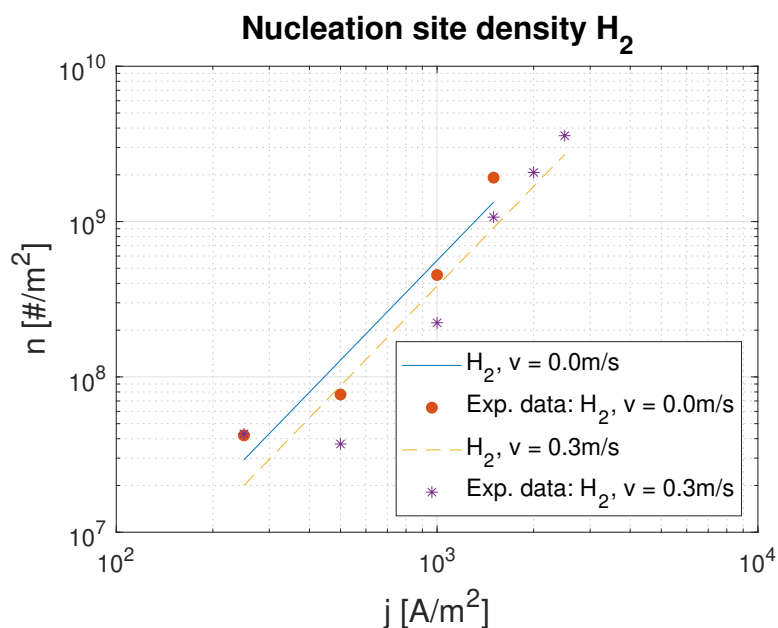
Figure 4.1: A log-log plot of the nucleation site density n against the current density j for an hydrogen evolving vertical transparent nickel electrode in 1M KOH, at 303K, 101 kPa and at free ($v = 0$m/s)) and forced ($v = 0.3$m/s)) convection [28].
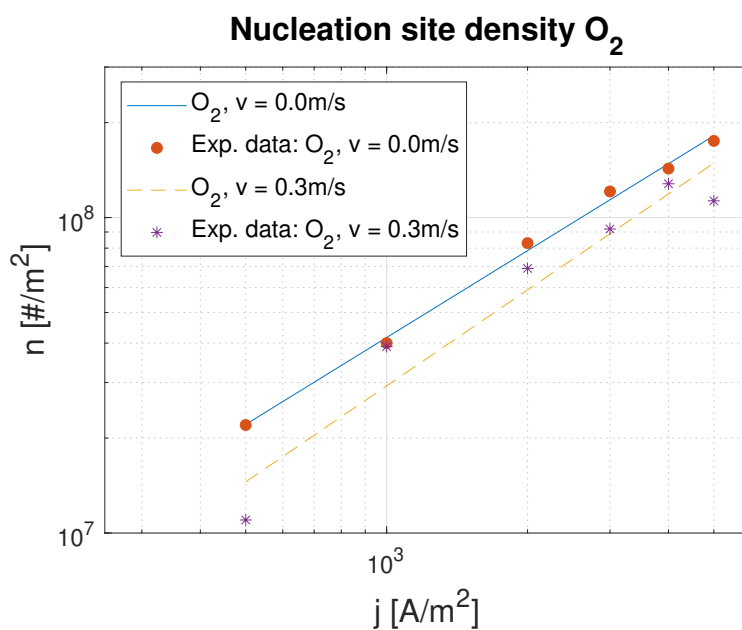
Figure 4.2: A log-log plot of the nucleation site density n against the current density j for an oxygen evolving vertical transparent nickel electrode in 1M KOH, at 303K, 101 kPa and at free ($v = 0$m/s)) and forced ($v = 0.3$m/s)) convection [28].

The power law of the nucleation site density for hydrogen is higher than for oxygen. This increase in power law is likely due to electrocapillarity; he increase in current density alters the surface potential of the working electrode, and as a result, an increase of the surface potential. The increased surface potential lowers the surface tension between the gas bubbles and the electrode surface. This effect is more significant for oxygen than for hydrogen based on the power correlation.

Also, the forced flow reduces the nucleation site density as the flow reduces the dissolved concentration near the electrode. This effect of forced flow is more dominant for lower current densities and is reduced for higher current densities, because for higher current densities sufficient dissolved gas is present to maintain nucleation.

Vogt *et al.* [87] derived an empirical relation that correlates the surface coverage to the current density for both oxygen and hydrogen from various authors:

$$\theta = 0.023 \cdot j^{0.3} \tag{4.2}$$

However, the correlation by Vogt *et al.* does not capture various effects that alter the surface coverage: gas type, flow along the electrode, and electrode surface characteristics. The correlation of Vogt *et al.* and the surface coverage experimental data of Janssen *et al.* are both plotted against the current density as illustrated in figure 4.3. As shown in figure 4.3 the correlation by Vogt *et al.* is not able
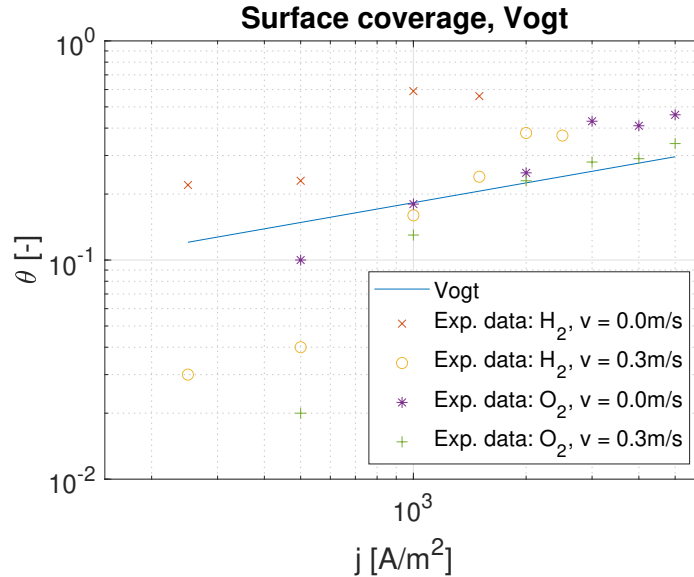
Figure 4.3: The empirical relation by Vogt *et al.* [87] and the experimental data of Janssen *et al.* [28] for surface coverage plotted against the current density.

to capture the earlier mentioned effects. The measured surface coverage by Janssen *et al.* is less for both hydrogen and oxygen over the current density range, because the flow is removes the bubbles from the electrode surface lowering the surface coverage. Also, the surface coverage for hydrogen is higher for any given current density, because twice the quantity of hydrogen product is generated. Furthermore, the electrode surface characteristics such as the surface roughness alter the likelihood of bubbles nucleating on the electrode surface. Increasing the electrode roughness increases the likelihood of bubble nucleation and therefore increases the bubble coverage. However, this last effect is not taken into account by Janssen *et al.*.

A separate surface correlation is made from the experimental data of Janssen *et al.* for both hydrogen and oxygen for the various flow velocities. The power laws for surface coverage and current density are listed below:

$$
\begin{aligned}
&\text{H}_2 : \theta = 0.0061 &&\cdot j^{0.6272} &&\&\quad v = 0.0 &&[\text{m/s}] \\
&\text{O}_2 : \theta = 0.0016 &&\cdot j^{0.6752} &&\&\quad v = 0.0 &&[\text{m/s}] \\
&\text{H}_2 : \theta = 3.0 \cdot 10^{-5} &&\cdot j^{1.2361} &&\&\quad v = 0.3 &&[\text{m/s}] \\
&\text{O}_2 : \theta = 3.0 \cdot 10^{-5} &&\cdot j^{1.121} &&\&\quad v = 0.3 &&[\text{m/s}]
\end{aligned}
\tag{4.3}
$$

Figure 4.4 and 4.5 show the fitted power curve for the surface coverage for hydrogen and oxygen, respectively. Comparing the power law by Vogt *et al.* and those from Janssen *et al.* there is a significant difference in the power number. This implies that the relation found by Vogt *et al.* for the surface coverage cannot be widely accepted.
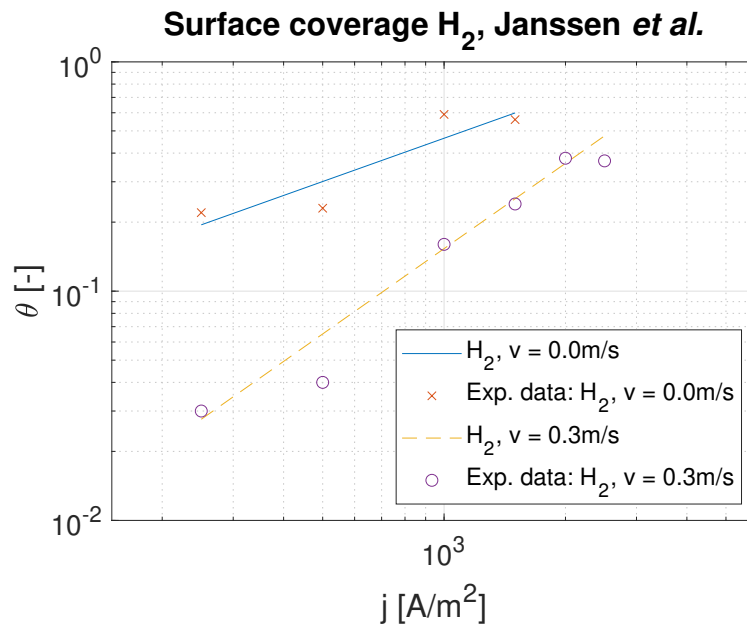
Figure 4.4: The fitted surface coverage and experimental data of hydrogen plotted against the current density for various flow velocities.
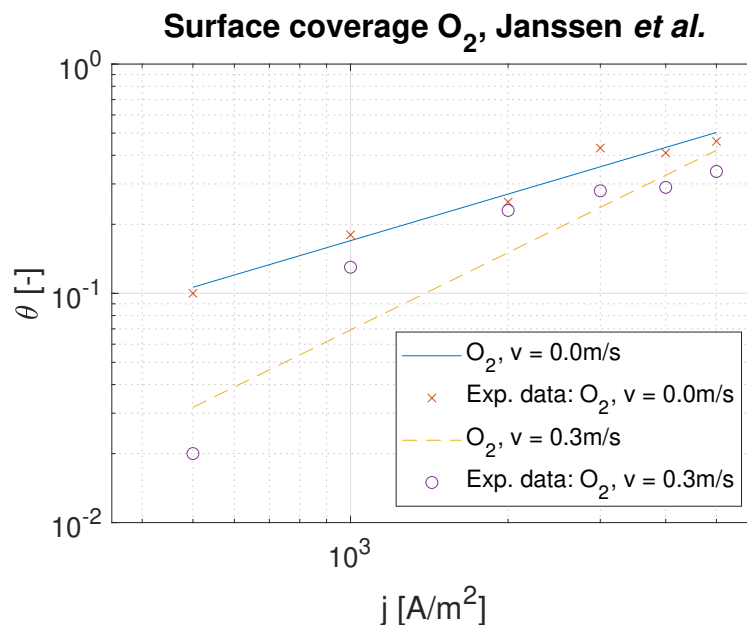
Figure 4.5: The fitted surface coverage and experimental data of oxygen plotted against the current density for various flow velocities.

Comparing the power numbers of hydrogen and oxygen in equation 4.3 the difference is less significant than comparing the power numbers for the various flow velocities. Therefore, the effect of flow velocity on the surface coverage is more dominant than the difference in gas properties.

The average bubble radius is defined based on the analytical approach illustrated in figure 2.4. The total projected area of bubbles on the electrode surface is the surface coverage and yields:

$$r_{b,i} = \sqrt{\frac{\theta_i}{n_i \pi}} \tag{4.4}$$

where $r_{b,i}$ is the bubble radius for either oxygen or hydrogen. Figure 4.6 and 4.7 show the average bubble radius experimental data and the bubble radius derived from equation 4.4 for hydrogen and oxygen, respectively. The power laws for the nucleation site density in equation 4.1 and the surface coverage in equation 4.3 are used to derive the bubble radius.
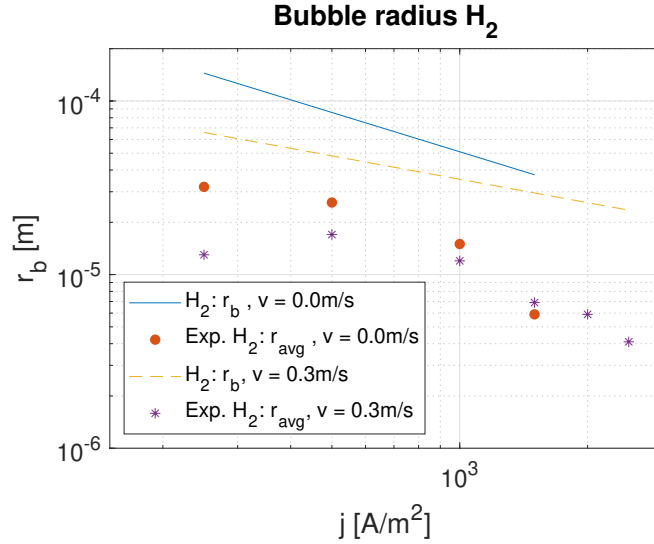
Figure 4.6: The bubble radius of hydrogen bubbles derived from equation 4.4 and the average bubble radius experimental data of Janssen *et al.* [28] for various flow velocities vs. the current density.
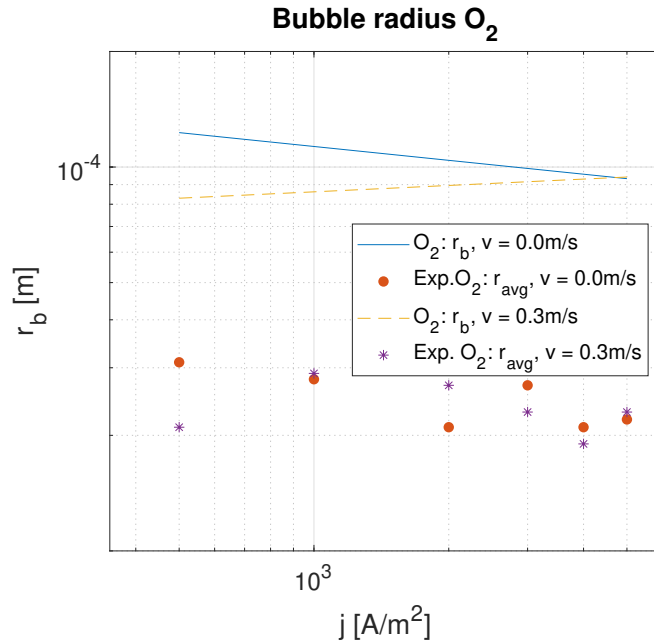
Figure 4.7: The bubble radius of oxygen bubbles derived from equation 4.4 and the average bubble radius experimental data of Janssen *et al.* [28] for various flow velocities vs. the current density.

As shown in figure 4.6 and 4.7 the average bubble radius derived from equation 4.4 are higher than the measured data by Janssen *el al.* [28]. This overestimation of the bubble radius is based on the measurement method used by Janssen *et al.* They track a fixed quantity of bubbles adhered to electrode surface by filming them while measuring the radius of those respective bubbles. However, this measurement method uses an average of all bubbles, while the bubbles just before leaving the electrode surface have a more dominant impact on the surface coverage than the smaller still growing bubbles. The bubble radius derived in equation 4.4 rather predicts the maximum average bubble radius than the average bubble radius. Figure 4.8 and 4.9 illustrate the measured maximum average radius and the analytically derived bubble radius for hydrogen and oxygen, respectively.

The derived bubble radius is in better agreement with the measured maximum average bubble radius.
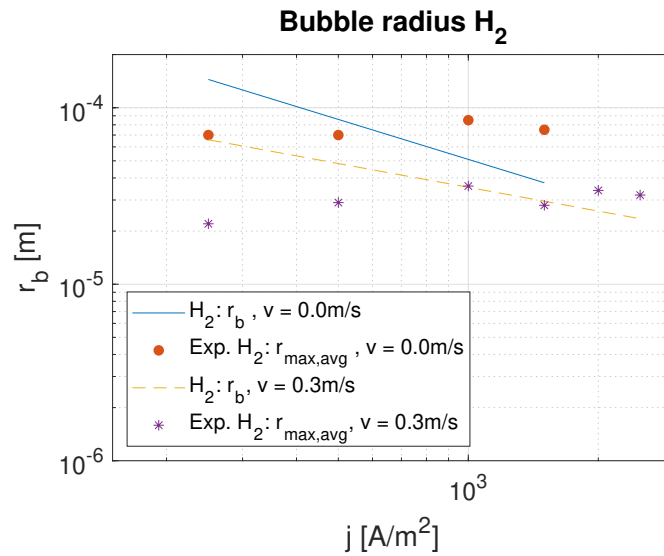
Figure 4.8: The bubble radius of hydrogen bubbles derived from equation 4.4 and the maximum average bubble radius experimental data of Janssen *et al.* [28] for various flow velocities vs. the current density.
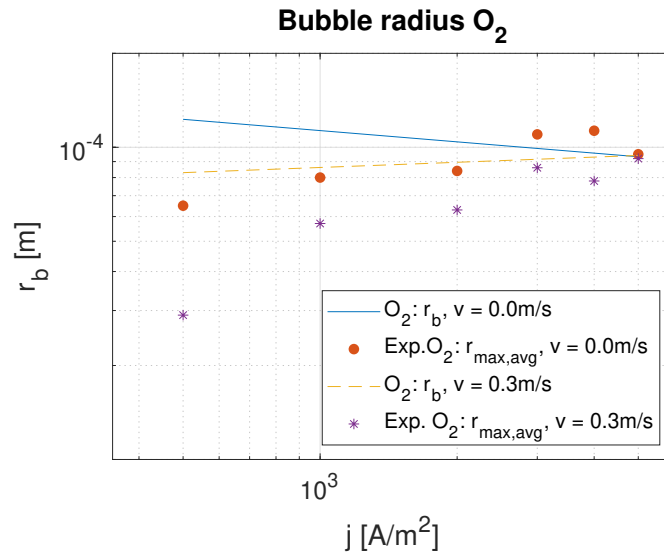
Figure 4.9: The bubble radius of oxygen bubbles derived from equation 4.4 and the maximum average bubble radius experimental data of Janssen *et al.* [28] for various flow velocities vs. the current density.

However, the trend is positive rather than negative implying that the bubbles grow instead of shrink with increased current density. In general bubbles tend to shrink with increased current densities, because the maximum bubble size is limited by the increased free convection.

The overall mass transfer coefficient is a combination of the natural convective and bubble-induced mass transfer coefficient. When forced flow is present, a superposition of the velocity is imposed on the velocity caused by the natural convection. Instead of using a Rayleigh number dependent on velocity a modified Rayleigh number is used which is derived in section 2.2 in equation 2.40. Also, the local velocity effect caused by the buoyancy of the bubbles cannot be tracked with the analytical model, rather an average velocity is used.

The modified Rayleigh number is determined based on the experimental data of Janssen *et al.* [28]. The parameters necessary for the modified Rayleigh number are listed in the table below:

It is assumed that the hydrodynamic self diffusion is of the same order as diffusion in 1M KOH water.

Parameter	Property	Value	Dimensions
g	Gravity constant	9.81	[m/s^2]
H	Height electrode	0.03	[m]
l	Inter-electrode width	0.01	[m]
V_m	Molar volume	0.0249	[m^3/mol]
ν_i	Kinematic viscosity H$_2$/O$_2$	1.09e^{-4}/1.59e^{-5}	[m^2/s]
z_i	Charge transfer H$_2$/O$_2$	2.0/4.0	[-]
$D_\mathrm{H,i}^\mathrm{eff}$	Hydrodynamic self diffusion H$_2$/O$_2$	3.0e^{-9}/1.9e^{-9}	[m^2/s]
F	Faraday constant	96485	[C/mol]

Table 4.1: Analytical properties for defining the natural, bubble-induced, and overall mass transfer coefficient

The modified Rayleigh number is plotted against the current density in figure 4.10. The difference
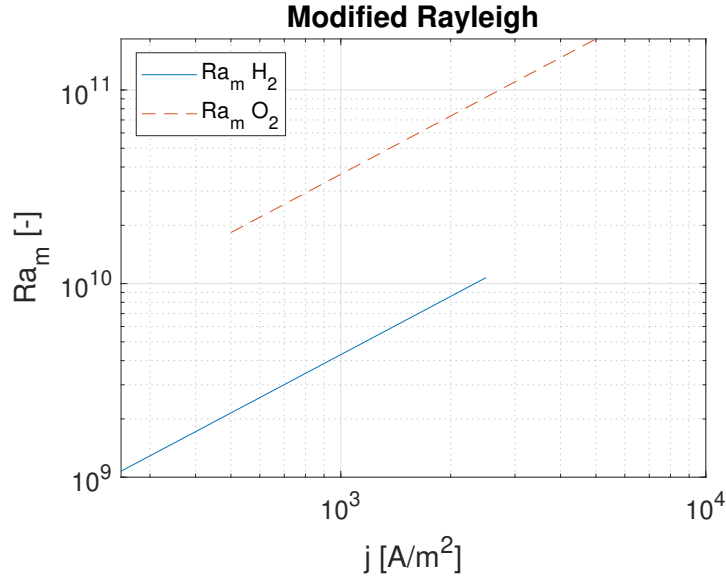
Figure 4.10: Modified Rayleigh number for hydrogen and oxygen vs. the current density based on the experimental setup of Janssen *et al.* [28].

in order of magnitude in the modified Rayleigh number between hydrogen and oxygen is a result of kinematic viscosity. Also, varying the inter-electrode width has the most influence on the Rayleigh number due to the power of the inter-electrode width which is 5.0. Smaller inter-electrode widths lowers natural convection. In contrary, lowering the electrode height increases the natural convection.

The natural convective mass transfer coefficient k_n is determined by the Sherwood number derived in equation 2.43. The relation for the natural convective mass transfer coefficient and the Sherwood number is:

$$k_n = \text{Sh}_H \frac{D_i}{H} \tag{4.5}$$

The bubble-induced mass transfer coefficient k_μ is determined by equation 2.49, and the overall mass transfer coefficient k_L with equation 2.51. The values for determining the mass transfer coefficients are listed in table 3.2.3 and 4.1.

The mass transfer coefficients illustrated in figure 4.11 are for hydrogen with a flow velocity of 0 [m/s]. As the bubble induced mixing is partially governed by the natural convective mass transfer, the bubble induced mass transfer coefficient only becomes dominant when the current density is high.
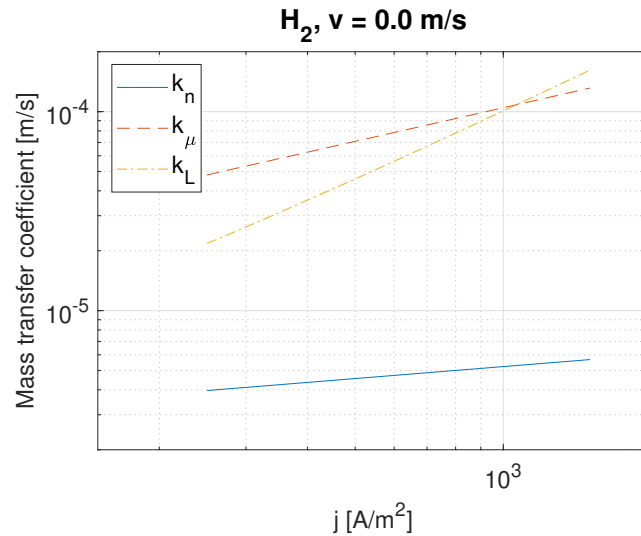
Figure 4.11: The overall, free, and bubble induced mass transfer coefficients vs. current density for hydrogen with 0 [m/s] (natural convection only) based on the experimental setup and conditions of Janssen *et al.* [28]

The mass transfer coefficient for hydrogen with a flow velocity of 0.3 [m/s] is shown in figure 4.12.
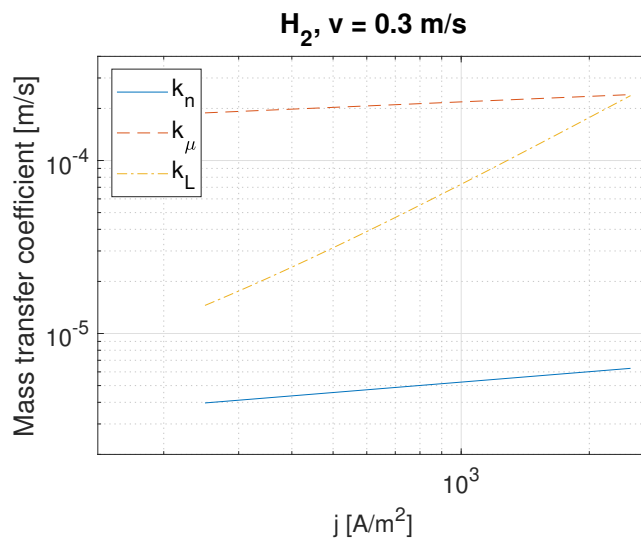
Figure 4.12: The overall, free, and bubble induced mass transfer coefficients vs. current density for hydrogen with flow velocity of $v = 3.0$ [m/s] (natural convection and forced convection) based on the experimental setup and conditions of Janssen et.al[28] .

The natural convective mass transfer for hydrogen with a flow of 0.3 [m/s] is exactly the same for the 0.0 [m/s] flow velocity, because the modified Rayleigh is dependent on the hydrodynamic self diffusion, which is assumed to be equal to the diffusion of hydrogen in 1M KOH water. The hydrodynamic self diffusion is dependent on the bubble radius and the gas fraction gradient according to equation 2.75. However, the local gas gradient can not be evaluated in an analytical model, because it is dependent on the local gas fraction. The local gas gradient depends on the vertical velocities and the local gas production. For higher velocities which is inherent to more gas production the local gas gradient increases and thus the hydrodynamic self diffusion increases. This results in an increased natural convective mass transfer for higher flow velocities.

The bubble-induced mass transfer coefficient for pure natural convection has a higher slope than for a forced flow velocity. The is a result of the hydrogen bubble radius with purely natural convection having a steeper slope than with forced convection as seen in figure 4.6. Also, the bubble nucleation site density affects the bubble induced mixing. However, the slope is similar for both flow velocities as seen in equation 4.1, and thus the effect of nucleation site density is negligible. On the other hand, the bubble induced mass transfer coefficient for a forced flow is higher over the whole current density range than for pure natural convection. This is caused by the hydrogen bubble radius being smaller for forced convection than for pure natural convection resulting in a more dominant bubble-induced mixing. Smaller bubbles generate more local-induced mixing than larger bubbles.

The overall mass transfer coefficient of hydrogen for pure and forced convection are similar in slope because the natural convection term is dominant in determining the overall mass transfer coefficient. The real effect of hydrogen on the mass transfer as stated in equation 2.51 (A_{H_2}) is only 0.21 lowering the effect of the bubble-induced mixing.

Figure 4.13 and 4.14 show the relation of the mass transfer coefficients of oxygen against the current density for a velocity of $v = 0.0$ [m/s] (pure natural convection) and $v = 0.3$ [m/s] (natural convection and forced convection), respectively.
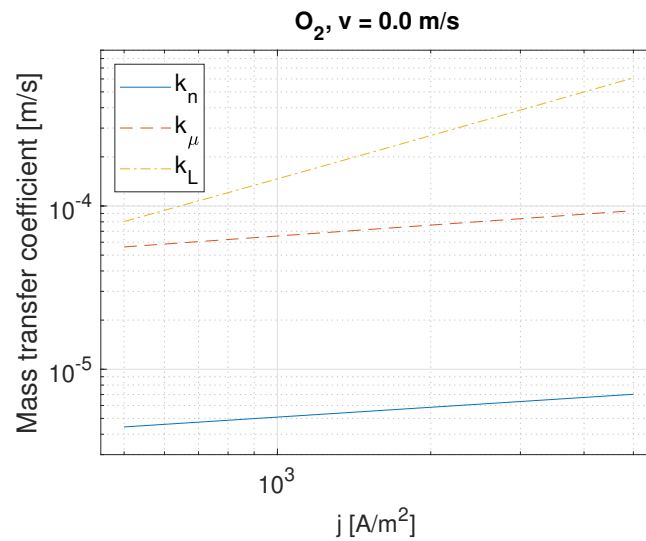
Figure 4.13: The overall, free, and bubble induced mass transfer coefficients vs. current density for hydrogen with $v = 0.0$ [m/s] based on the experimental setup and conditions of Janssen *et al.*[28].
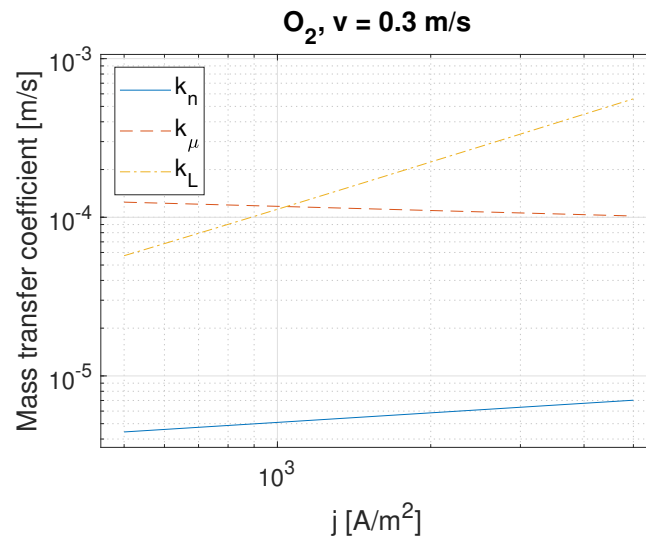
Figure 4.14: The overall, free, and bubble induced mass transfer coefficients vs. current density for oxygen with flow rate $v = 0.3$ [m/s] based on the experimental setup and conditions of Janssen *et al.*[28].

The key difference between oxygen and hydrogen is the bubble radius, the nucleation density, and the real effect oxygen has on mass transfer.

The natural convective mass transfer coefficient for oxygen for the various flow velocities as seen in figure 4.13 and 4.14 are the same. The same reasoning holds for the natural convection of hydrogen where the hydrodynamic self diffusion cannot be evaluated analytically. However, for oxygen the bubble radius is generally bigger than for hydrogen increasing the hydrodynamic self diffusion and the stokes velocity. The stokes velocity makes the mass transfer boundary layer thinner resulting in a higher local gas fraction gradient. At the other hand, the local gas fraction for oxygen is less than for hydrogen assuming no velocity effects on the gradient, because less oxygen is produced for the same given current density.

Furthermore, the intrinsic values of oxygen such as kinetic viscosity and diffusion coefficient positively affect the free natural convection.

As seen from figure 4.13, the oxygen bubble-induced mixing for pure natural convection is less for the whole current density range compared to the forced flow bubble-induced mass transfer coefficient. This is caused by the bubble radius of oxygen being overall bigger for pure natural convection as seen in figure 4.7 compared with the bubble radius of oxygen for a flow velocity of 0.3 [m/s]. However, the forced flow bubble-induced mixing has a negative slope compared to the positive slope of the pure natural convection bubble-induced mass transfer coefficient. This is a result of the increase in bubble size for higher current densities for oxygen in a forced flow configuration as seen in figure 4.7. The nucleation site density has less effect on the bubble-induced mixing than the bubble radius considering the power number used in the bubble-induced mixing. Smaller bubbles increase the bubble-induced mixing, because for a given volume multiple bubble can generate more mixing than a single bubble.

The overall mass transfer is affected by the real effect of hydrogen and oxygen ($\overline{A}_{\mathrm{H_2}}$, $\overline{A}_{\mathrm{O_2}}$) have on the natural and bubble-induced mass transfer coefficients (equation 2.51. For oxygen the real effect is larger than for hydrogen which results in a higher overall mass transfer coefficients given the same bubble size and nucleation site density.

The definition for the mass transfer boundary layer L stated in equation 2.26 and the concentration penetration depth in section 2.2 are used to define the Hatta number in equation 2.28.

Figure 4.15 shows the mass transfer boundary layer for oxygen and hydrogen at different flow velocities. The mass transfer boundary layer is larger for oxygen and hydrogen with a flow velocity of 0.3 [m/s] than for their respective 0.0 [m/s] flow velocity. It is expected that the mass transfer boundary layer should be thinner for higher flow velocity, because the flow velocity increases natural convection. However, it is not possible to evaluate the hydrodynamic self diffusion in the modified Rayleigh number analytically. Therefore, the effect of velocity on the hydrodynamic self diffusion is assumed to be constant. As a result, the natural convection mass transfer coefficient with a flow velocity bigger than 0.0 [m/s] results in a thicker mass transfer boundary layer than for a flow velocity of 0.0 [m/s]. The mass transfer boundary layer thickness is in the same order as the bubble diameter for a current density of 1000 [A/m^2] and higher. This implies that dissolved concentration can still access the bubble as long as the concentration depth reaches far enough in the mass transfer boundary layer.
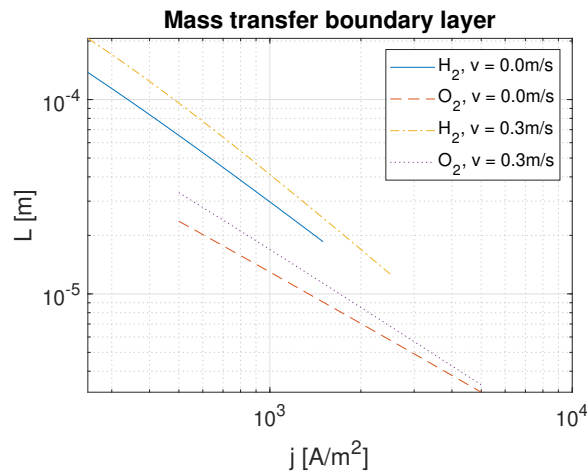
Figure 4.15: Mass transfer boundary layer L vs. current density for oxygen and hydrogen at different flow velocities.

The concentration penetration depth is visualized in figure 4.16 where the concentration depth is plotted against the current density for different flow velocities. The penetration depth is inversely proportional to the square root of the nucleation site density. This results in lower concentration depths for hydrogen than for oxygen. Again, for higher flow velocities the concentration penetration depth is bigger than for pure natural convection. This effect is a result of the flow velocity not having a influence on the hydrodynamic self diffusion which it must have.
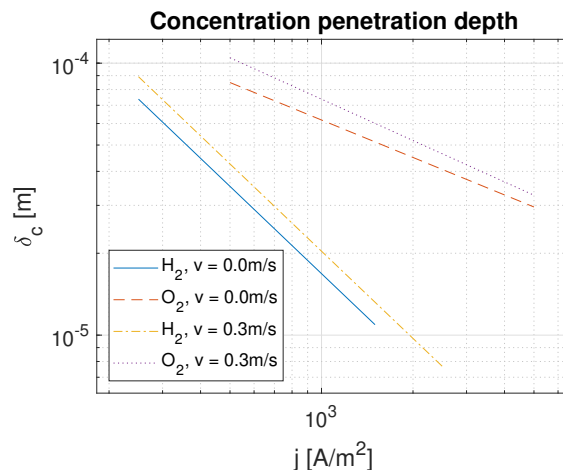
Figure 4.16: Concentration penetration depth layer δ_c vs. current density for oxygen and hydrogen at different flow velocities.

The Hatta number stated in equation 2.28 is a dimensionless number that relates the rate of dissolved gas entering the gas bubbles to the diffusion of the dissolved gas within the mass transfer boundary layer. The Hatta number for hydrogen is larger than for oxygen as shown in figure 4.17. The reason is the concentration penetration depth of hydrogen becomes significantly lower than of oxygen for a lower current densities as shown in figure 4.16. The significant decrease in concentration penetration is due to significant difference in power number for the nucleation site density as shown in equation 4.1. The shift between the curves for hydrogen is because of the flow rate which reduces the mass transfer boundary layer shown in figure 4.15. For oxygen the Hatta number does not exceed 1. The cause is the mass transfer boundary layer which is smaller for oxygen than for hydrogen. The thinner mass transfer boundary layer of oxygen is a result of the more dominant bubble induced mass transfer coefficient comparing figures 4.12 and 4.14. Also, for oxygen the concentration penetration depth is bigger than for hydrogen, because concentration penetration depth is proportional to inverse square root of the nucleation site density. And the nucleation site density for oxygen is less than for hydrogen implying that for higher current densities a larger penetration depth is reached for oxygen than for hydrogen. Moreover, hydrogen and oxygen with a flow rate have a higher overall Hatta number than without a flow rate. However, whether flow rate enhances the uptake of dissolved gas is not known. The modified Rayleigh number does not properly take into account the flow velocity effect through the hydrodynamic self diffusion. The increased Hatta number can be explained by the significantly higher nucleation site density for hydrogen compared to oxygen as seen in figure 4.1 and 4.2. A higher nucleation site density implies a bigger sink for dissolved hydrogen resulting in a higher Hatta number. Moreover, hydrogen has a smaller bubble radius than oxygen which increases the total surface area of the bubbles in within the mass transfer boundary layer to take up dissolved gas.
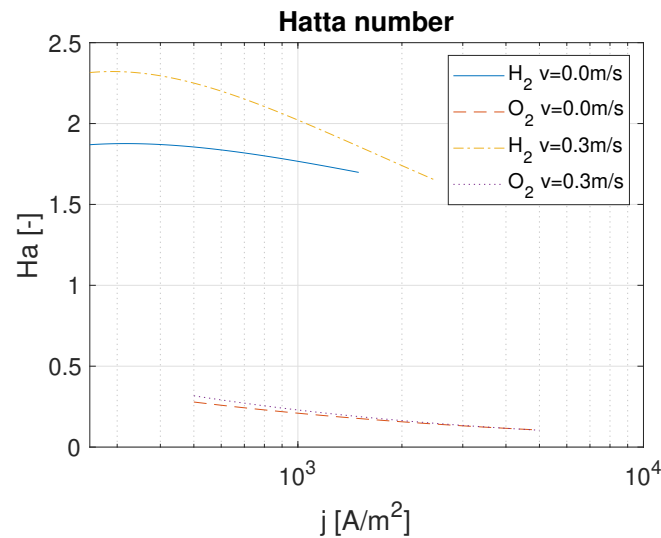
Figure 4.17: Hatta number vs. current density for oxygen and hydrogen at different flow velocities.

The gas evolution efficiency defined in section 2.2 follows the same trend as the Hatta number as shown in figure 4.18, because they are related by equation 2.32. For the hydrogen evolution the gas evolution reaches values of roughly 65 to 80 % for current densities between 250 and 2500 [A/m^2], while for oxygen this is significantly less, only up to roughly 5% between 500 and 1000 [A/m^2].
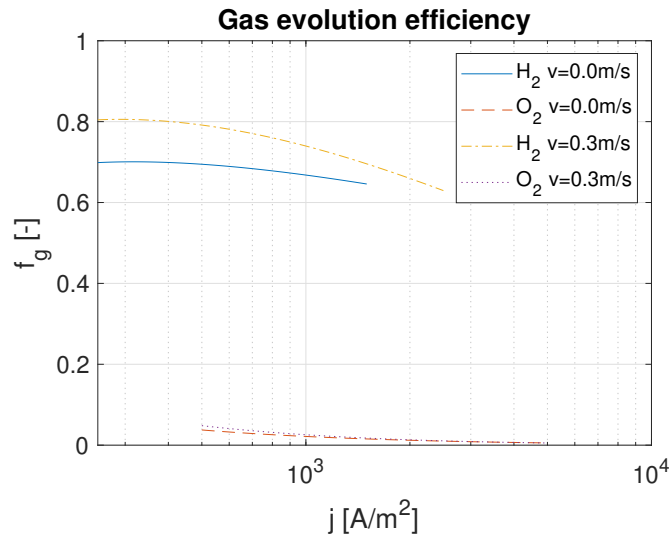
Figure 4.18: Gas-evolution efficiency f_g vs. current density for oxygen and hydrogen at different flow velocities.

Janssen et al.[38] performed measurements on the gas evolution efficiency for both oxygen and hydrogen for a similar electrode setup as used in his previous work [28]. They determined the volumetric gas evolution using high-speed films and divide the determined volumetric gas evolution by the theoretical maximum volumetric gas evolution rate ($= z_i F j V_m$). Figure 4.19 shows the hydrogen gas evolution efficiency for a flow velocity of 0.12 m/s plotted against the current density .
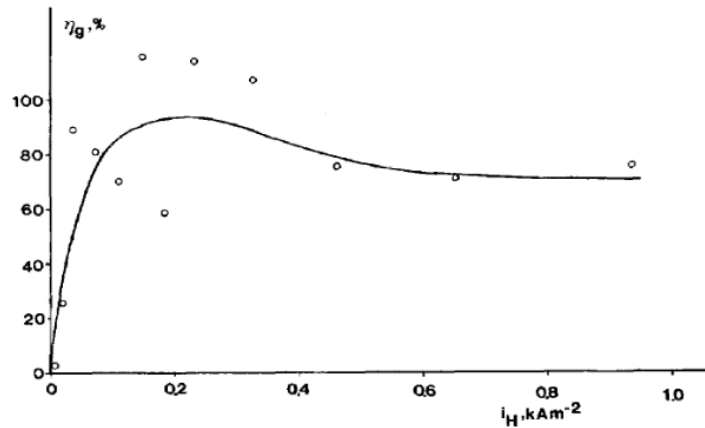
Figure 4.19: Gas evolution efficiency vs. current density for hydrogen evolution on a nickel electrode in 1M KOH at 298K and bulk solution velocity of 0.12 [m/s] [38]

The gas evolution shown in figure 4.20 by Janssen *et al.* [38] has wide range for the measured gas evolution efficiency while the analytically derived gas evolution only has a limited range of 250 to 2500 [A/m^2]. Nonetheless, the analytically derived gas evolution efficiencies shows a rather good agreement with the measured gas evolution efficiency. The scattering of the measured gas evolution efficiency is due to rather high inaccuracy, but it is mentioned that the gas evolution for hydrogen practically constant and around 75% [38]. The velocity induced by the buoyancy of the bubbles is not measured in Janssen *et al.* [38] rather the forced velocity only. Also, the gas evolution efficiency of Janssen *et al.* [38] has a peak, while the analytically derived gas evolution has not. This peak is a result of the power number used that describes the natural convection in equation 2.43. For higher power numbers

this peak increases while for lower power numbers this peak is reduced. This indicates that the free convective mass transfer coefficient is more dominant than stated by equation 2.43.
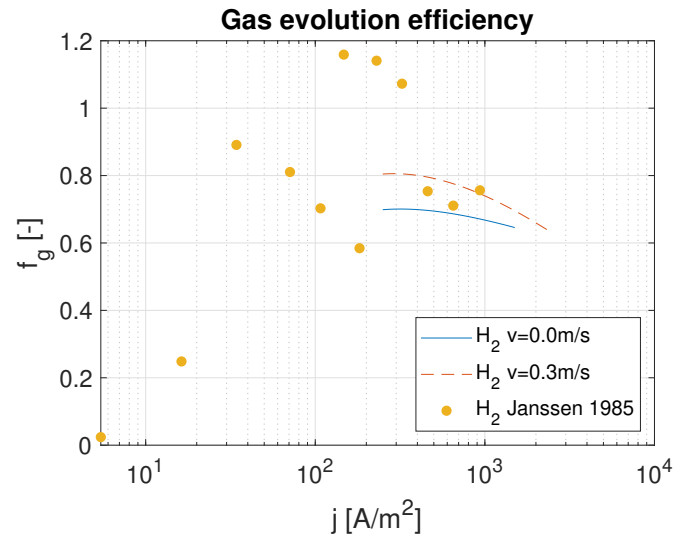
Figure 4.20: Comparison hydrogen gas evolution efficiency vs. current density for analytical derived gas evolution efficiency based on the experimental results of Janssen *et al.* [28] and measured by Janssen *et al.* 1985 [38]

The same approach is taken for comparing the oxygen gas evolution efficiency between the analytical model and the experimental data of Janssen *et al.* [38]. The overall gas evolution efficiency of oxygen for various flow velocities is roughly 65% illustrated in figure 4.21. However, the analytically derived oxygen gas evolution efficiency is significantly lower than the measured gas evolution efficiency as seen in figure 4.22. This effect is foremostly caused by the significant difference in the power number of nucleation site density stated in equation 4.1. Especially for current densities above 100 [A/m^2] the bubble nucleation site density of hydrogen increases with three orders of magnitude comparing figure 4.1 and 4.2.
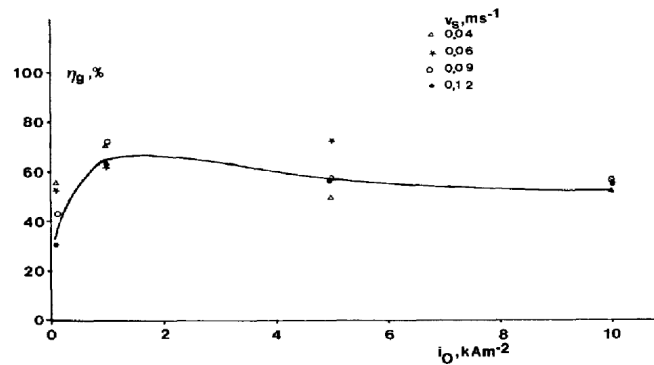
Figure 4.21: Gas evolution efficiency vs. current density for oxygen evolution on a nickel electrode in 1M KOH at 298K and various bulk velocities [38].
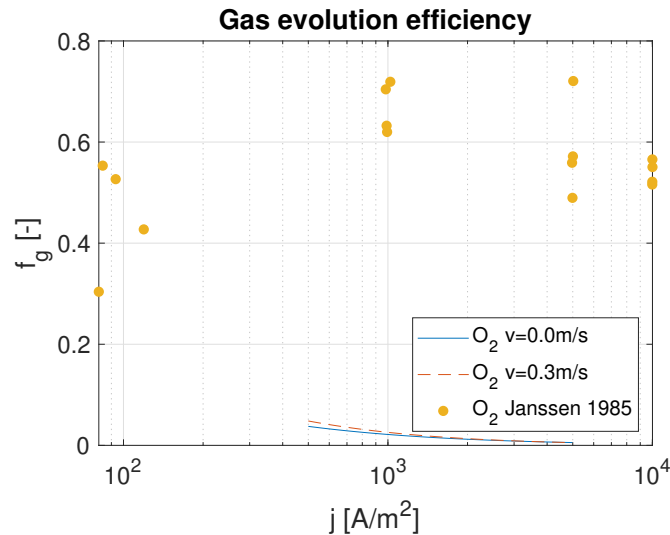
Figure 4.22: Comparison oxygen gas evolution efficiency vs. current density for analytical derived gas evolution efficiency based on the experimental results of Janssen *et al.* [28] and measured by Janssen *et al.* 1985 [38]

The predicted dissolved concentration is based on equation 2.27 and on the previous predicted mass transfer boundary layer and Hatta. The dissolved concentration is based on the experimental parameters of Janssen *et al.* [28] and is shown in figure 4.23. The dissolved concentration for hydrogen reaches
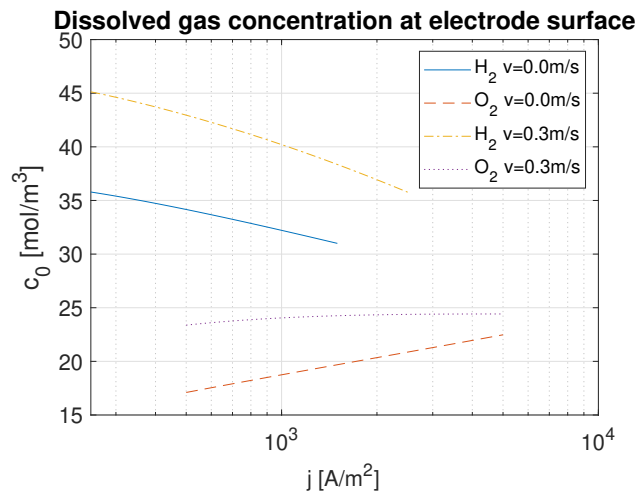
Figure 4.23: The analytically derived dissolved gas concentration plotted against the current density for hydrogen and oxygen at different flow velocities based on the experimental data of Janssen *et al.* [28].

between 30 to 40 times the maximum solubility of hydrogen in water, while for oxygen it is only 15 to 20 times the maximum solubility of oxygen in water. Based on the work of Clamroth [16] and Shibata [19, 21] who measure the dissolved gas concentration using a current-interrupt method, the trend for dissolved hydrogen concentration evolution is similar to the derived dissolved gas concentration. The trend is that at current densities between 10 and 400 [A/m^2] the dissolved gas concentration increases with current density and beyond that current density the dissolved gas concentration remains fairly constant. However, for the derived hydrogen dissolved gas concentration it is lowered with increased current density.

The dissolved gas concentration for oxygen remains constant for a wide range of current density. Glass [22] measured oxygen dissolved gas concentration which is roughly 13 times the maximum oxygen solubility, and also show an increase in dissolved current density for the same current density range for the analytically derived dissolved gas concentration. Both the measurement data of Clamroth, Glass, and Shibata can be found in Appendix C in figure C.1.

4.1.1. Effects on the dissolved gas concentration

In this section the results are discussed that affect the dissolved gas concentration to rise, and what determines its power of the current density for a wider current density than the measured data for Janssen *et al.* [28]. However, the same correlations are used as in Janssen et al. [28] and are listed below:

$$
\begin{aligned}
r_b(j) &= 73.618 \cdot j^{0.3789} \\
k_{\mathrm{L}}(j) &= 3.0 \cdot 10^{-5} \cdot j^{0.85} \\
n_{\mathrm{O_2}}(j) &= 35 \cdot 10^{6} \cdot j^{1.0} \\
\mathrm{Sh_b} &= 2
\end{aligned}
\tag{4.6}
$$

The other earlier mentioned relations for mass transfer boundary layer, concentration penetration depth, and Hatta number are the same. The three exceptions made are the power number for the nucleation site density of oxygen which is now 1.0 for simplicity. The second exceptions is that the overall mass transfer coefficient is based on the experimental data of Janssen *et al.* [31]. The last exception is that the radius r_{b} is determined based on the experimental data rather than the correlation stated in equation 4.4.

The bubble radius, mass transfer boundary layer, and the concentration penetration depth are plotted against the current density in figure 4.24. In figure 4.25 the Hatta number and enhancement factor
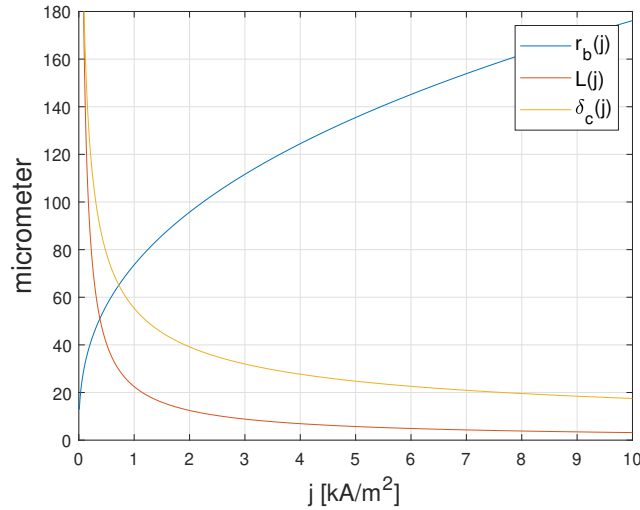
Figure 4.24: The bubble radius r_b, mass transfer boundary layer L, and the concentration penetration depth δ_c mentioned in equation 4.6 are plotted against the current density.

ε_{H} stated in equation 2.27 are plotted against the current density. As seen from figure 4.25 the Hatta number drops below 1 over a large range of current density, because δ_c is proportional to the inverse square root of the nucleation site density, and thus the current density:

$$
\delta_c \propto \frac{1}{\sqrt{n}} \propto \frac{1}{\sqrt{j}}
\tag{4.7}
$$

Also, the mass transfer boundary layer L is proportional to the current density:

$$
L \propto j^{-0.85}
\tag{4.8}
$$

where the mass transfer boundary layer becomes thinner faster with current density j.

Solving the gas evolution efficiency stated in equation 2.32 for $\frac{2r_b(j)}{L(j)} < 1$, and else for equation 2.31 for $\frac{2r_b(j)}{L(j)} \geq 1$, results in the figure 4.26. As seen in figure 4.26 the resulting Hatta number goes quickly below 1. The Hatta number can be increased by increasing the bubble Sherwood number ($\mathrm{Sh_b}$) or the bubble nucleation site density ($n(j)$). The bubble Sherwood number relates the the mass transfer by the bubble and towards the bulk. Increasing the bubble Sherwood number from $2ln(2)$ to 10 increases
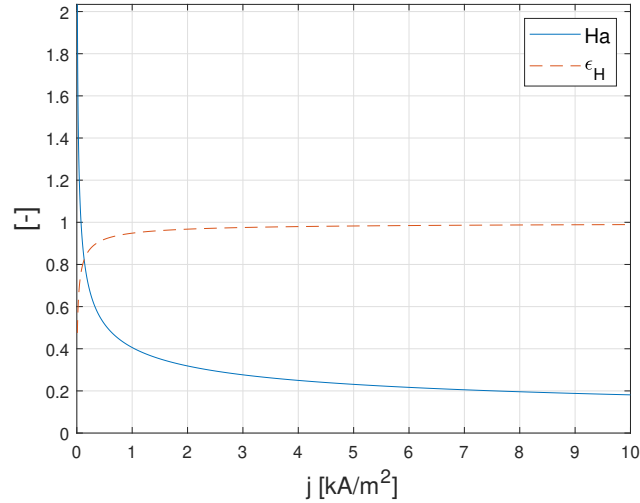
Figure 4.25: The Hatta number and enhancement factor ε_H plotted against the current density.
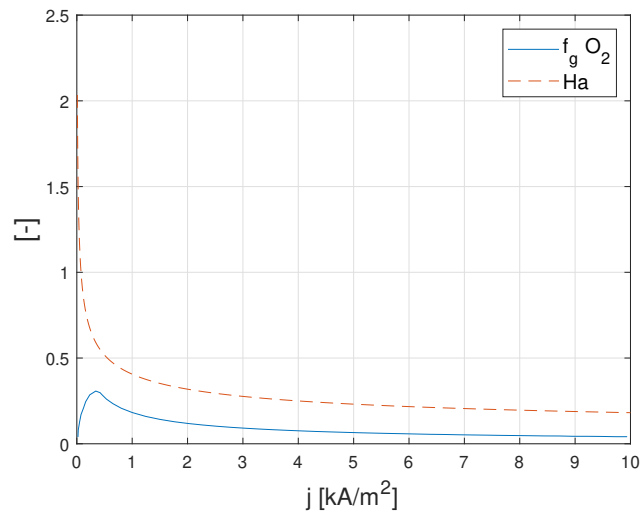
Figure 4.26: The oyxgen gas evolution efficiency and Hatta number plotted against the current density.

the as evolution effiency as seen in figure 4.27. Comparing the figures 4.21 and 4.27 the peak in the analytical approach is higher at lower current densities and the tail in the figure is decreasing more quickly than the measured oxygen gas evolution efficiency. The peak is determined by the location of $\frac{2r_b(j)}{L(j)}$. The location of the peak can shifted towards higher current densities for a thicker mass transfer boundary layer L. This increase in mass transfer boundary layer also shifts the gas evolution efficiency to higher numbers for higher current densities, because the Hatta number is increased.
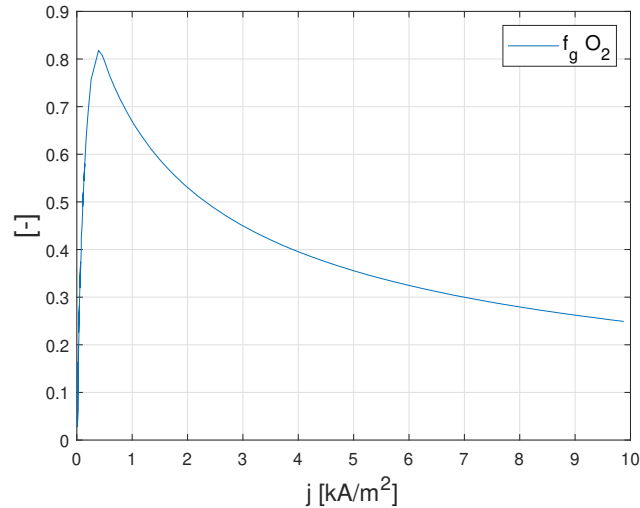
Figure 4.27: The oxygen gas evolution efficiency plotted against the current density for a bubble Sherwood number of 10.
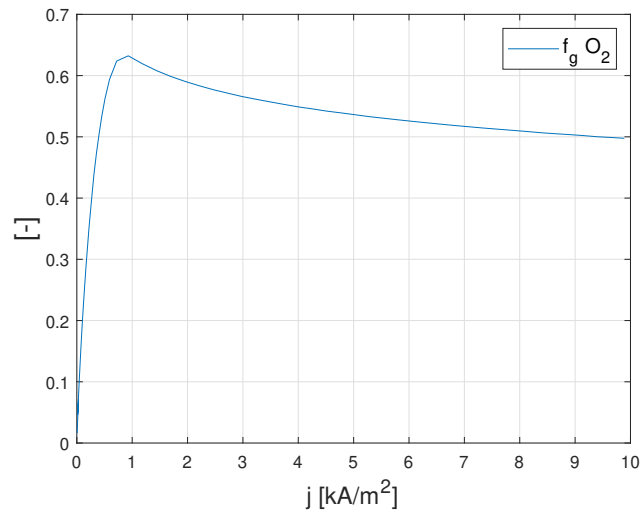
Figure 4.28: The oxygen gas evolution efficiency plotted against the current density for a three times thicker and a less current dependent mass transfer boundary layer.

Increasing the mass transfer boundary layer by three times gives a better agreement with the experimental data of Janssen *et al.* [38] as shown in figure 4.28. Also, the tail of the gas evolution efficiency can be made more flat by decreasing the power number for the mass transfer boundary layer L such that the Hatta number becomes less dependent on the current density j. Moreover, a nucleation site density which is more dependent on the current density also results in overall increase of the gas evolution efficiency. Finally, a thinner adherence region (smaller bubble radius) also shifts the peak to higher current densities. However, this must be combined by a higher bubble Sherwood number to increase the overall oxygen gas evolution efficiency.

As the dissolved gas concentration is directly coupled to gas evolution efficiency through the Hatta number, the mass transfer boundary layer, and determined by equation 2.27, the earlier mentioned effects on the gas evolution efficiency also hold for the dissolved gas concentration.

4.1.2. Literature Measurements Dissolved Gas Concentration

The database in Appendix C consists of multiple works that measure the dissolved hydrogen concentration [16, 17, 18, 19, 20, 21, 22, 23, 24, 25, 26]. From the database there is a clear distinction between vertical and horizontal electrolyzers . The trend for the power law is visualized in figure 4.29. The
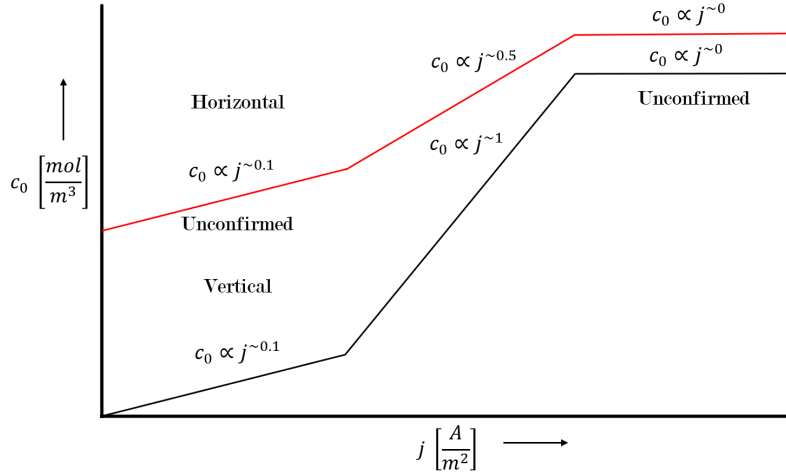
Figure 4.29: Overview of the trend lines for dissolved gas concentration in vertical and horizontal electrode setups.

dissolved concentration (c_0) follows the power law:

$$c_0 = B \cdot j^p \tag{4.9}$$

where B is a constant, j is the current density, and p is the power number. The power for horizontal lines is roughly 0.5 while for vertical setups the power is around 1.0. Moreover, the power number decreases towards zero for higher current densities. This could be an indication of homogeneous nucleation becoming dominant. Bowers *et al.* [88] state that homogeneous nucleation of oxygen bubbles occur at a concentration which is 100 times the equilibrium solubility in 30% weight percentage potassium iodide solution. It is also mentioned that agitation (stirring of the mixture) quickly lowers the dissolved gas concentration. This behaviour of dissolved gas concentration flattening for various forms agitation is seen in figure 4.30 which is the work of Shibata [21]. The dissolved gas concentration measured by Shibata is also roughly 100 times the maximum solubility of hydrogen in acidic conditions. However, in figure C.1 there are multiple cases that this flattening occurs at concentrations lower and higher than the concentration of Shibata.

Furthermore, the trend line for horizontal electrodes is above the vertical trend line, because in horizontal setups the overall dissolved concentration transfer to the bubbles is less. The reason for less mass transfer to the bubbles is that the mass transfer boundary layer is much thicker due to less natural convection compared to vertical electrodes. Hence more dissolved gas concentration can accumulate within the mass transfer boundary layer.

Two limiting cases exist for the Hatta number; the Hatta number is much smaller than 1 or bigger than 1. Both limiting cases result in a different approach of the dissolved gas concentration in equation 2.27.

Small Hatta Number

A small Hatta number states that the mass transfer boundary layer decreases less significantly with increasing current density compared to the nucleation site density as stated by equation 2.27 and equation 2.29, respectively. The mass transfer to the bulk becomes limiting, in which bubbles take away little of the dissolved gas. Therefore, the nucleation site density becomes less significant.

If the Hatta number is much smaller than 1 (Ha<< 1) the dissolved gas concentration can be approximated as:

$$c_0 = -c_0' L \tag{4.10}$$

where tanh (Ha)/Ha $\longrightarrow$ 1 in equation 2.27. This implies that the dissolved gas concentration is proportional to the current density and the mass transfer boundary layer. The dissolved gas concentration
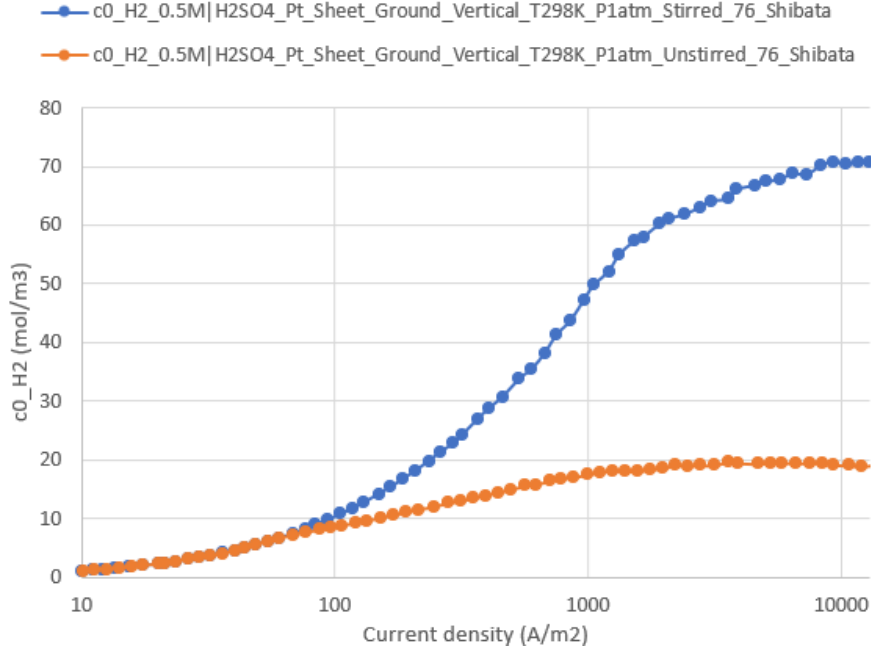
Figure 4.30: The dissolved hydrogen gas concentration vs. the current density with agitation and without agitation based on the experimental data of Shibata [21].

in equation 2.27 is now inversely proportional to the overall mass transfer coefficient:

$$c_0 \propto jL \propto \frac{j}{k_{\mathrm{L}}} \qquad (4.11)$$

where $L = \frac{D}{k_{\mathrm{L}}}$.

Large Hatta Number
For large Hatta numbers (Ha $>>$ 1) the dissolved gas concentration in equation 2.27 is approached as:

$$c_0 = -c_0' \frac{L}{\mathrm{Ha}} \qquad (4.12)$$

where the last term results in different proportionality than for a small Hatta number. The dissolved gas concentration is now approximated as:

$$c_0 \propto \frac{L}{\mathrm{Ha}} \propto \frac{j}{\sqrt{n}} \qquad (4.13)$$

where $\frac{L}{\mathrm{Ha}} = r\sqrt{\frac{Sh_a}{Sh_b \theta}} = \sqrt{\frac{Sh_a}{\pi Sh_b n}}$. For a large Hatta number a high nucleation site density and/or low overall mass transfer coefficient is required as stated in equations 2.28 and 2.27. The trend in figure 4.29 for higher current densities is only met when the dissolved gas concentration inversely follows the nucleation site density ($n \propto j^{-p}$). This can only be validated with nucleation site density, radius data or surface coverage data using equation 4.4.

4.2. Numerical Model

The results of the numerical model are divided in their respective models as mentioned in figure 2.5. The electrolyzer that will be modelled is depicted in figure 3.1. The material properties used during simulations are listed in table 3.2.3. The model implementations and conditions are explained in section 3.2.

First the electrochemical characteristics are presented and discussed. Subsequently, the flow characteristics and finally the dissolved gas concentrations are showed and evaluated.

4.2.1. Electrochemical Characteristics

As mentioned in section 2.3.5 a secondary current distribution with Butler-Volmer kinetics is used to track the electrode kinetics at the electrode-electrolyte interface. Also, in section 2.1.1 the various overpotentials are elaborated which depend on parameters that are listed in table 3.2.3 that will be used in modelling the electrochemical characteristics.

The evolution of the potential distribution over the electrolysis cell is illustrated in figure 4.31. Increasing the applied average current density increases the electrode surface potential indicated with E_{cell} in figure 4.31. This increase in electrode potential is caused by the increased activation, concentration, and ohmic overpotentials. The grey arrows indicate the path of current. In this electrolysis cell setup the anode is left and cathode is right. This implies that the ions (current) flows from the right towards the left and is experienced a negative current because of its direction in fixed frame reference. The potential
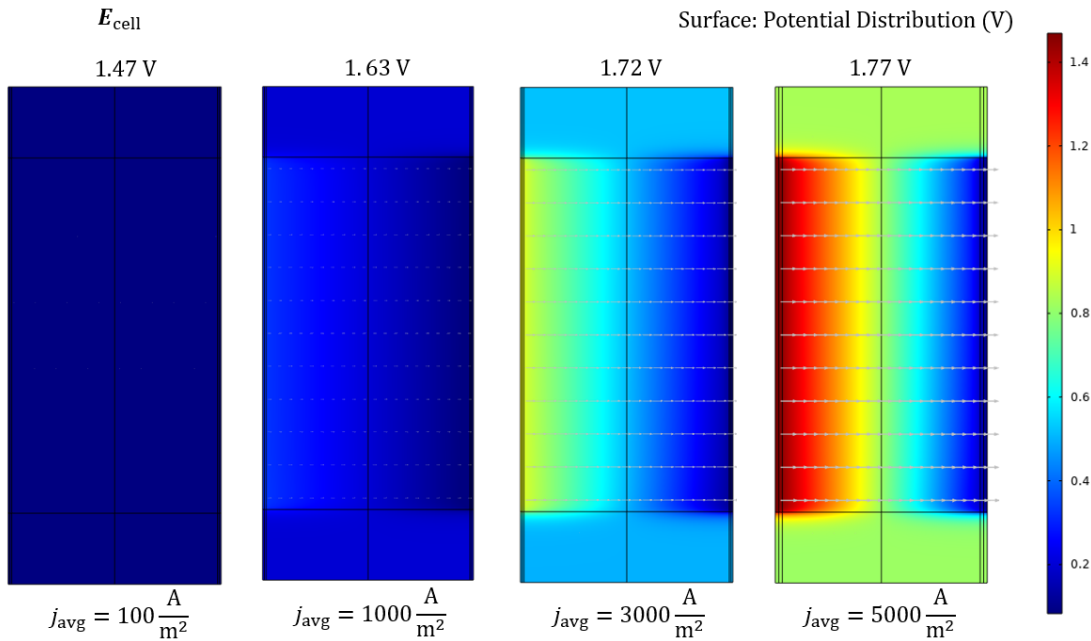
Figure 4.31: Surface contour plots of the potential distribution for different applied average current densities and the resulting electrode potential (SHE). The grey arrows are proportional to the current density and give the direction of the current.

distribution as seen in figure 4.31 is in agreement with other literature works [89].

The electrolyte conductivity is an important characteristic, because it defines the ohmic overpotential and influences the electrode potential. Subsequently, the electrode kinetics affect the activation and concentration overpotential and therefore the electrode potential. In figure 4.32 a sequence of electrolyte conductivity is presented with increasing current density. Also, the minimum electrolyte conductivity is given for each applied average current density. The steep decrease in electrolyte conductivity is related to the Bruggeman correlation stated in equation 2.8. The standard electrolyte conductivity for 1M KOH is 23 [S/m] as listed in table 3.2.3. The electrolyte conductivity decreases, because more dispersed/gas fraction is present at the electrode walls. The ions traversing the electrolyte have to travel a longer path among the gas bubbles increasing the the electrolyte resistivity. Hence a lower electrolyte conductivity at the electrode walls. Figure 4.32 also shows that the conductivity is higher for hydrogen production,
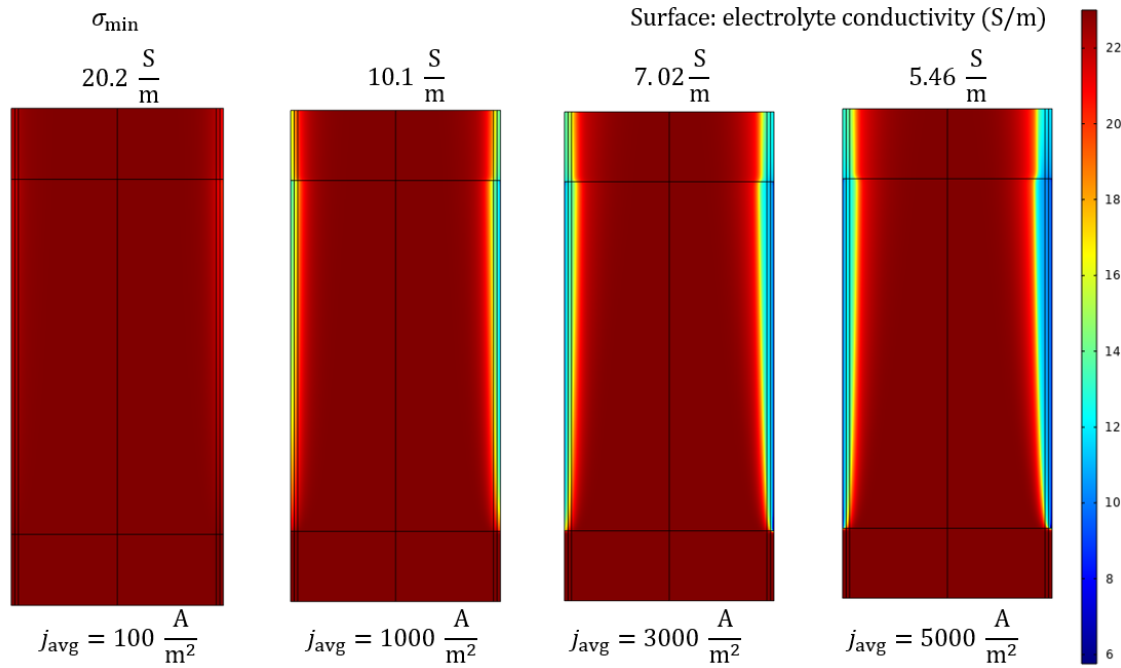
Figure 4.32: Surface contour of the electrolyte conductivity for different applied average current densities and the minimum electrolyte conductivity. The standard electrolyte conductivity in 1M KOH is 23 [S/m]

because a higher gas flux is injected at the electrode boundary. Higher applied current densities result in higher gas fractions which lower the conductivity of the electrolyte.

In the next section, flow characteristics, it is clear why the electrolyte conductivity near electrode walls are low. As mentioned, the gas fraction increases near the electrode wall lowering the electrolyte conductivity. The blue regions in figure 4.32 indirectly represent the dispersed phase.

4.2.2. Flow Characteristics

The flow characteristics are important, because it determines the distribution of the dissolved gas concentration in the electrolysis cell. In figure 4.33 the distribution of the dispersed phase is plotted for various applied average current densities. Also, the maximum gas fraction for each current density is illustrated. For increasing current densities both the gas volume fraction and the thickness of dispersed phase increases. The gas fractions have the same shape as seen in figure 4.32, because the gas fraction directly influences the electrolyte conductivity.
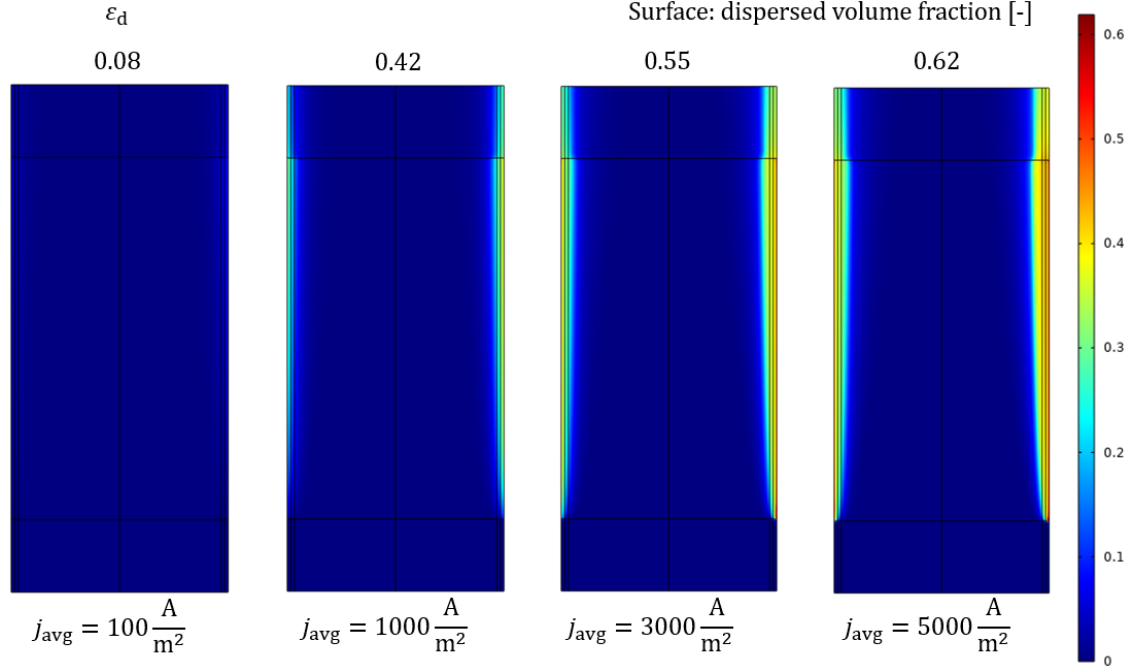
Figure 4.33: Surface contour of the dispersed volume fraction for hydrogen at the cathode (left) and oxygen at the anode (right) for different applied average current densities and the maximum dispersed fraction.

The gas volume fractions for different heights along the working electrode and an applied average current density of 5000 $[\mathrm{A/m^2}]$ are shown in figure 4.34. The middle graph in figure 4.34 shows that the hydrogen gas fraction reaches further into the bulk concentration than the oxygen gas fraction, because the hydrodynamic self diffusion stated in equation 2.75 has a larger stokes velocity and bigger gas fraction gradient. In the case for hydrogen, the bubbles are assumed to be half the radius of the oxygen bubbles. Also, but to a lesser effect is the quantity of dispersed phase entering at the electrode wall resulting in the local gas gradients. Moreover, the shear diffusion of the bubbles stated in equation 2.74 increases rapidly when the gas fraction goes towards 0.4 or higher. This results in a flatter plateau of the gas fraction as seen in the middle graph of figure 4.34. Furthermore, the porosity effect in the adherence region is shown in the left and right graph of figure 4.34. The porosity effect is stated in equation 2.80. For the HER (left) the permeability is less, because the hydrogen bubbles are smaller compared to the oxygen bubbles. Also, a higher porosity reduces the permeability, which results from the higher gas production of hydrogen. Hence the permeability in hydrogen adherence region is less.

The gas fraction in the adherence region for HER at height H = 10 mm is higher at the electrode wall than for the positions higher on the working electrode. This effect should not be present as in the adherence region the bubbles are assumed to be static and thus no stokes velocity is present. Because bubbles are able to move freely in the adherence region the gas fractions are increased. This gas fraction increase is a result of little shear-induced diffusion of the bubbles. The sudden increase in gas fraction is likely due to a transition to shear-induced diffusion which becomes dominant at higher gas fraction. The reason that oxygen with its large bubbles has higher gas fractions is likely due to its lower shear rate near the electrode wall. This results in a lower shear-induced diffusion and higher gas fractions. The shear is lower in the HER adherence region, because the permeability compared to the OER adherence region is lower.

$$j_{\mathrm{avg}} = 5000 \ \frac{\mathrm{A}}{\mathrm{m}^2}$$
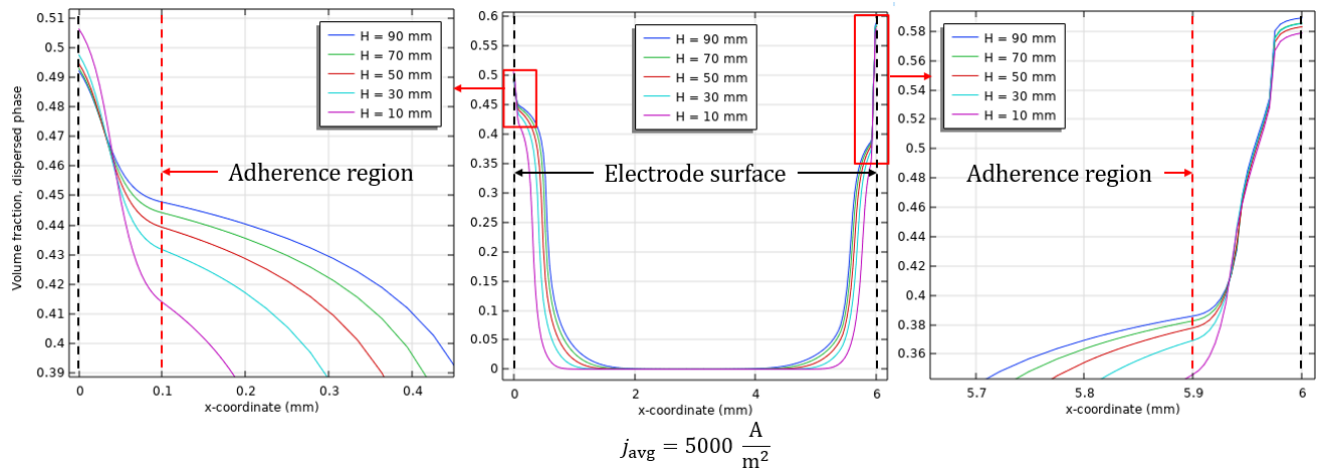
Figure 4.34: Dispersed volume fraction for hydrogen at the cathode (left) and oxygen at the anode (right) at different heights of the working electrode for an applied average current density of 5000 [A/m^2].

Figure 4.35 illustrates the gas fractions for various current densities halfway the working electrode height. As expected, the gas volume fraction increases with increasing current density. Also, increased current density results in gas penetrating deeper in the bulk (lateral direction). This is due to an increase in the lateral velocity of the gas flux.

The effect of the adherence regions on the velocity is affected by the gas fraction and not only the bubble size. The Kozeny-Carman equation 2.80 states that an decreased permeability will result from increased gas fractions. Again, for the HER this is more dominant than for OER due to the smaller bubble size of hydrogen.
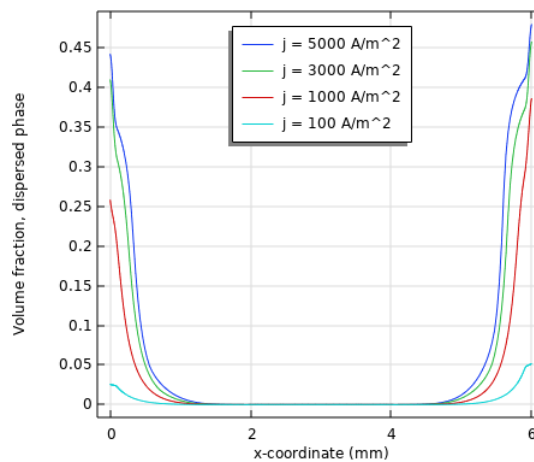
Figure 4.35: Dispersed volume fraction for oxygen at the anode (left) and hydrogen at the cathode (right) for various current densities at an height of 50 [mm].

   The bubble motion (dispersed phase) influences the electrolyte (continuous phase) by means of the gas-liquid interactions. The gas-liquid interactions are defined in terms of the slip velocities. Figure 4.36 shows the effect of the dispersed phase on the continuous phase. In the middle graph the velocity of the continuous phase is higher near the electrode walls, because more bubbles are present dragging the continuous phase with it. It is also shown, that the velocity of the continuous phase is higher for the HER (right) than for the OER (left). This is expected, because more hydrogen is generated. However, the bubble size of oxygen is larger than hydrogen which results in a higher stokes velocity. The increased velocities near the electrode surfaces reduces the velocity in the middle of the electrode as seen in the middle graph of figure 4.36. If the width between the two electrode is small enough and sufficient dispersed phase is entering the through the electrodes, the continuous velocity can be negative at the middle of the electrode.

In the left and right graph of figure 4.36 the effect of the adherence region is illustrated. For the HER (right) the porosity inhibits the flow in the adherence region. As well for the OER (left), but the permeability for hydrogen is less than for oxygen due to higher gas fractions seen in figure 4.34 and the smaller bubble size.
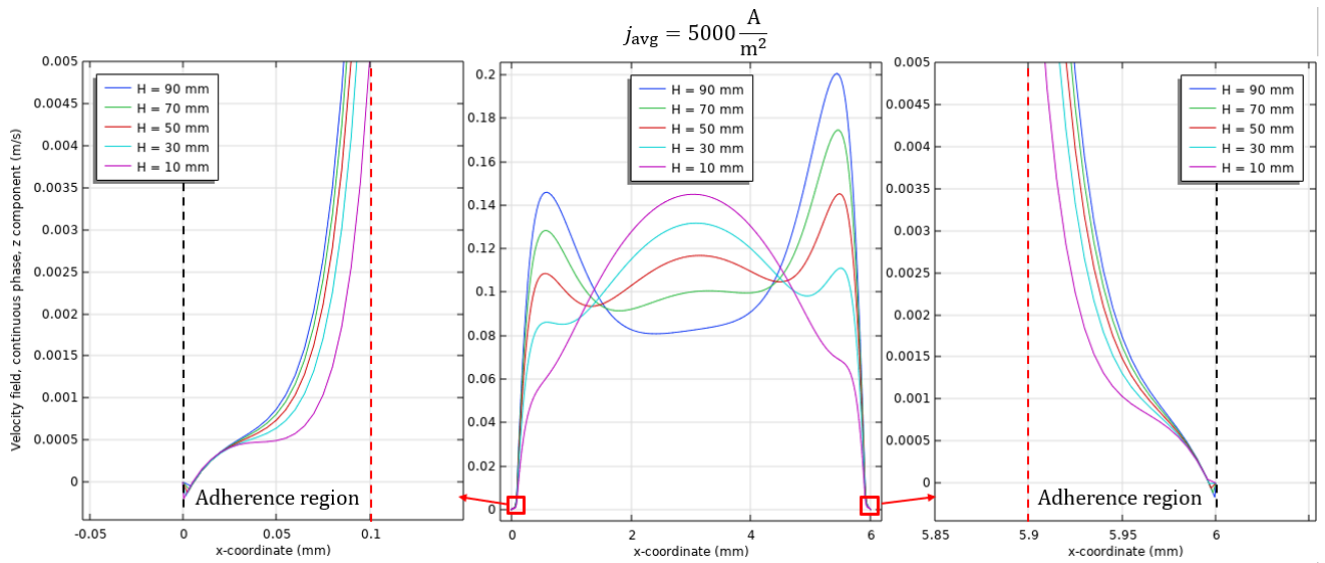
Figure 4.36: Velocity vector z-component continuous phase at different heights of the working electrode for an applied average current density of 5000 [A/m^2].

4.2.3. Chemical Species Characteristics

The flow characteristics directly influence the evolution of the tracker species and the dissolved gas concentration. First, the contour plots of the oxygen and hydrogen tracker species are showed in figure 4.37. The tracker species helps to define the mass transfer coefficient towards the electrode surface area.
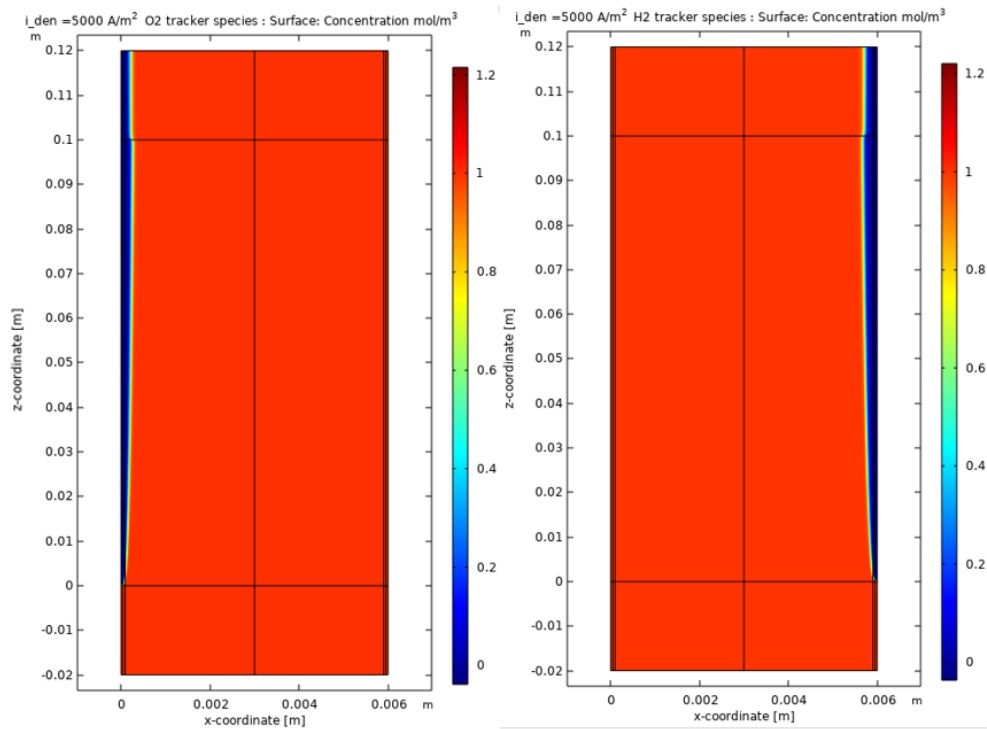
Figure 4.37: Contour plots of the oxygen(left) and hydrogen(right) tracker species for an applied current density of 5000 [A/m^2].

Both tracker species enter with a concentration of 1 [mol/m^3] and are fully consumed at their respective electrode. From figure 4.37 the distinction between the two colour regimes indicate the shift from convective to diffusive flux, because the concentration of the tracker species can only be replenished by diffusion at this boundary. The diffusion of the tracker species is not corrected for the gas fraction such that the diffusion of the tracker species could act as an effective diffusion. It is assumed that the effect of gas fraction on the diffusion of the tracker species is negligible in the adherence region, because the adherence region is only a single bubble diameter thick.

The tracker species determines the overall mass transfer coefficient k_L defined in section 2.2. The overall mass transfer coefficient is plotted in the left graph of figure 4.38.

The overall mass transfer coefficient is plotted against the electrode height position z to visualise how the mass transfer coefficient decreases with increasing height. With increasing height the local velocity increases which lowers the free natural convection and the overall mass transfer coefficient. In the right graph of figure 4.38 the mass transfer boundary layer is plotted against the working electrode height. The mass transfer boundary layer is the inverse of the overall mass transfer coefficient. Thus it becomes thicker for increasing height. This is an expected results for any given boundary layer which becomes thicker along the flow direction.
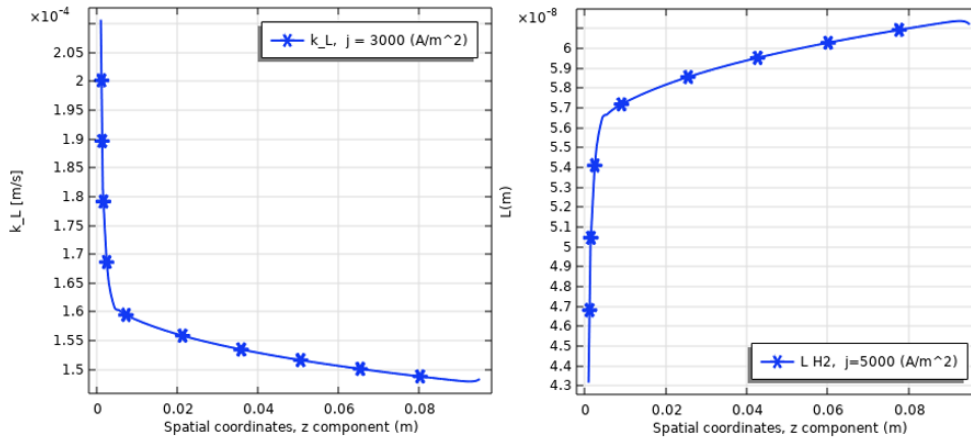
Figure 4.38: Left: The overall mass transfer coefficient (k_L) vs. the height of the working electrode with an applied current density of 5000 [A/m^2]. **Right**: The mass transfer boundary layer thickness plotted against the working electrode height with an applied current density of 5000 [A/m^2].

The mass transfer coefficient in figure 4.38 is evaluated to determine the power with respect to the height position z. The power fits of the mass transfer coefficient are plotted in figure 4.39. Comparing
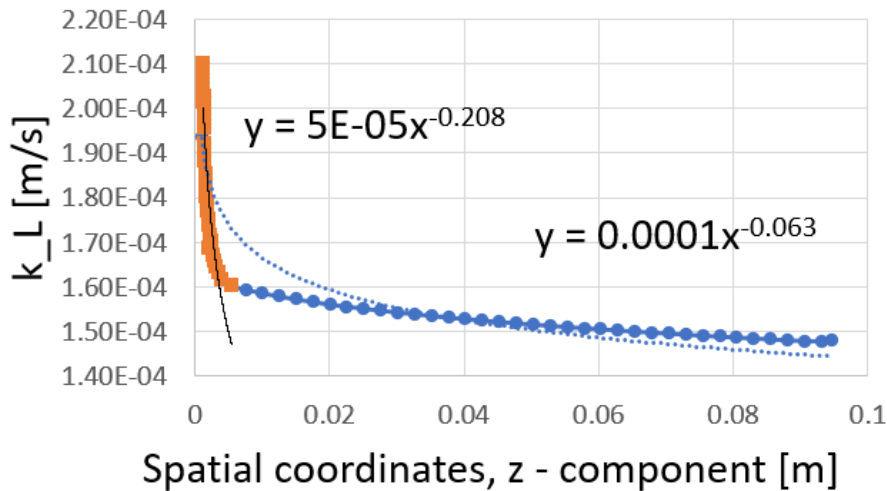
Figure 4.39: The numerical modelled mass transfer coefficient plotted against the electrode height with two separate power fits. The first fit holds for the lower part of the electrode. The second fit is for the whole electrode height.

the analytical solution for Sh_H in equation 2.43 the natural mass transfer coefficient is proportional to $z^{-0.2}$. Based on the two fits in figure 4.39 only up to an electrode height of 0.01 [m] the analytical solution holds. However, for the whole electrode height the power reduces to -0.068 which is significantly smaller than -0.2. The analytical solution for the Sherwood number could be a result of the modified Rayleigh number exceeding the boundaries for which the Sherwood number holds. As stated

in equation 2.44 the power number decreases if the modified Rayleigh number exceeds $5 \cdot 10^6$. Another possibility could be that inlet velocity boundary condition must be replaced for a pressure boundary such that the static pressure can mimic the natural convection. This only occurs for a certain inlet velocity which this model does not have, because the inlet velocity is defined at 0.1 [m/s].

Figures 4.40 and 4.41 show the evolution of the dissolved hydrogen and oxygen gas concentration, respectively. The left graphs illustrate the effect of electrode height on the dissolved gas concentrations while the right graphs show the evolution of dissolved gas concentration for various applied current densities. It shows that the dissolved gas concentration for hydrogen and oxygen is more for higher positions along the electrode. As the overall mass transfer coefficient is lower with increased electrode height, the lower dissolved gas concentrations for increased height is to be expected.

Moreover, the sink for the dissolved hydrogen gas to enter the bulk starts roughly at 8.5 micron for an
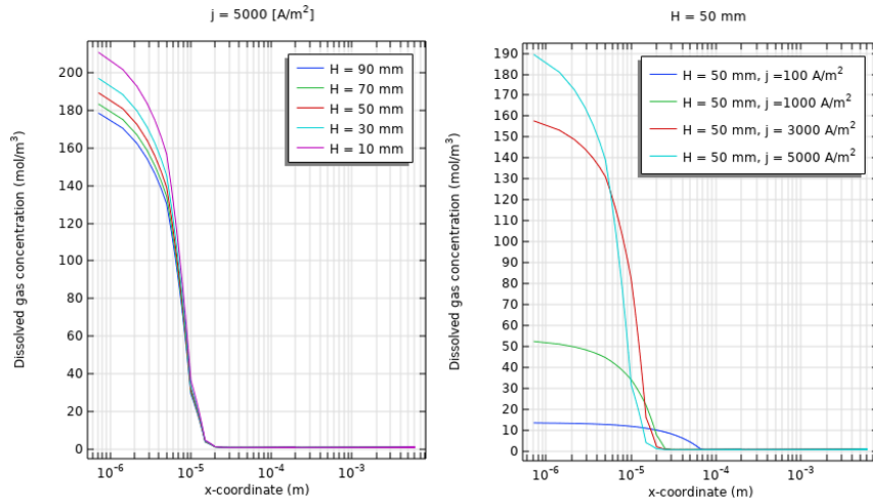
Figure 4.40: Left: Dissolved hydrogen gas concentration vs. the electrode width for various electrode heights and an applied current density of $j = +5000$ [A/m^2] . **Right**: Dissolved hydrogen gas concentration vs. electrode width for various current densities at an electrode height of 50 mm.
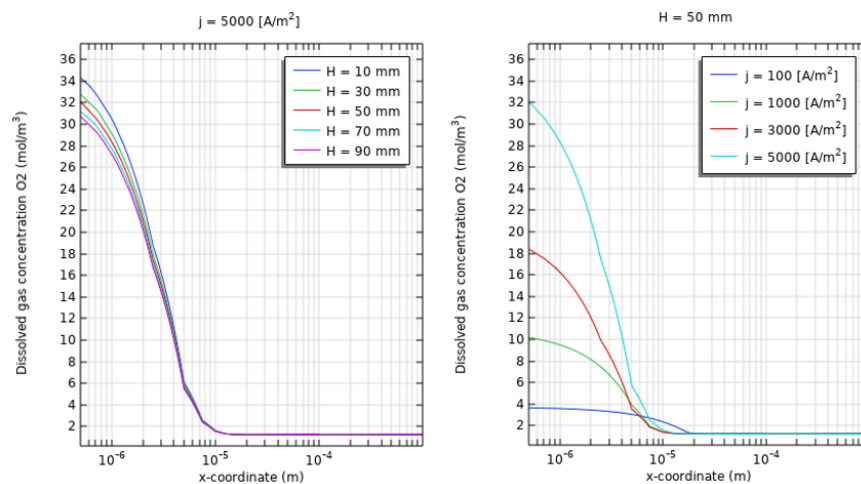
Figure 4.41: Left: Dissolved oxygen gas concentration vs. the electrode width for various electrode heights and an applied current density of $j = +5000$ [A/m^2] . **Right**: Dissolved oxygen gas concentration vs. electrode width for various current densities at an electrode height of 50 mm.

electrode height of 10 mm. This is also seen from the right graph in figures 4.38 and 4.40. The dissolved concentration quickly goes towards the maximum solubility concentration of hydrogen in water due to sink shown in figure 3.3. The value for the k_∞ sink is 500 [m/s] and is chosen such that the sink does

not overshoot. This would result in local negative dissolved gas concentrations. However, if k_∞ is too small the dissolved gas concentration will penetrate deeper into the bulk.

Furthermore, the right graphs in figure 4.40 and 4.41 show that the width of the the sink terms increases for lower current densities, because the mass transfer boundary layer becomes thicker for lower current densities.

5

Conclusion

The aim of this thesis is to understand the various effects bubble radius, nucleation site density, electrode height, and mass transfer have on the dissolved gas concentration. Grasping these various effect helps to understand how to lower the dissolved gas concentration which minimizes the activation and concentration overpotential. Eventually resulting in more efficient alkaline water electrolysis.

The analytical model uses the experimental data of Janssen *et al.* [28] to predict the gas evolution efficiency and the dissolved gas concentration. The predicted gas evolution efficiency and dissolved gas concentration was subsequently validated by another work of Janssen *et al.* [38]. The predicted hydrogen gas evolution efficiency shows a good agreement with the experimental data as seen in figure 4.20. In contrary, the predicted oxygen gas evolution efficiency is significantly less than the experimental data from Janssen *et al.* [38]. The relation stated in equation 4.4 is not able to capture the effects of surface coverage and bubble nucleation site density fully for oxygen, because the power from this relation with respect to the current density approaches zero. This implies that the bubble radius for oxygen is independent of current density, while using the experimental data of Janssen **et al.** [28] is in the order of 0.4 stated in equation 4.6. Therefore, the relation stated in equation 4.4 has a limited use. From the analytical analysis the gas evolution efficiency increases with the mass transfer of dissolved gas in to the bubble. Also, increasing the nucleation site density increases the gas evolution efficiency. Both effects are seen in figure 4.27 and figure 4.28, respectively. Moreover, shifting the peak for the gas evolution efficiency is achieved by changing the thickness of the mass transfer boundary layer stated in equation 2.26 and shown in figure 4.28. To increase the gas evolution efficiency the mass transfer boundary layer must be less dependent on current density which increases the dimensionless Hatta number. Lastly, smaller bubbles radii also shift the gas evolution peak to higher current densities. However, the dissolved mass transfer to the bubbles must be increased. Tweaking the previous effects results in a gas evolution efficiency which is in good agreement with the experimental data on the oxygen gas evolution efficiency of Janssen *et al.* [38]. The effects of mass transfer, nucleation site density, mass transfer boundary layer, and bubble radius directly affect the dissolved gas concentration in the same manner as shown by equation 2.27.

The measurements on dissolved gas concentration performed by various authors resulted in a distinct difference between vertical and horizontal electrode setups. The vertical electrodes have an increased nucleation site density rate compared to horizontal electrode for increasing current densities. For higher current density the dissolved gas concentration flattens. This effect is likely due to homogeneous nucleation and reported by Bowers *et al.* [88]. Also, horizontal electrode setups have a higher overall dissolved gas concentration than vertical electrodes, because the mass transfer boundary layer is much thicker for horizontal electrodes than for vertical electrodes.

The numerical results for the natural convective mass transfer coefficient are in agreement with the analytical expression for the natural convective Sherwood number stated in equation 2.43. However this agreement is limited to an height of 0.01 [m]. Beyond 0.01 [m] the natural convection becomes almost independent of the electrode height based on the numerical simulations. The hydrogen and oxygen dissolved gas concentrations are lowered along the height of the electrode for a fixed current

density, because the overall mass transfer coefficients increases along the height of the electrode. Also, the dissolved concentration reaches further in the bulk as the mass transfer boundary layer is broader for lower current densities, because the fluid velocity is lower.

6

Recommendations

6.1. Recommendations research and literature

- More emphasis on the bubble nucleation site density as function of current density and electrode roughness in combination with measuring the supersaturation. At this moment very literature exists that covers both nucleation site density and supersaturation within in a single experiment. Also, it best to use the current-interrupt method which is better able to measure the dissolved gas concentration at the electrode surface than using the film method.
- Investigate natural convection boundary conditions instead of using fixed inlet velocity boundaries.
- Improve slip velocities for horizontal setup
- Improve numerical instabilities for lower current densities. However, they are required to reuse the previous solution as an initial setup for higher current densities.
- The hydrodynamic self diffusion requires an analytical approach to be expressed in bubble radius and gas flux. This will improve defining natural convective mass transfer.
- The inlet velocity cannot exceed values lower than 0.01 m/s without running into convergency problems. The cause is that at least the same amount of mass must enter at the inlet and the outlet of the domain. The mass leaving the system cannot be easily tracked as the dispersed phase drags along the electrolyte. Moreover, the boundary at the top is a pressure boundary and is unable to converge when the inlet velocity is unable to overcome the hydrostatic and dynamic pressure change.
- The gas hindrance function f and shear-induced dimensionless number β_s must be improved, because the effects of shear-induced bubble diffusion is too dominant for gas fractions of 0.4 or higher.
- Extend the numerical analysis to horizontal setups and if required the slip velocities.

6.2. COMSOL recommendations

- Extend the numerical approach for the interaction between the adherence region and the bulk. Currently the adherence region is a single bubble layer, but it could be extended to multiple layers and have a non-uniform approach of the porosity.
- A non-diluted species model must be used to study the concentration near the electrode walls as the concentration for higher current densities is much higher than the potassium hydroxide concentration.
- Growth rate of the bubbles must be taken into account by the sink term defined in the diluted species model.
- Improve the computation time by using more increments for the lower current densities while reducing the time range for time dependent studies. The time dependent studies are necessary to provide proper initial conditions for the following current density in the parametric sweep.
- Improve the velocity inlet boundary conditions such that the model is able to converge for inlet velocities of 0 m/s. This can be achieved by using a pressure boundary instead of a velocity inlet boundary.

- Improve the effect the gas dispersed phase has on the diffusion of hydrogen and oxygen using relations for effective diffusivity and porosity effects.

- To improve the effect bubble radius has on flow dynamics and the sink terms, a relation for bubble size vs current density can be integrated. However, this significantly increases the computational effort as the meshing must be continuously altered in the adherence region.

- The effective diffusivity in the adherence region and outside as well can be taken into account for increased local gas fractions. However, the effects will probably be minimal in the adherence region as it is extremely thin and would not affect the mass transfer significantly.

- The meshing regime with nodes of 2.5 micrometer must be extended further into the fluid domain, because some of the accuracy is lost in determining the dissolved gas evolution near the electrode. This is seen in the left graph of figure 4.40 and figure 4.41.

- Instead of using a gas flux inlet and a dissolved gas flux inlet at the same boundary, only use a single dissolved gas flux inlet and a mass sink for the dissolved gas. This sink is then equal to the mass source for the dispersed phase. Currently an arbitrary value of 0.5 is taken for the gas evolution efficiency to prevent double the electrons transferred for the same applied current density.

References

[1] Alfredo Ursua, Luis M Gandia, and Pablo Sanchis. "Hydrogen production from water electrolysis: current status and future trends". In: *Proceedings of the IEEE* 100.2 (2011), pp. 410–426.

[2] U.S. Energy Information Administration. *EIA projects nearly 50% increase in world energy usage by 2050, led by growth in Asia*. 2019. URL: https://www.eia.gov/todayinenergy/detail.php?id=41433 (visited on 04/04/2022).

[3] European Environment Agency. *Climate change policies*. 2020. URL: https://www.eea.europa.eu/themes/climate/policy-context (visited on 04/04/2022).

[4] European Committee. *2030 climate & energy framework*. 2020. URL: https://ec.europa.eu/clima/eu-action/climate-strategies-targets/2030-climate-energy-framework_nl (visited on 04/04/2022).

[5] European Environment Agency. *Adaptation challenges and opportunities for the European energy system*. 2019. URL: https://www.eea.europa.eu/publications/adaptation-in-energy-system (visited on 04/04/2022).

[6] Sofia Elena Colesca Mihaela Pacesila Stefan Gabriel Burcea. "Analysis of renewable energies in European Union". In: *Elsevier* 56 (2016), pp. 156–170.

[7] Rebecca Lindsey and LuAnn Dahlman. "Climate change: Global temperature". In: *Climate. gov* 16 (2020).

[8] Hannah Ritchie. *How many people does synthetic fertilizer feed?* 2017. URL: https://ourworldindata.org/how-many-people-does-synthetic-fertilizer-feed (visited on 04/26/2022).

[9] Chattopadhyay Ramnarayan. *Advanced Thermally Assisted Surface Engineering Processes*. 2004.

[10] John Uri. *55 Years Ago: Apollo AS-203 Mission Tests Liquid Hydrogen Behavior*. 2021. URL: https://www.nasa.gov/feature/55-years-ago-apollo-as-203-mission-tests-liquid-hydrogen-behavior (visited on 06/01/2021).

[11] Sunita Sharma and Sib Krishna Ghoshal. "Hydrogen the future transportation fuel: From production to applications". In: *Renewable and sustainable energy reviews* 43 (2015), pp. 1151–1158.

[12] Agus Haryanto et al. "Current status of hydrogen production techniques by steam reforming of ethanol: a review". In: *Energy & Fuels* 19.5 (2005), pp. 2098–2106.

[13] Emanuele Taibi et al. "Green hydrogen cost reduction". In: (2020).

[14] Maximilian Schalenbach et al. "Acidic or alkaline? Towards a new perspective on the efficiency of water electrolysis". In: *Journal of The Electrochemical Society* 163.11 (2016), F3197.

[15] Maximilian Schalenbach et al. "A perspective on low-temperature water electrolysis-challenges in alkaline and acidic technology". In: *Int. J. Electrochem. Sci* 13.2 (2018), pp. 1173–1226.

[16] R Clamroth and CA Knorr. "Über die verschiedenen Anteile der Wasserstoffüberspannung an Palladium: I. Diffusionsüberspannung und deren Grenzwert". In: *Zeitschrift für Elektrochemie, Berichte der Bunsengesellschaft für physikalische Chemie* 57.6 (1953), pp. 399–405.

[17] M Breiter, H Kammermaier, and CA Knorr. "Untersuchung der Phasengrenzimpedanz an Edelmetallelektroden im Gebiet der Wasserstoffadsorption I. Aktivierte Platinelektroden". In: *Zeitschrift für Elektrochemie, Berichte der Bunsengesellschaft für physikalische Chemie* 60.1 (1956), pp. 37–47.

[18] Jozsef Venczel. "Ueber den Stofftransport an gasentwickelnden Elektroden". PhD thesis. ETH Zurich, 1961.

[19] Shigeo Shibata. "The concentration of molecular hydrogen on the platinum cathode". In: *Bulletin of the Chemical Society of Japan* 36.1 (1963), pp. 53–57.

[20]   Charles K Bon. "Supersaturation at gas-evolving electrodes". In: (1970).

[21]   Shigeo SHIBATA. "Supersolubility of hydyogen in acidic solution in the vicinity of hydrogen-evolving platinum cathodes in different surface states". In: *Denki Kagaku oyobi Kogyo Butsuri Kagaku* 44.11 (1976), pp. 709–712.

[22]   H Vogt. "On the supersaturation of gas in the concentration boundary layer of gas evolving electrodes". In: *Electrochimica Acta* 25.5 (1980), pp. 527–531.

[23]   RM De Jonge et al. "Gas bubble behaviour and electrolyte resistance during water electrolysis". In: *International Journal of Hydrogen Energy* 7.11 (1982), pp. 883–894.

[24]   HMS Wedershoven et al. "Behaviour of oxygen bubbles during alkaline water electrolysis". In: *International Journal of Heat and Mass Transfer* 25.8 (1982), pp. 1239–1243.

[25]   L Müller, M Krenz, and K Rübner. "On the relation between the transport of electrochemically evolved Cl2 and H2 into the electrolyte bulk by convective diffusion and by gas bubbles". In: *Electrochimica acta* 34.3 (1989), pp. 305–308.

[26]   Richard Lindsay Stover. *Bubble coalescence dynamics and supersaturation in electrolytic gas evolution*. University of California, Berkeley, 1996.

[27]   Li JJ Janssen and SJD Van Stralen. "Bubble behaviour on and mass transfer to an oxygen-evolving transparent nickel electrode in alkaline solution". In: *Electrochimica Acta* 26.8 (1981), pp. 1011–1022.

[28]   LJJ Janssen et al. "Bubble behaviour during oxygen and hydrogen evolution at transparent electrodes in KOH solution". In: *Electrochimica acta* 29.5 (1984), pp. 633–642.

[29]   K Qian, ZD Chen, and JJJ Chen. "Bubble coverage and bubble resistance using cells with horizontal electrode". In: *Journal of Applied Electrochemistry* 28.10 (1998), pp. 1141–1145.

[30]   AV Kuznetsov. "Analytical investigation of the fluid flow in the interface region between a porous medium and a clear fluid in channels partially filled with a porous medium". In: *Applied Scientific Research* 56.1 (1996), pp. 53–67.

[31]   LJJ Janssen. "Effective solution resistivity in beds containing one monolayer or multilayers of uniform spherical glass beads". In: *Journal of Applied Electrochemistry* 30.4 (2000), pp. 507–509.

[32]   H Vogt. "The role of single-phase free convection in mass transfer at gas evolving electrodes—I. Theoretical". In: *Electrochimica acta* 38.10 (1993), pp. 1421–1426.

[33]   Lokmane Abdelouahed et al. "Hydrodynamics of gas bubbles in the gap of lantern blade electrodes without forced flow of electrolyte: Experiments and CFD modelling". In: *Chemical Engineering Science* 111 (2014), pp. 255–265.

[34]   Andreas Ehrl et al. "A computational approach for the simulation of natural convection in electrochemical cells". In: *Journal of Computational Physics* 235 (2013), pp. 764–785.

[35]   Ismail M Sakr et al. "Numerical study on natural and forced convection in electrochemical cells". In: *CFD letters* 5.3 (2013), pp. 81–96.

[36]   Jonathan Schillings, Olivier Doche, and Jonathan Deseure. "Modeling of electrochemically generated bubbly flow under buoyancy-driven and forced convection". In: *International Journal of Heat and Mass Transfer* 85 (2015), pp. 292–299.

[37]   Rainier Hreiz et al. "Electrogenerated bubbles induced convection in narrow vertical cells: A review". In: *Chemical Engineering Research and Design* 100 (2015), pp. 268–281.

[38]   LJJ Janssen and E Barendrecht. "Mechanism of mass transfer of indicator ions to an oxygen-evolving and a hydrogen-evolving electrode in alkaline solution". In: *Electrochimica acta* 30.5 (1985), pp. 683–694.

[39]   H Vogt. "On the gas-evolution efficiency of electrodes I–Theoretical". In: *Electrochimica Acta* 56.3 (2011), pp. 1409–1416.

[40]   MBI Janjua and RL Le Roy. "Electrocatalyst performance in industrial water electrolysers". In: *International Journal of Hydrogen Energy* 10.1 (1985), pp. 11–19.

[41]   RL LeRoy. "Industrial water electrolysis: present and future". In: *International Journal of Hydrogen Energy* 8.6 (1983), pp. 401–417.

[42]   Christophe Coutanceau, Stève Baranton, and Thomas Audichon. *Hydrogen electrochemical production*. Academic Press, 2017.

[43]   Dohyung Jang, Hyun-Seok Cho, and Sanggyu Kang. "Numerical modeling and analysis of the effect of pressure on the performance of an alkaline water electrolysis system". In: *Applied Energy* 287 (2021), p. 116554.

[44]   Von DAG Bruggeman. "Berechnung verschiedener physikalischer Konstanten von heterogenen Substanzen. I. Dielektrizitätskonstanten und Leitfähigkeiten der Mischkörper aus isotropen Substanzen". In: *Annalen der physik* 416.7 (1935), pp. 636–664.

[45]   M Hammoudi et al. "New multi-physics approach for modelling and design of alkaline electrolyzers". In: *International Journal of Hydrogen Energy* 37.19 (2012), pp. 13895–13913.

[46]   BE Conway and L Bai. "State of adsorption and coverage by overpotential-deposited H in the H2 evolution reaction at Au and Pt". In: *Electrochimica Acta* 31.8 (1986), pp. 1013–1024.

[47]   Aria Kahyarian, Bruce Brown, and Srdjan Nesic. "Mechanism of the hydrogen evolution reaction in mildly acidic environments on gold". In: *Journal of The Electrochemical Society* 164.6 (2017), H365.

[48]   GJ Brug et al. "The kinetics of the reduction of protons at polycrystalline and monocrystalline gold electrodes". In: *Journal of electroanalytical chemistry and interfacial electrochemistry* 181.1-2 (1984), pp. 245–266.

[49]   Livia Giordano et al. "pH dependence of OER activity of oxides: current and future perspectives". In: *Catalysis Today* 262 (2016), pp. 2–10.

[50]   R.+ Kötz, H Neff, and S Stucki. "Anodic Iridium Oxide Films: XPS-Studies of Oxidation State Changes and". In: *Journal of The Electrochemical Society* 131.1 (1984), p. 72.

[51]   Miao Zhang, Moreno De Respinis, and Heinz Frei. "Time-resolved observations of water oxidation intermediates on a cobalt oxide nanoparticle catalyst". In: *Nature chemistry* 6.4 (2014), pp. 362–367.

[52]   Kai S Exner and Herbert Over. "Beyond the rate-determining step in the oxygen evolution reaction over a single-crystalline IrO2 (110) model electrode: kinetic scaling relations". In: *ACS Catalysis* 9.8 (2019), pp. 6755–6765.

[53]   James B Gerken et al. "A survey of diverse earth abundant oxygen evolution electrocatalysts showing enhanced activity from Ni–Fe oxides containing a third metal". In: *Energy & Environmental Science* 7.7 (2014), pp. 2376–2382.

[54]   Isabela C Man et al. "Universality in oxygen evolution electrocatalysis on oxide surfaces". In: *ChemCatChem* 3.7 (2011), pp. 1159–1165.

[55]   Nemanja Danilovic et al. "Activity–stability trends for the oxygen evolution reaction on monometallic oxides in acidic environments". In: *The journal of physical chemistry letters* 5.14 (2014), pp. 2474–2478.

[56]   Serhiy Cherevko et al. "Dissolution of noble metals during oxygen evolution in acidic media". In: *ChemCatChem* 6.8 (2014), pp. 2219–2223.

[57]   K Stephan and H Vogt. "A model for correlating mass transfer data at gas evolving electrodes". In: *Electrochimica Acta* 24.1 (1979), pp. 11–18.

[58]   J.W.Haverkort. "Mathematical Model Alkaline Water Electrolysis". To be distributed as future work. Apr. 2022.

[59]   JW Haverkort and H Rajaei. "Voltage losses in zero-gap alkaline water electrolysis". In: *Journal of Power Sources* 497 (2021), p. 229864.

[60]   Boris Brangeon, Patrice Joubert, and Alain Bastide. "Influence of the dynamic boundary conditions on natural convection in an asymmetrically heated channel". In: *International Journal of Thermal Sciences* 95 (2015), pp. 64–72.

[61]   Frédéric Dupont et al. "Etude expérimentale de la convection naturelle en canal vertical chauffé à flux constant: Influence de l'angle d'inclinaison". In: *Congrés Francais de Thermique* (2007), p. 6.

[62] BW Webb and DP Hill. "High Rayleigh number laminar natural convection in an asymmetrically heated vertical channel". In: (1989).

[63] COMSOL. URL: https://www.comsol.com/ (visited on 04/15/2022).

[64] D Darmana, NG Deen, and JAM Kuipers. "Detailed modeling of hydrodynamics, mass transfer and chemical reactions in a bubble column using a discrete bubble model". In: *Chemical engineering science* 60.12 (2005), pp. 3383–3404.

[65] Alexande Sokolichin, Gerhart Eigenberger, and Alexej Lapin. "Simulation of buoyancy driven bubbly flow: established simplifications and open questions". In: *AIChE Journal* 50.1 (2004), pp. 24–45.

[66] MS Nigam. "Numerical simulation of buoyant mixture flows". In: *International journal of multiphase flow* 29.6 (2003), pp. 983–1015.

[67] Ruben Wedin and Anders A Dahlkild. "On the transport of small bubbles under developing channel flow in a buoyant gas-evolving electrochemical cell". In: *Industrial & engineering chemistry research* 40.23 (2001), pp. 5228–5233.

[68] COMSOL. *The CFD Module User's Guide*. URL: https://doc.comsol.com/5.3/doc/com.comsol.help.cfd/CFDModuleUsersGuide.pdf (visited on 04/16/2022).

[69] Anders A Dahlkild. "Modelling the two-phase flow and current distribution along a vertical gas-evolving electrode". In: *Journal of Fluid Mechanics* 428 (2001), pp. 249–272.

[70] H Nicolai et al. "Particle velocity fluctuations and hydrodynamic self-diffusion of sedimenting non-Brownian spheres". In: *Physics of Fluids* 7.1 (1995), pp. 12–23.

[71] David Leighton and Andreas Acrivos. "Measurement of shear-induced self-diffusion in concentrated suspensions of spheres". In: *Journal of Fluid Mechanics* 177 (1987), pp. 109–131.

[72] Uwe Schaflinger. "Centrifugal separation of a mixture". In: *Fluid Dynamics Research* 6.5-6 (1990), p. 213.

[73] Philip Geoffrey Saffman. "The lift on a small sphere in a slow shear flow". In: *Journal of fluid mechanics* 22.2 (1965), pp. 385–400.

[74] COMSOL. *The Porous Media Flow Module User's Guide*. URL: https://doc.comsol.com/5.6/doc/com.comsol.help.porous/PorousMediaFlowModuleUsersGuide.pdf (visited on 04/18/2022).

[75] J Alberto Ochoa-Tapia and Stephen Whitaker. "Momentum transfer at the boundary between a porous medium and a homogeneous fluid—I. Theoretical development". In: *International Journal of Heat and Mass Transfer* 38.14 (1995), pp. 2635–2646.

[76] J Alberto Ochoa-Tapia and Stephen Whitaker. "Momentum transfer at the boundary between a porous medium and a homogeneous fluid—II. Comparison with experiment". In: *International Journal of Heat and Mass Transfer* 38.14 (1995), pp. 2647–2655.

[77] COMSOL. *The COMSOL Reference Manual*. URL: https://doc.comsol.com/5.5/doc/com.comsol.help.comsol/COMSOL_ReferenceManual.pdf (visited on 04/18/2022).

[78] Edmund JF Dickinson, Juan G Limon-Petersen, and Richard G Compton. "The electroneutrality approximation in electrochemistry". In: *Journal of Solid State Electrochemistry* 15.7 (2011), pp. 1335–1345.

[79] Engineering Toolbox. *Hydrogen- Density and Specific Weight vs. Temperature and Pressure*. URL: https://www.engineeringtoolbox.com/hydrogen-H2-density-specific-weight-temperature-pressure-d_2%20044.html (visited on 04/21/2022).

[80] Engineering Toolbox. *Oxygen - Density and Specific Weight vs. Temperature and Pressure*. URL: https://www.engineeringtoolbox.com/oxygen-O2-density-specific-weight-temperature-pressure-d_2082.html (visited on 04/21/2022).

[81] Pal M Sipos, Glenn Hefter, and Peter M May. "Viscosities and densities of highly concentrated aqueous MOH solutions (M+= Na+, K+, Li+, Cs+,(CH3) 4N+) at 25.0° C". In: *Journal of Chemical & Engineering Data* 45.4 (2000), pp. 613–617.

[82]   Engineering Toolbox. *Dynamic Viscosities of Common Gasses*. URL: `https://www.engineering toolbox.com/gases-absolute-dynamic-viscosity-d_1888.html` (visited on 04/21/2022).

[83]   RJ Gilliam et al. "A review of specific conductivities of potassium hydroxide solutions for various concentrations and temperatures". In: *International Journal of Hydrogen Energy* 32.3 (2007), pp. 359–364.

[84]   Engineering Toolbox. *Solubility of Gases in Water vs. Temperature*. URL: `https://www.enginee ringtoolbox.com/gases-solubility-water-d_1148.html` (visited on 04/21/2022).

[85]   RE Davis, GL Horvath, and CW Tobias. "The solubility and diffusion coefficient of oxygen in potassium hydroxide solutions". In: *Electrochimica Acta* 12.3 (1967), pp. 287–297.

[86]   Min J Tham, Robert Dixon Walker Jr, and Keith E Gubbins. "Diffusion of oxygen and hydrogen in aqueous potassium hydroxide solutions". In: *The Journal of Physical Chemistry* 74.8 (1970), pp. 1747–1751.

[87]   H Vogt and RJ Balzer. "The bubble coverage of gas-evolving electrodes in stagnant electrolytes". In: *Electrochimica acta* 50.10 (2005), pp. 2073–2079.

[88]   Peter G Bowers et al. "Supersaturation limit for homogeneous nucleation of oxygen bubbles in water at elevated pressure:" Super-Henry's Law"". In: *The Journal of Physical Chemistry* 99.23 (1995), pp. 9632–9637.

[89]   E Amores Vera et al. "Study of an alkaline electrolyzer powered by renewable energy". In: *Excerpt from the Proceedings of the 2011 COMSOL Conference in (Stuttgart)*. 2011.

[90]   Stuart W Churchill and Humbert HS Chu. "Correlating equations for laminar and turbulent free convection from a vertical plate". In: *International journal of heat and mass transfer* 18.11 (1975), pp. 1323–1329.

A
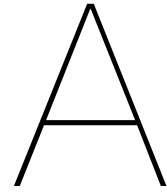
Appendix A

The conductivity of electrolyte containing potassium hydroxide for various temperatures plotted against the molarity as illustrated in figure A.1.
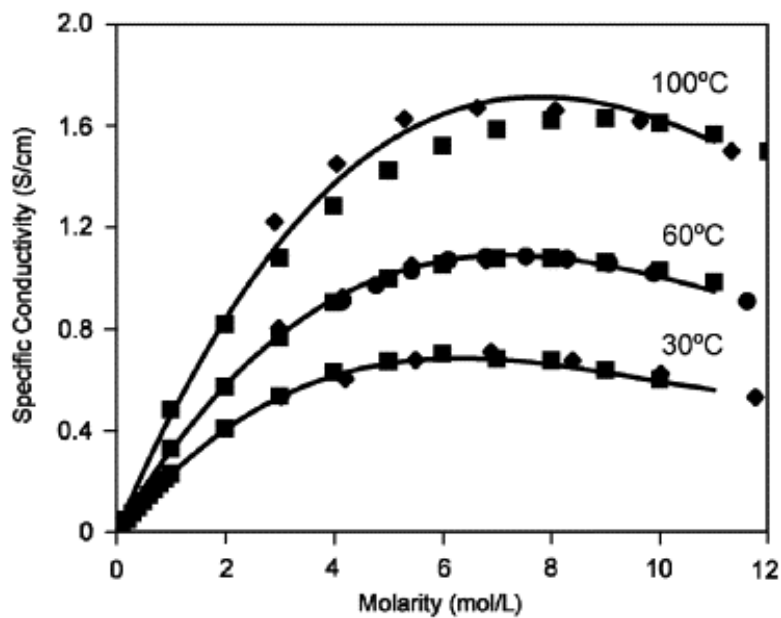
Figure A.1: Conductivity of the electrolyte containing potassium hydroxide (KOH) vs. molarity at 30, 60, and 100 °C. Reprinted from Gilliam et al.[83].

The semi-empirical relations derived by Churchill et al. and the tabular data of Ede for the laminar regime of isothermal, vertical plates [90].
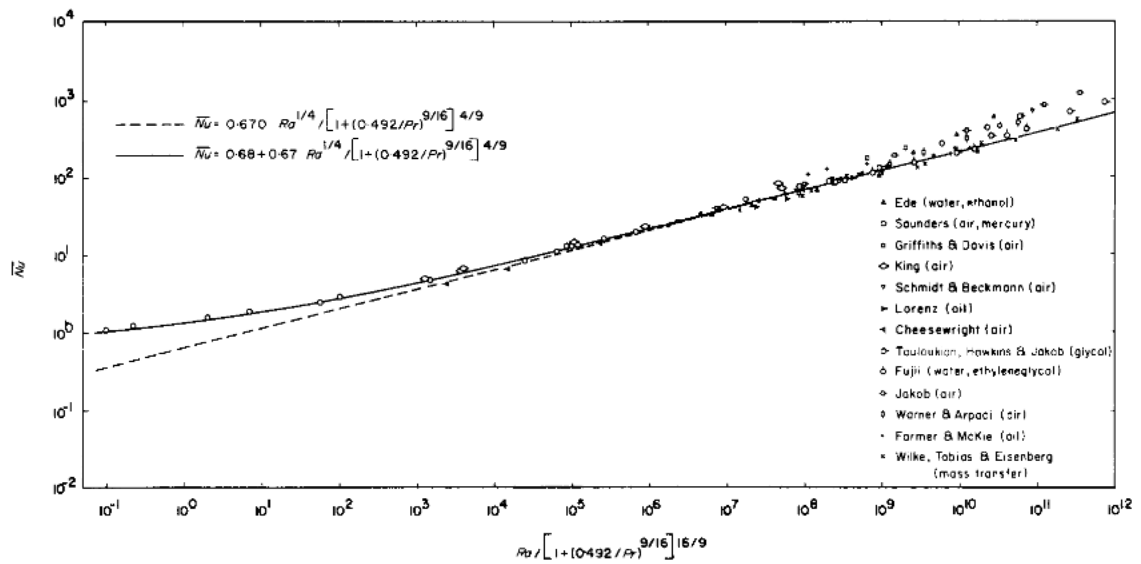
Figure A.2: The semi-empirical relations derived by Churchill et al. and the tabular data of Ede for the laminar regime of isothermal, vertical plates [90].

B

Appendix B
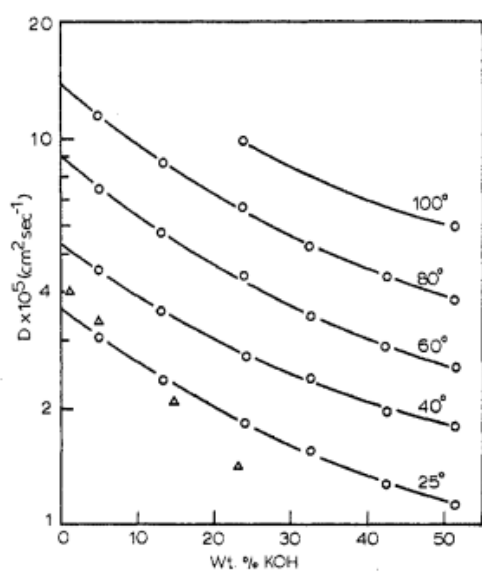
Figure B.1: Diffusion coefficients for hydrogen in KOH solutions at various temperatures [86].
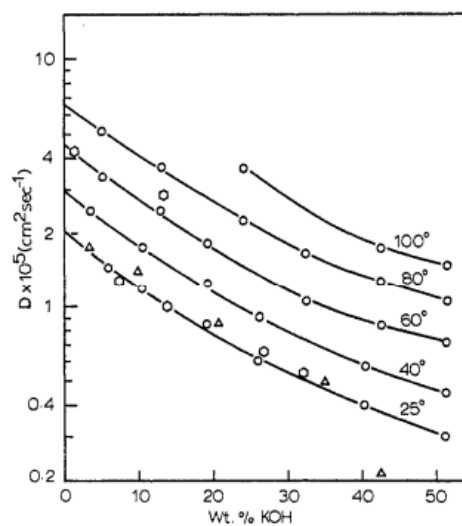
Figure B.2: Diffusion coefficients for oxygen in KOH solutions at various temperatures [86].

C

Appendix C
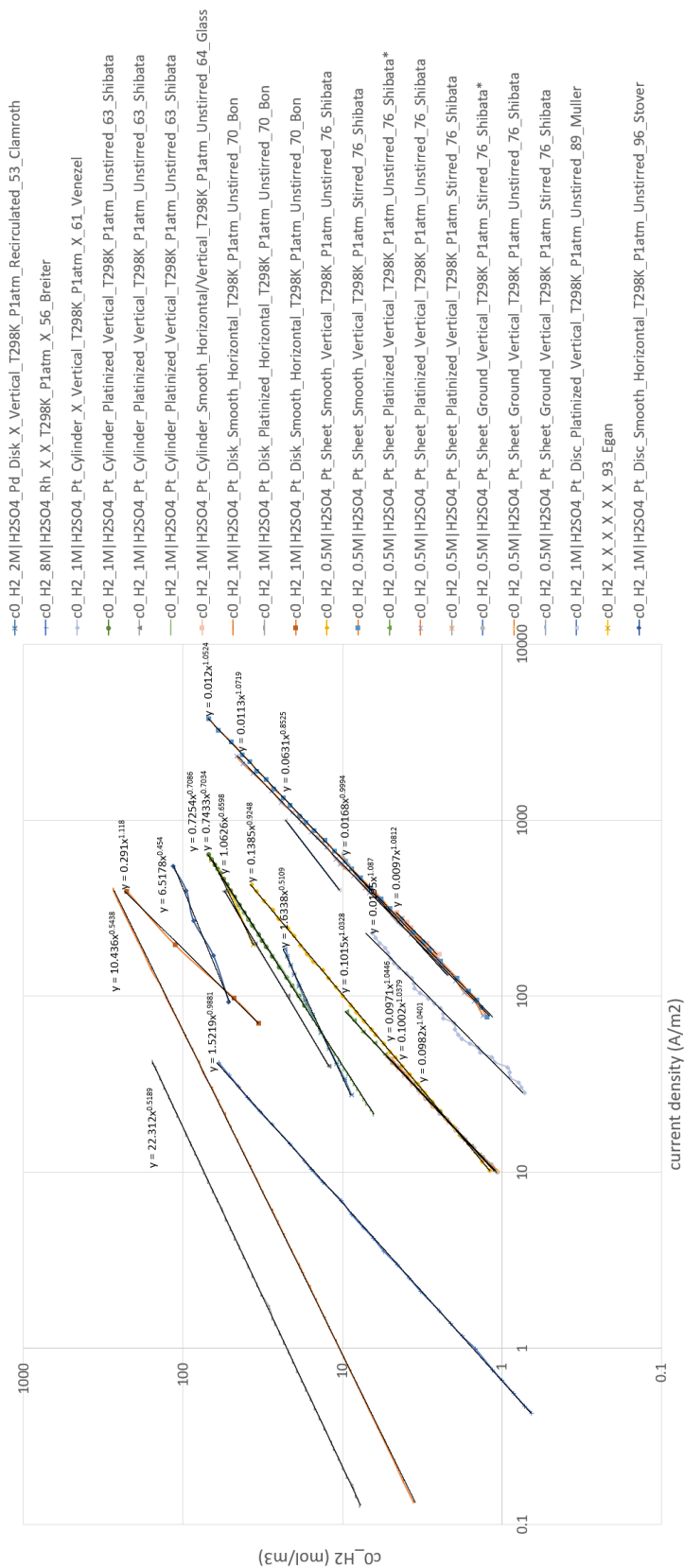
Figure C.1: The dissolved gas concentration for hydrogen in acidic conditions plotted against the current density from various authors. The measurement methods are either based on a current-interrupt method or using film to track the bubble growth over time.

C.1. Conditions Mixture Model & Adherence Region Model

The inlet velocity boundary condition

$$
\begin{aligned}
\mathbf{U}_{c,z} &= 0.01\mathrm{m/s} \cdot \frac{6}{W_1^2} \cdot x \cdot (W_1 - x) && \text{for} \quad 0 \le x \le W_1, \quad \text{and} \quad z = 0 \\
\mathbf{U}_{c,x} &= 0\mathrm{m/s} && \text{for} \quad 0 \le x \le W_1, \quad \text{and} \quad z = 0
\end{aligned}
\tag{C.1}
$$

,where the velocity of the continuous phase in the z-direction is not a uniform velocity profile rather a near parabolic velocity profile. The velocity profile helps to reduce the entrance length such that the beginning of the electrode has a fully developed flow. The near parabolic velocity profile also helps to reduce computational time as the steady state is reached quicker and less finite elements are required.

The outlet boundary condition is pressure boundary condition at the top of the electrode where the continuous and dispersed phase leave the domain. The following pressure boundary condition was used:

$$
\mathbf{p}_{out} = 0 \quad \mathrm{Pa} \quad \text{for} \quad 0 \le x \le W_1, \quad \text{and} \quad z = H_1 + H_2 + H_3
\tag{C.2}
$$

The wall or no-slip boundary conditions describes the velocity between the continuous and dispersed phase with the wall. The velocity for viscous fluids, here the continuous and dispersed phase, is zero.

$$
\begin{aligned}
\mathbf{U}_c(x,z) &= 0 \quad \mathrm{m/s} \quad \text{for} \quad 0 \le z \le H_1 \quad \& \quad H_2 \le zH_3, \quad \text{and} \quad x = 0 \\
\mathbf{U}_d(x,z) &= 0 \quad \mathrm{m/s} \quad \text{for} \quad 0 \le z \le H_1 \quad \& \quad H_2 \le z \le H_3, \quad \text{and} \quad x = 0
\end{aligned}
\tag{C.3}
$$

$$
\begin{aligned}
\mathbf{U}_c(x,z) &= 0 \quad \mathrm{m/s} \quad \text{for} \quad 0 \le z \le H_1 \quad \& \quad H_2 \le z \le H_3, \quad \text{and} \quad x = W_1 \\
\mathbf{U}_d(x,z) &= 0 \quad \mathrm{m/s} \quad \text{for} \quad 0 \le z \le H_1 \quad \& \quad H_2 \le z \le H_3, \quad \text{and} \quad x = W_1
\end{aligned}
\tag{C.4}
$$

Faraday's law is used to couple the gas flux inlet with the applied current density. The oxygen and hydrogen gas flux inlet are stated in the following equations, respectively:

$$
N_{O_2}(x = 0, z) = \frac{1}{4} \frac{RT}{pF} f_{\mathrm{g,H_2}} \cdot i_{\mathrm{loc,\ x\,=\,0}} \quad \text{for} \quad H_1 \le z \le H_2
\tag{C.5}
$$

$$
N_{H_2}(x = W_1, z) = \frac{1}{2} \frac{RT}{pF} f_{\mathrm{g,H_2}} \cdot i_{\mathrm{loc,\ x\,=\,W1}} \quad \text{for} \quad H_1 \le z \le H_2
\tag{C.6}
$$

where i_{loc} is the local current density determined by the electrochemical model at the boundary $x = 0$ and $x = W_1$.

C.2. Conditions Species Model

The dissolved concentration of any species modelled is solved with the governing equation 2.84 and requires initial concentration, boundary conditions, and the sink domain.

The initial concentration conditions are based on the experimental initialization of Janssen *et al.* [28]. The experimental setup is sparged with hydrogen and oxygen gas to ensure a maximum solubility of the species in the electrolyte. For the tracker species an arbitrary value is chosen of 1 M. The initial conditions are equated below:

$$
\begin{aligned}
c_{\mathrm{H_2,initial}} &= c_{\mathrm{in,H_2}} = & c_{\mathrm{s,H_2}} &= 0.794 \quad [\mathrm{mol/m^3}] \\
c_{\mathrm{O_2,initial}} &= c_{\mathrm{in,O_2}} = & c_{\mathrm{s,O_2}} &= 1.26 \quad [\mathrm{mol/m^3}] \\
c_{\mathrm{H_2,track,initial}} &= & c_{\mathrm{in,H_2,track}} &= 1.0 \quad [\mathrm{mol/m^3}] \\
c_{\mathrm{O_2,track,initial}} &= & c_{\mathrm{in,O_2,track}} &= 1.0 \quad [\mathrm{mol/m^3}]
\end{aligned}
\tag{C.7}
$$

The no-flux boundary condition states that there is no mass flux at the boundary. The following boundaries have a no-flux boundary condition:

$$
- \mathbf{n} \cdot \mathbf{U}_i = 0\mathrm{mol/(m^2 s)} \quad \text{for} \quad 0 \le z \le H_1 \quad \& \quad H_2 \le z \le H_3, \quad \text{and} \quad x = 0 \quad \& \quad x = W_1
\tag{C.8}
$$

For the inlet boundary condition there are two different boundary conditions used. The first is a constrained concentration or Dirichlet boundary:

$$
\begin{aligned}
c_{\mathrm{H_2,in}} = c_{\mathrm{s,H_2}} = \ & 0.794 \quad \mathrm{mol/m^3} \quad \text{for} \quad 0 \le x \le W_1, \qquad\qquad \text{and} \quad z = 0 \\
& c_{\mathrm{O_2,in}} = c_{\mathrm{s,O_2}} = 1.26 \quad \mathrm{mol/m^3} \qquad \text{for} \quad 0 \le x \le W_1, \quad \text{and} \quad z = 0 \\
c_{i,track,in} = \ & 1.0 \quad \mathrm{mol/m^3} \quad \text{for} \quad 0 \le x \le W_1, \qquad\qquad \text{and} \quad z = 0
\end{aligned} \tag{C.9}
$$

where i denotes the hydrogen or oxygen tracker species. The second inlet boundary conditions is an inlet condition for the dissolved hydrogen and oxygen concentration. It states that the dissolved flux normal to the electrode wall. Note that the sign is switched depending on which electrode the dissolved oxygen or hydrogen is generated; the flux respective to the electrode must point inward to the bulk and not out of the domain.

$$
\begin{aligned}
-\mathbf{n} \cdot \mathbf{N}_{O_2} = R_{\mathrm{O_2}} = -\frac{1}{4}\frac{i_{loc}}{F} \quad \text{for} \quad H_1 \le z \le H_2 \quad \text{and} \quad x = 0 \\
-\mathbf{n} \cdot \mathbf{N}_{H_2} = R_{\mathrm{H_2}} = \frac{1}{2}\frac{i_{loc}}{F} \quad \text{for} \quad H_1 \le z \le H_2 \quad \text{and} \quad x = W_1
\end{aligned} \tag{C.10}
$$

The outlet boundary condition states that the diffusive flux normal to the outlet is zero. This outlet is a safe approximation of the outlet while the inlet flow velocity is always > 0 m/s. Else the system is not able to lose mass and results in convergency issues.

$$
\mathbf{n} \cdot D_i \nabla c_i = 0 \quad \mathrm{mol/s} \quad \text{for} \quad 0 \le x \le W_1, \quad \text{and} \quad z = H_1 + H_2 + H_3 \tag{C.11}
$$

Finally, the sink domain is determined for both hydrogen and oxygen. The sink term is activated by the mass transfer boundary layer L which is derived in the section 2.2. The sink term within the mass transfer boundary layer represents the dissolved gas uptake by the gas bubbles. The second sink term represents the sink term for dissolved gas towards the bulk:

$$
\begin{aligned}
S_{H_2} = -k_\infty(c_{H_2} - c_{H_2,s}) \quad \text{if} \quad x < (W_1 - L_{\mathrm{H_2}}), \quad \text{for} \quad H_1 \le z \le (H_1 + H_2) \\
S_{H_2} = -k_b(c_{H_2} - c_{H_2,s}) \quad \text{if} \quad x > (W_1 - L_{\mathrm{H_2}}), \quad \text{for} \quad H_1 \le z \le (H_1 + H_2)
\end{aligned} \tag{C.12}
$$

The sink terms for outside and inside the mass transfer boundary layer, respectively:

$$
\begin{aligned}
S_{O_2} = -k_\infty(c_{O_2} - c_{O_2,s}) \quad \text{if} \quad x > L_{\mathrm{O_2}}, \quad \text{for} \quad H_1 \le z \le (H_1 + H_2) \\
S_{O_2} = -k_b(c_{O_2} - c_{O_2,s}) \quad \text{if} \quad x < L_{\mathrm{O_2}}, \quad \text{for} \quad H_1 \le z \le (H_1 + H_2)
\end{aligned} \tag{C.13}
$$

C.3. Conditions Electrochemical Model

The insulation boundary conditions for the electrolyte current and electrode current, respectively:

$$
\begin{aligned}
-\mathbf{n} \cdot i_l = 0 \quad \frac{A}{m^2} \quad \text{for} \quad 0 \le x \le W_1, \quad \text{and} \quad z = 0 \ \& \ z = H_1 + H_2 + H_3 \\
-\mathbf{n} \cdot i_s = 0 \quad \frac{A}{m^2} \quad \text{for} \quad 0 \le z \le H_1, \quad \text{and} \quad x = 0 \ \& \ x = W_1 \\
-\mathbf{n} \cdot i_s = 0 \quad \frac{A}{m^2} \quad \text{for} \quad H_1 + H_2 \le z \le H_1 + H_2 + H_3, \quad \text{and} \quad x = 0 \ \& \ x = W_1
\end{aligned} \tag{C.14}
$$

The initial electrode potential boundary conditions :

$$
\begin{aligned}
\phi_{\mathrm{s,initial}} = 1.23 \quad V \quad \text{for} \quad H_1 \le z \le (H_1 + H_2), \quad \text{and} \quad x = 0 \\
\phi_{\mathrm{s,initial}} = 0.00 \quad V \quad \text{for} \quad H_1 \le z \le (H_1 + H_2), \quad \text{and} \quad x = W_1
\end{aligned} \tag{C.15}
$$

D
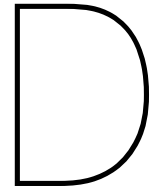
Appendix D

In this appendix the raw data of Janssen *et al.* [28] is presented. Note that Janssen *et al.* uses a different nomenclature for the current density and nucleation site density.

Nature of gas	i (kA m^{-2})	v (m s^{-1})	d [(mm)$^{-2}$]	R_a (μm)	$R_{a,m}$ (μm)	s	V_a (μm)	J [(mm)$^{-1}$]
O$_2$	0.5	0	22	31	65	0.10	8.7	1.85
	1.0		40	28	80	0.18	18.4	4.00
	2.0		83	21	84	0.25	25.5	8.55
	3.0		121	27	110	0.43	51.0	14.16
	4.0		143	21	113	0.41	50.1	17.59
	5.0		175	22	95	0.46	48.3	18.20
	0.5	0.3	11	21	29	0.02	0.7	0.43
	1.0		39	29	57	0.13	7.6	2.26
	2.0		69	27	63	0.23	19.3	5.75
	3.0		92	23	86	0.28	26.1	8.50
	4.0		128	19	78	0.29	26.3	11.78
	5.0		113	23	92	0.34	37.4	12.60
H$_2$	0.25	0	42	32	70	0.22	17.7	3.39
	0.50		77	26	70	0.23	15.2	5.07
	1.00		453	15	85	0.59	37.4	28.80
	1.50		1918	5.9	75	0.56	33.4	110.64
	0.25	0.3	43	13	22	0.03	0.6	1.01
	0.50		37	17	29	0.04	1.2	1.17
	1.00		223	12	36	0.16	4.9	7.20
	1.50		1068	6.9	28	0.24	4.4	19.98
	2.00		2070	5.9	34	0.38	8.4	46.22
	2.50		3572	4.1	32	0.37	8.4	40.96

Figure D.1: The effect of current density (i) on average nucleation site density (d), average radius of adhered bubbles (R), average maximum radus of adhered bubbles ($R_{a,m}$), surface coverage (s), volume of attached bubbles per unit surface (V_a), and basic bubble parameter (J) for an oxygen and hydrogen evolving vertical transparent nickel electrode in 1M KOH, at 303K, 101 kPa and at free and forced convection [28]